FEBRUARY 2023 Ph.D. in Engineering Physics ZEKERİYA UYSAL

REPUBLIC OF TURKEY

GAZİANTEP UNIVERSITY

GRADUATE SCHOOL OF NATURAL & APPLIED SCIENCES

MEASUREMENT OF THE PRODUCTION CROSS SECTION OF B^+ MESON AT CERN-ATLAS EXPERIMENT WITH $\sqrt{s} = 13$ TEV DATA

Ph.D. THESIS

IN

ENGINEERING PHYSICS

BY

ZEKERİYA UYSAL

FEBRUARY 2023

MEASUREMENT OF THE PRODUCTION CROSS SECTION OF B^+ MESON AT CERN-ATLAS EXPERIMENT WITH $\sqrt{S} = 13$ TEV DATA

Ph.D. Thesis
in
Engineering Physics
Gaziantep University

Supervisor
Prof. Dr. Ayda BEDDALL

Co-Supervisor
Prof. Dr. Ahmet BİNGÜL

by

Zekeriya UYSAL

February 2023

© 2023 [Zekeriya UYSAL]

MEASUREMENT OF THE PRODUCTION CROSS SECTION OF B^+ MESON AT CERN-ATLAS EXPERIMENT WITH $\sqrt{S} = 13$ TEV DATA

submitted by **Zekeriya UYSAL** in partial fulfillment of the requirements for the degree of Doctor of Philosophy in **Engineering Physics, Gaziantep University** is approved by,

Prof. Dr. Mehmet İshak YÜCE
Director of the Graduate School of Natural and Applied Sciences .....

Prof. Dr. Ramazan KOÇ
Head of the Department of Engineering Physics .....

Prof. Dr. Ayda BEDDALL
Supervisor, Engineering Physics
Gaziantep University .....

Prof. Dr. Ahmet BİNGÜL
Co-Supervisor, Engineering Physics
Gaziantep University .....

Graduation Date: 09 February 2023

Examining Committee Members:

Prof. Dr. Serkant Ali ÇETİN
Department of Basic Sciences
İstinye University .....

Assoc. Prof. Dr. Andrew John BEDDALL
Department of Basic Sciences
İstinye University .....

Prof. Dr. Mustafa Sadettin ÖZYAZICI
Electrical and Electronics Engineering
Hasan Kalyoncu University .....

Assoc. Prof. Dr. Mustafa YILMAZ
Engineering Physics
Gaziantep University .....

Prof. Dr. Ayda BEDDALL
Engineering Physics
Gaziantep University .....

I hereby declare that all information in this document has been obtained and presented in accordance with academic rules and ethical conduct. I also declare that, as required by these rules and conduct, I have fully cited and referenced all material and results that are not original to this work.

Zekeriya UYSAL

ABSTRACT

MEASUREMENT OF THE PRODUCTION CROSS SECTION OF B^+ MESON AT CERN-ATLAS EXPERIMENT WITH $\sqrt{\mathrm{S}} = 13$ TEV DATA

UYSAL, Zekeriya
Ph.D. in Engineering Physics
Supervisor: Prof. Dr. Ayda BEDDALL
Co-Supervisor: Prof. Dr. Ahmet BİNGÜL
February 2023
113 pages

The differential cross section of B^+ meson is presented as a function of transverse momentum and pseudorapidity. It is determined from the channel $B^+ \to J/\psi K^+$ and reconstructed with using ATLAS pp collision dataset, Run2 2015 data with integrated luminosity of 3.2 fb^{-1}. Measurement is done for 8 intervals of transverse momentum p_{T} and 4 intervals of rapidity $|y|$ covering the range 9 GeV <p_{T} < 120 GeV and $|y| <$ 2.25. B^+/ B^- ratio is consistent with MC and 13 TeV / 7 TeV cross-section ratio is consistent with the theoretical expectations.

Key Words: Cross Section, B^+ Meson, CERN, ATLAS, RPC, GIF++

ÖZET

CERN-ATLAS DENEYİNDE $\sqrt{\mathrm{S}} = 13$ TEV KÜTLE MERKEZİ ENERJİSİ VERİSİYLE B^+ MEZON ÜRETİM TESİR KESİTİNİN ÖLÇÜLMESİ

UYSAL, Zekeriya
Doktora Tezi, Fizik Mühendisliği Bölümü
Danışman: Prof. Dr. Ayda BEDDALL
İkinci Danışman: Prof. Dr. Ahmet BİNGÜL
Şubat 2023
113 sayfa

B^+ mezon diferansiyel tesir kesidi $B^+ \to J/\psi K^+$ bozunma kanalı p_{T} ve $|y|$ aralıkları için hesaplanmıştır. Hesaplamalarda toplam ışınlılığı 3.2 fb^{-1} olan ATLAS Run2 2015 verisi kullanılmış olup, 9 GeV < p_{T} < 120 GeV ve $|y| < 2.25$ aralığında 8 dikine momentum p_{T} ve 4 rapidite $|y|$ bölgesi analiz için seçilmiştir. B^+/ B^- oranı MC ile ve 13 TeV / 7 TeV tesir kesidi oranı teorik hesaplamalar ile uyumlu bulunmuştur.

Anahtar Kelimeler: Tesir Kesiti, B^+ Mezon, CERN, ATLAS, RPC, GIF++

This thesis is dedicated to all those who perished
and suffered the loss of loved ones in the devastating earthquake.
In memory of Derin.

ACKNOWLEDGEMENTS

First and foremost, I am extremely grateful to my amazing family for their support, and constant encouragement.

I would like to express my sincere gratitude to my supervisors, who had a great influence on my getting started with particle physics, Prof. Dr. Ayda Beddall, Assc. Prof. Dr. Andrew J. Beddall, and Prof. Dr. Ahmet Bingül, for their guidance, continued support, patience, motivation, and enthusiasm.

This analysis could not be completed without support of Prof. Dr. Leonid Gladilin, he believed in me and supervised the analysis. I'm deeply indebted to him for what I learned in physics, analysis and statistics. I would like to thank Marina Aleksandrova for her great support in trigger efficiency parts. Also very special thanks to ATLAS BJpsiX group for their support. I'd like to acknowledge the assistance of Prof. Dr. Matteo Cacciari for the FONLL and Prof. Dr. Hubert Spiesberger for the GM-VFNS theory parts.

I would also like to extend my deepest gratitude to Prof. Dr. Serkant Ali Çetin, who trusted and encouraged me to attend RPC upgrade projects and guided with his experiences. I'm very grateful to Luigi Di Stante and Dr. Alessandro Polini for everything I know about RPC.

I also had great pleasure of working with Assc. Prof. Dr. Gökhan Ünel at software interface for RFQ ion source and LEBT line design project called Demirci-Pro. I'd like to express my gratitude to my dear friends Dr. Candan Dozen Altuntaş, Dr. Sinem Şimşek and Prof. Dr. Ilkay Türkçakır for their great friendship and unwavering support.

Finally, thanks to the funding agency, Turkish Energy, Nuclear and Mineral Research Agency (TENMAK) for sponsoring this work.

TABLE OF CONTENTS

Page

ABSTRACT . . . . . **v**

ÖZET . . . . . **vi**

ACKNOWLEDGEMENTS . . . . . **viii**

TABLE OF CONTENTS . . . . . **ix**

LIST OF TABLES . . . . . **xiv**

LIST OF FIGURES . . . . . **xv**

LIST OF SYMBOLS . . . . . **xviii**

CHAPTER 1 . . . . . **1**

INTRODUCTION **1**

CHAPTER 2 . . . . . **2**

LHC AND ATLAS EXPERIMENT **2**

2.1. The Large Hadron Collider 2

2.2. Luminosity Calculation at the LHC 4

2.3. ATLAS Coordinate System and Units 4

2.4. Magnet System 8

2.5. Inner Detector (ID) 8

2.5.1. Insertible B Layer (IBL) 9

2.5.2. The Silicon Pixel Detector 10

2.5.3. The Semiconductor Tracker (SCT) 10

2.5.4. Transition Radiation Tracker (TRT) 11

2.6. Calorimeter System 11

2.6.1. Electromagnetic Calorimeter 12

2.6.2. Hadronic Calorimeter 13

2.7. Muon Spectrometer 14

2.7.1. Resistive Plate Chambers (RPC) 15
2.7.2. Cathode Strip Chambers (CSC) 16
2.7.3. Monitored Drift Tube (MDT) 16
2.7.4. Thin Gap Chambers (TGC) 18
2.8. Trigger and DAQ 19
2.8.1. L1 Trigger 19
2.8.2. High Level Trigger 20
CHAPTER 3 21
DATA AND EVENT SELECTION 21
3.1. Data and MC files 21
3.2. Event Selection and Reconstruction of J/ψ Candidates 22
3.3. Reconstruction of B^+ Candidates 23
CHAPTER 4 24
YIELD CALCULATION 24
CHAPTER 5 27
EVENT REWEIGHTING 27
CHAPTER 6 29
CROSS SECTION CALCULATION 29
CHAPTER 7 31
SYSTEMATIC UNCERTAINTIES 31
7.1. Introduction 31
7.2. nPv Systematic 32
7.3. $|y|$ and PV_z Systematic 33
7.4. p_{T} Systematic 33
7.5. Tracking Systematics 34
7.6. Muon Reconstruction Systematics 34
7.7. Lxy Systematics 35
7.7.1. Overview 35
7.7.2. Lxy Uncertainty due to Detector Resolution 35

7.8. MC Systematics 37
7.9. Fit Systematic 38
7.10. Luminosity Systematic 39
7.11. BR Systematic 39
7.12. Total Systematic 40
CHAPTER 8 43
RESULTS 43
8.1. Cross-section 43
8.1.1. Cross-section in p_{T} Bin 43
8.1.2. Cross-section in y Bin 44
8.1.3. Cross-section in Double Differential Bin 45
8.2. Cross-section Ratio 47
CHAPTER 9 52
CONCLUSION 52
REFERENCES 53
APPENDIX 59
APPENDIX A LUMINOSITY CALCULATION 59
A.1. Good Run Lists 59
A.2. Integrated Luminosity 60
APPENDIX B SELECTION OF THE CUTS 61
B.1. Cut Optimisation 61
B.1.1. Flight Distance L_{xy} 62
B.1.2. Cos(θ'_K) 63
B.1.3. Cos(θ^*_K) 63
B.2. Selection of the Cuts 64
B.3. Primary Vertex Selection 64
B.4. MCP Recommendations for Muon Selection 65
B.4.1. Tight Selection 65
B.5. R_{xy} Selection 66

B.6. The $S(z_0)$ and $S(a_{0xy})$ Selections 67
B.7. Trigger Matching 68
APPENDIX C TRIGGER EFFICIENCY 69
C.1. Di-muon Trigger Efficiency 69
APPENDIX D MC REWEIGHTING 71
D.1. Beam Tilt 72
D.1.1. Tilt in xy-z Plane 72
D.1.2. Tilt in x-z Plane 72
D.1.3. Tilt in y-z Plane 73
D.1.4. Tilt Conclusion 73
D.1.5. Trigger Scale Factors 74
D.2. Refitted Primary Vertex 75
D.2.1. Overview 75
D.2.2. Pv_z Reweighting 77
D.3. Number of Primary Vertices 78
D.3.1. Overview 78
D.3.2. Efficiency Scale Factor 79
D.4. p_{T} Bin Reweighting 80
D.5. $|y|$ Bin Reweighting 82
D.6. Muon Reconstruction Scale Factor 82
APPENDIX E FIT PLOTS 84
E.1. B^+ p_{T} Bins 85
E.2. B^+ y Bins 86
E.3. B^+ Double Differential Bins 87
E.4. B^- p_{T} Bins 88
E.5. B^- y Bins 89
E.6. B^- Double Differential Bins 90
APPENDIX F $B^{\pm}$ MASS TABLES 91
APPENDIX G FONLL TABLES 93

G.1. FONLL $\sqrt{s} = 13$ TeV 94
G.1.1. p_{T} Bin 94
G.1.2. y Bin 94
G.1.3. Double Differential Bin 95
G.2. FONLL $\sqrt{s} = 7$ TeV 95
G.2.1. p_{T} Bin 96
G.2.2. y Bin 96
APPENDIX H GM-VFNS TABLES 97
H.1. GM-VFNS $\sqrt{s} = 13$ TeV 97
H.1.1. p_{T} Bin 97
H.1.2. y Bin 98
H.1.3. Double Differential Bin 98
H.2. GM-VFNS $\sqrt{s} = 7$ TeV 99
H.2.1. p_{T} Bin 99
H.2.2. y Bin 99
APPENDIX I ATLAS SERVICE WORKS 100
I.1. Introduction 100
I.2. Installation, Test, and Commissioning of RPC BME Chambers 100
I.3. BIS78 Resistive Plate Chambers Upgrade 102
I.4. RPC Prototype Tests in GIF++ and H8 106
I.5. Results 108
PUBLICATIONS 111
CURRICULUM VITAE 113

LIST OF TABLES

Page

Table 2.1 List of common LHC parameters. 3
Table 2.2 Selected LHC parameters for pp collisions in 2015. 4
Table 3.1 Data15 and MC16a files used in this analysis. 21
Table 3.2 MC16a Truth0 files used in this analysis. 22
Table 3.3 Selected Run2 triggers for 2015 data. 22
Table 3.4 $B^{\pm}$ reconstruction cuts. 23
Table 7.1 δ_{Lxy} relative ratio in p_{T} bin. 36
Table 7.2 δ_{Lxy} relative ratio in y bin. 36
Table 7.3 δ_{Lxy} in double differential bin. 37
Table 7.4 δ_{MC} in double differential bin. 38
Table 7.5 δ_{Fit} in double differential bin. 39
Table 7.6 Total systematic and statistical uncertainties in DD bins. 40
Table 8.1 Cross-section in p_{T} bin. 44
Table 8.2 Cross-section in $|y|$ bin. 45
Table 8.3 Cross-section in double differential bin. 46
Table 8.4 $\sigma_{13\ \mathrm{TeV}}/\sigma_{7\ \mathrm{TeV}}$ cross-section ratios in p_{T} bin. 49
Table 8.5 $\sigma_{13\ \mathrm{TeV}}/\sigma_{7\ \mathrm{TeV}}$ cross-section ratios in $|y|$ bin. 49
Table A.1 Run2 corresponding luminosity for 2015 data. 60
Table A.2 Calculated luminosity values for selected triggers. 60
Table F.1 $B^{\pm}$ mass and uncertainties of Data15. 92
Table F.2 B^{+} number of candidates, mass and width. 92
Table F.3 B^{-} number of candidates, mass and width. 92
Table G.1 FONLL 13 TeV in p_{T} bins. 94
Table G.2 FONLL 13 TeV in y bins. 94
Table G.3 FONLL 13 TeV in DD bins. 95
Table G.4 FONLL 7 TeV in p_{T} bin. 96
Table G.5 FONLL 7 TeV in y bin. 96
Table H.1 13 TeV GM-VFNS predictions for the p_{T} bin 97
Table H.2 13 TeV GM-VFNS predictions for the y bin 98
Table H.3 13 TeV GM-VFNS predictions for the DD bin. 98
Table H.4 7 TeV GM-VFNS predictions for the p_{T} bin 99
Table H.5 7 TeV GM-VFNS predictions for the y bin 99

LIST OF FIGURES

Page

Figure 2.1 The LHC collider rings. 3
Figure 2.2 ATLAS coordinate system 5
Figure 2.3 ATLAS track parameters 6
Figure 2.4 ATLAS general. 7
Figure 2.5 Inner detector components. 9
Figure 2.6 Cut-away view of calorimeter system 12
Figure 2.7 Ecal slice. 13
Figure 2.8 Muon chamber layout. 14
Figure 2.9 RPC plane structure. 15
Figure 2.10 MDT chamber. 17
Figure 2.11 TGC sectors. 18
Figure 2.12 Trigger and DAQ scheme in ATLAS. 19
Figure 4.1 B^+ and B^- fit result for the first double differential bin. 26
Figure 7.1 NPv distribution for B^+ using PRW tool. 32
Figure 7.2 NPv distribution for B^- using PRW tool. 32
Figure 7.3 Uncertainties in double differential bins. 41
Figure 7.4 Uncertainties in double differential bins. 42
Figure 8.1 $B^\pm$ cross-section in p_T bin. 44
Figure 8.2 $B^\pm$ cross-section in $|y|$ bin. 45
Figure 8.3 $B^\pm$ cross-section in double differential bin. 46
Figure 8.4 B^+ and B^- cross-section ratio in p_T bin. 47
Figure 8.5 B^+ and B^- cross-section ratio in $|y|$ bin. 48
Figure 8.6 $B^\pm$ cross-section ratio of 13/7 TeV in p_T bin. 48
Figure 8.7 $B^\pm$ cross-section ratio of 13/7 TeV in $|y|$ bin. 49
Figure 8.8 $B^\pm$ cross-section ratio of 13/7 TeV in DD bins. 50
Figure 8.9 $B^\pm$ cross-section ratio of 13/7 TeV in DD bins. 51
Figure A.1 Total Atlas integrated luminosity 2015 60
Figure B.1 Track p_T study. 62
Figure B.2 Lxy significance distribution. 62
Figure B.3 Efficiency, purity, EP and significance plots. 63
Figure B.4 Efficiency, purity, EP and significance plots. 64
Figure B.5 R_{xy} distribution of Data and MC. 66

Figure B.6 Significance z_0 distribution. 67
Figure B.7 Significance a_{0xy} distribution. 68
Figure D.1 Data(Left), and MC(Right) V_z vs. $V_{<xy>}$profile. 72
Figure D.2 Data (Left), and MC (Right) V_z vs. $V_{<x>}$ profile. 73
Figure D.3 Data (Left), and MC (Right) V_z vs. $V_{<y>}$ profile. 73
Figure D.4 x-z profile for Data and MC tilt. 74
Figure D.5 y-z profile for Data and MC tilt. 74
Figure D.6 Selection range for triggers. 75
Figure D.7 Data15 and MC16a refitted PV$_x$ position profile plot. 76
Figure D.8 Data15 and MC16a refitted PV$_y$ position profile plot. 76
Figure D.9 Data15 and MC16a refitted PV$_z$ position profile plot. 76
Figure D.10 Data15 and MC16a V_z profile. 77
Figure D.11 Data15 and MC16a nPVs correction. 78
Figure D.12 Data15 and Data16 mean number of interaction per crossing. . . 78
Figure D.13 B^+ and B^- efficiency in DD bin. 79
Figure D.14 B^+ and B^- efficiency in p_{T} bin. 80
Figure D.15 B^+ and B^- Efficiency Ratio in $|y|$ bin 80
Figure D.16 Data15 and MC16a distribution of $N_{candidates}$ in p_{T} bins. 81
Figure D.17 The distribution of B^- candidates after applying $|y|$ correction. 82
Figure E.1 B^+ candidate fit in p_{T} bins. 85
Figure E.2 B^+ candidate fit in y bins. 86
Figure E.3 B^+ candidate fit in double differential bins. 87
Figure E.4 B^- candidate fit in p_{T} bins. 88
Figure E.5 B^- candidate fit in y bins. 89
Figure E.6 B^- candidate fit in double differential bins. 90
Figure F.1 $B^{\pm}$ (mean) mass distribution. 91
Figure I.1 RPC trigger hit occupancy for Data 2015. 101
Figure I.2 Cabling of the BME chambers. 102
Figure I.3 Position of BIS78 chambers. 102
Figure I.4 Assembling of the prototype. 103
Figure I.5 Basic test setup used in BB5. 103
Figure I.6 TDC mezzanine. 104
Figure I.7 OPC setup. 104
Figure I.8 OPC-UA setup in BB5. 105
Figure I.9 Cern accelerator complex. 106
Figure I.10 GIF infrastructure. 107
Figure I.11 GIF++ setup. 107
Figure I.12 TDAQ setup. 108
Figure I.13 H8 test setup. 108

Figure I.14 HV versus Efficiency. 109
Figure I.15 Time resolution vs Effective HV. 109
Figure I.16 Distribution of the ΔT. 110

LIST OF SYMBOLS

m	:	Particle mass, invariant mass
E	:	Particle energy
η	:	Pseudo-rapidity
y	:	Rapidity
$K^{\pm}$	:	Charged K meson
$B^{\pm}$	:	Charged B meson
σ	:	Cross-section
$\mathcal{L}$	:	Luminosity
χ^2	:	Chi-square
p_{T}	:	Transverse momentum
ϵ	:	Efficiency
$\mathcal{A}$	:	Acceptance
w	:	Weight scale factor
δ	:	Systematic scale factor

CHAPTER 1

INTRODUCTION

Studies of heavy-quark production at the Large Hadron Collider (LHC) [1] provides a test of perturbative quantum chromodynamics (QCD) at the highest available collider energies. Heavy-quark production is an important background for measurements in the electroweak and Higgs sectors, and in searches for new physics. Since theoretical predictions suffer from large uncertainties the experimental constraints on heavy-quark production cross sections are of great value.

B mesons, produced in hadronisation involving bottom quarks, are produced at high rates in pp collisions at LHC energies.

The ATLAS experiment [2] at the LHC has previously measured the production of $B^{\pm}$ mesons[1] in pp collisions at $\sqrt{s} = 7\,\text{TeV}$ [3].

In this study, measurements of the B^{+} inclusive production cross sections in pp collisions at $\sqrt{s} = 13\,\text{TeV}$ and their comparison with next-to-leading-order (NLO) QCD calculations are presented. The analysis note for this study [4] is available on the CERN Document Server (CDS), and the most recent results will be published there as well. The summary of the ATLAS qualification task and works described in Appendix I.

[1] Hereafter, referred to as simply B^{+} with charge conjugation implied.

CHAPTER 2

LHC AND ATLAS EXPERIMENT

The Large Hadron Collider (LHC) [5] is a proton-proton collider installed in an underground tunnel near Geneva, Switzerland, with a circumference of 27 km and a depth of 50–175 m. The LHC machine accelerates and collides proton beams, but also heavier ions like lead.

The particles are accelerated in opposite directions in two beams before colliding in four different interaction points that house four of the LHC experiments: ATLAS [6], CMS [7], ALICE [8], and LHCb [9].

The two general-purpose detectors on the LHC are ATLAS (A Toroidal LHC ApparatuS) and CMS (Compact Muon Solenoid), these experiments study a wide range of physics at the TeV scale. A dedicated experiment, LHCb (LHC beauty) is a dedicated experiment for studying the physics of the b-quark to understand, for example, matter and antimatter asymmetries. ALICE (A Large Ion Collider Experiment) is designed to study quark-gluon plasma in lead-ion collisions.

2.1 The Large Hadron Collider

The accelerator complex at CERN, shown in Figure 2.1, consists of linear and circular accelerators which accelerate particles step by step to higher energies. Each accelerator boosts the energy of the beam of particles before they are injected from one machine to the next.

Using an electric field to separate electrons from an atom, protons are extracted from hydrogen gas. The protons are then accelerated in LINAC 2 by RF cavities. The LINAC 2 boosts the energies of the particles up to 50 MeV. The protons are then sent to the Proton Synchrotron Booster (PSB) [1, 5], the first circular accelerator in the chain, to increase the energy to 1.4 GeV, followed by the Proton Synchrotron (PS) [1, 5] where

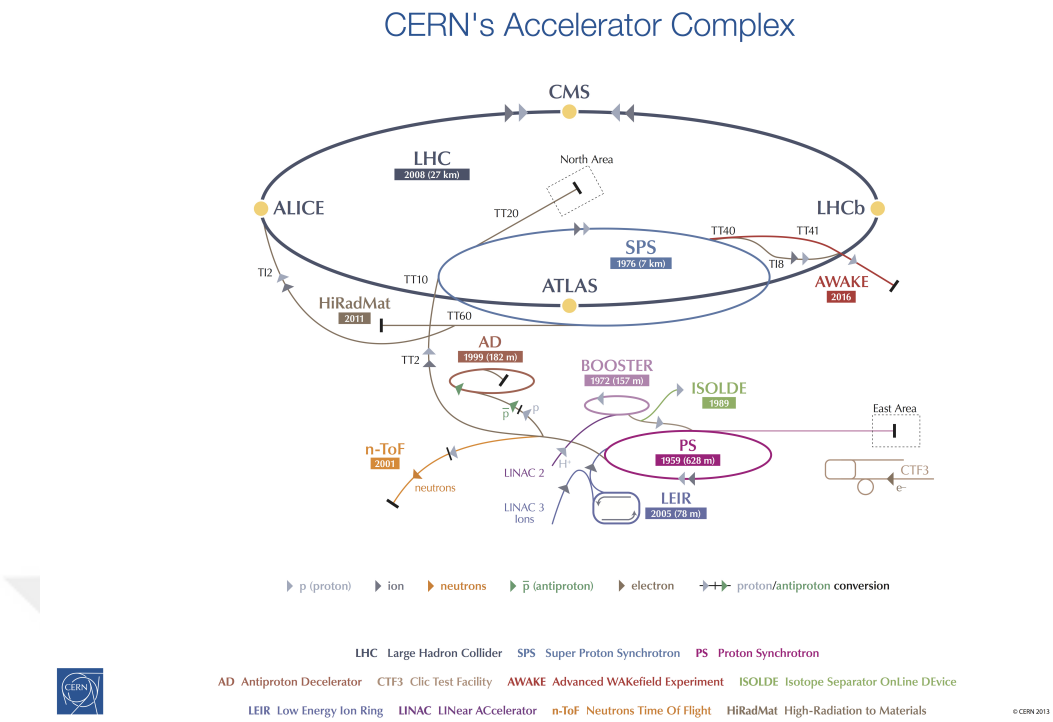

Figure 2.1 The LHC collider rings [10].

the energy of the particles reaches 25 GeV, this beam is then delivered to the Super Proton Synchrotron (SPS) [1, 5] where it is accelerated to 450 GeV. The final step is the injection into the LHC in both clockwise and anti-clockwise directions, where the beams reach the nominal energies of 7 TeV (in Run1) and 13 TeV (in Run2). In the LHC beams are composed of bunches of protons which are guided by 8.3 Tesla superconducting magnets operating at a temperature of 1.9 K and cooled by liquid helium. Dipole magnets steer the protons around the ring while quadrupole magnets provide focussing. After reaching the nominal energy, the beams are collided every 25 ns at the locations of the CMS, ATLAS, LHCb and ALICE experiments. Table 2.1 [11, 5] summarizes some LHC beam parameters.

Table 2.1 List of common LHC parameters.

Machine Configuration	Nominal Value
No. of bunches per proton beam	2808
No. of protons per bunch	1.15×10^{11}
Bunch spacing (ns)	25
Peak luminosity	$10^{34} cm^{-2} s^{-1}$

2.2 Luminosity Calculation at the LHC

The luminosity, $\mathcal{L}$, of the colliding beams can be expressed as a proportionality factor between the number of events per second and the cross-section σ, which can be defined as the effective area assigned to two colliding particles.

$$\mathcal{L} = \frac{R_{inel}}{\sigma_{inel}} = \frac{\mu\, n_b\, f_r}{\sigma_{inel}} \tag{2.1}$$

where, $\mathcal{L}$ is instantaneous luminosity, which is in units of cm^{-2}s^{-1}. R_{inel} is the rate of inelastic pp collisions. σ_{inel} is the inelastic pp collision cross-section, it is expressed in barns, where 1 barn = 10^{24} cm^{-2}s^{-1}. μ is the average number of inelastic pp interactions per bunch crossing, n_b is the number of bunch pairs colliding per revolution, f_r is the revolution frequency. In order to define the number of observed events in an experiment, the integrated luminosity is used. The integral of the instantaneous luminosity over time is called integrated luminosity and can be formulated as follows:

$$\mathcal{L}_{int} = \int_0^T \mathcal{L}(t)dt \tag{2.2}$$

By using Equation 2.2 the total number of events N generated in a particular reaction can be defined as:

$$N = \sigma \int \mathcal{L}(t)dt = \sigma \mathcal{L}_{int} \tag{2.3}$$

One of the primary goal of a collider experiment is to optimize the integrated luminosity

Table 2.2 Selected LHC parameters for pp collisions at $\sqrt{s}$ = 13 TeV in 2015 [12].

Parameter	Value
Maximum number of colliding bunch pairs (n_b)	2232
Bunch spacing	25 ns
Typical bunch population	1.1×10^{11}
Peak luminosity	$5 \times 10^{33} cm^{-2} s^{-1}$
Peak number of inelastic interactions/crossing ($< \mu >$)	~ 16
Luminosity-weighted mean inelastic interactions/crossing	13
Total delivered integrated luminosity	4.0 fb^{-1}

in order to collect as much data as possible and make it available for physics analyses. Thus, luminosity data is essential for cross-section measurements.

2.3 ATLAS Coordinate System and Units

The position of the ATLAS detector components, depicted in Figure 2.4, and their reconstructed objects, are defined using a conventional coordinate system. The x-y

plane is the transverse plane that is perpendicular to the beam direction, and the z-axis is defined by the beam direction. The positive x-direction points toward the centre of the LHC ring, while the positive y-axis is defined as pointing upwards from the interaction point. The positive z-axis direction is then determined using the standard right-handed coordinate system shown in Figure 1, where the detector along the $z > 0$ is labeled as side A, the detector along the $z < 0$ is labeled as side C, and the central barrel is labeled as B.

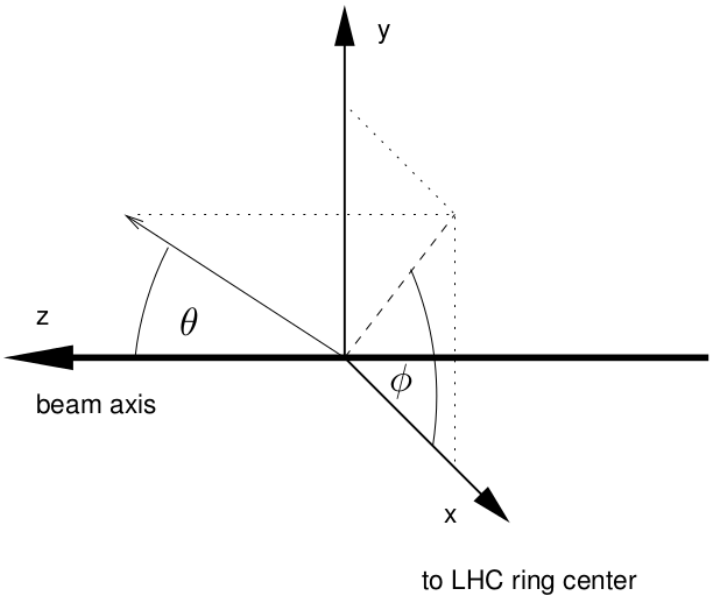

Figure 2.2 The ATLAS coordinate system. The direction of a particle is specified by the two angles θ and ϕ.

The azimuthal angle, ϕ is measured around the beam axis, with positive (negative) values that are correlated with the top (bottom) part of the detector. The polar angle θ describes the angle with respect to the beam axis [13] and is more usually described in the form of pseudo-rapidity defined as

$$\eta = -\ln\tan(\theta/2) \tag{2.4}$$

This variable is preferred instead of theta because it is invariant for Lorentz boost along the beam line, but only in the relativistic regime. Otherwise, rapidity is used over the polar angle and formulated as follows,

$$y = \frac{1}{2}\ln(\frac{E+p_z}{E-p_z}) \tag{2.5}$$

The polar angle and pseudorapidity allow defining the transverse momentum of particles $p_{\mathrm{T}} = \sqrt{p_x^2 + p_y^2}$ or the transverse energy $E_T = \sqrt{E_x^2 + E_y^2}$. These variables also allow

describing the angular separation between two objects called DeltaR which is formulated as in Equation 2.6.

$$\Delta R = \sqrt{(\Delta\eta)^2 + (\Delta\phi)^2} \tag{2.6}$$

Two impact parameters are defined for a particle trajectory. The transverse impact parameter d_0 is defined as the distance in the transverse plane between the point of closest approach and the nominal beam axis. The distance in z direction from the point of closest approach to the nominal interaction point is specified as the longitudinal impact parameter z_0. Figure 2.3 shows the representation of the impact parameters.

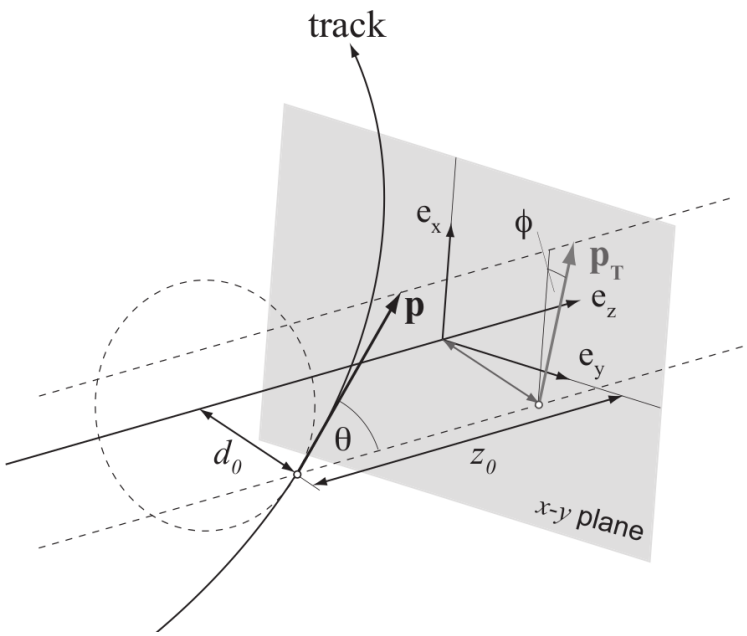

Figure 2.3 Representation of ATLAS track parameters [14].

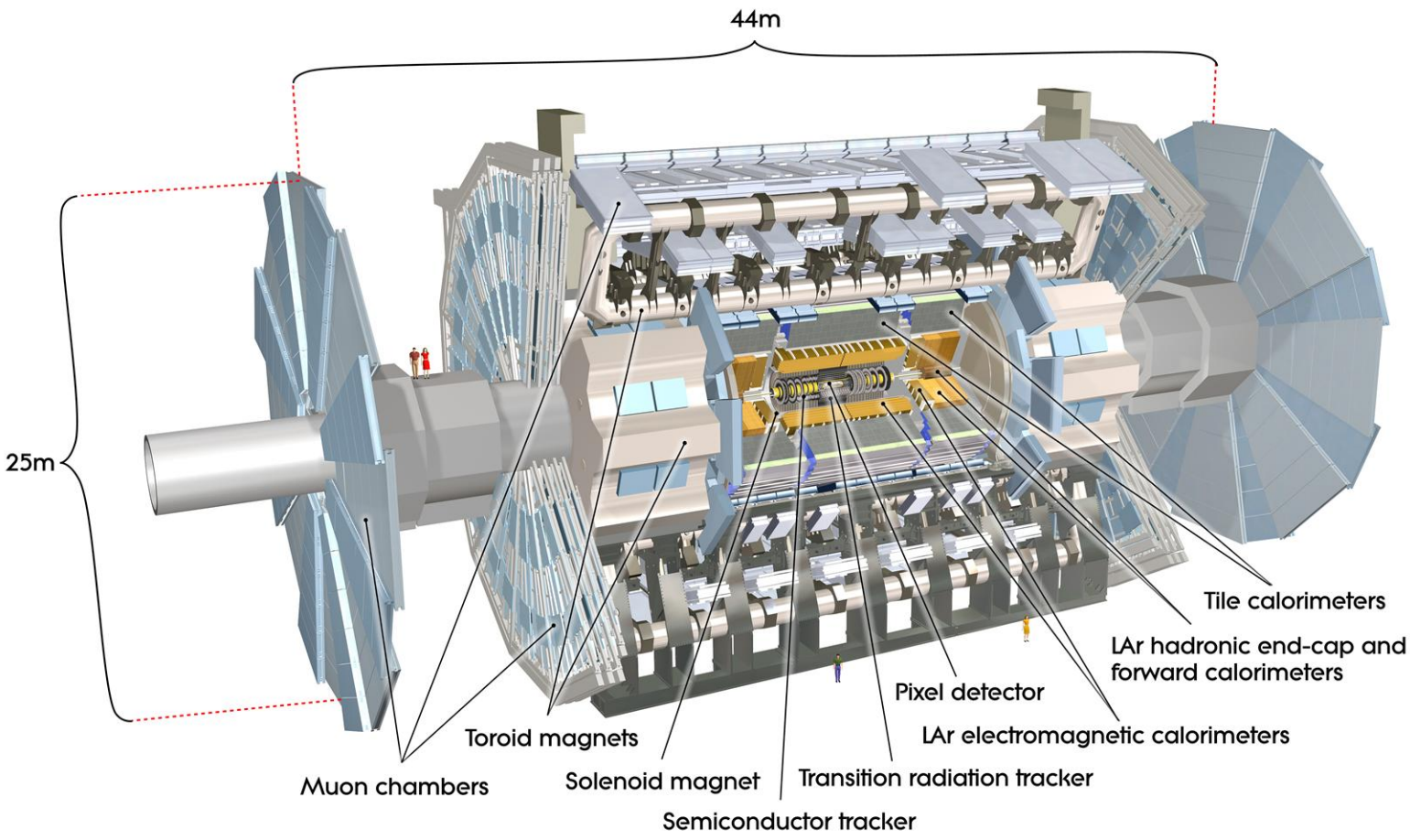

Figure 2.4 General view of ATLAS detector and its parts [15].

2.4 Magnet System

The ATLAS magnet system bends charged particles around the multiple layers of detector systems and also provides a means to contain the tracks of particles. In order to separate and measure the momentum of the produced charged particles up to TeV range, a specific magnetic field distribution is required. Which allows us to determine the charge and transverse momentum of particles (q/p_{T}). The magnet system of ATLAS consists of the toroidal field (TF) magnet with the barrel toroid (BT), the two end cap toroids (ECT), and the central solenoid (CS). BT and ECT bends particles in the R-z plane while the CS bent in the R-ϕ plane [16]. The superconducting magnets are cooled by liquid helium at 4.8 K. The main components of the magnet system are described in the following subsections.

The central solenoid magnet is designed to provide a magnetic field of 2 T [17] at the centre of the ATLAS tracking volume and is enclosed by end-cap toroids and a barrel toroid. This high magnetic field allows very energetic particles to curve enough to measure their momentum very precisely. The solenoid is a single-layer coil wrapped internally in a supporting cylinder with an inner diameter of 2.46 m and an outer diameter of 2.56 m, with an axial length of 5.8 m [6]. The flux of the magnetic field is delivered by the steel of the hadronic calorimeter.

Toroid magnets provide magnetic fields for the muon spectrometer, approximately 0.5 Tesla and 1 Tesla for the muon detectors in the central and end-cap regions respectively. The barrel toroid comprises eight superconducting coils circularly located around the beam axis, while two extra toroids, one in each end-cap, have been employed in the end-cap regions. Barrel toroid has 25.3 m lentgh, 9.4 m inner diameter and 20.1 m outer diameter.

2.5 Inner Detector (ID)

The Inner Detector is the innermost component of the ATLAS detector. It is located inside a 7 m long container with a radius of 1.15 m, and the whole system is placed inside the 2 T magnetic field produced by the central solenoid [6].

The ID is divided into three sub-detectors, which are in order of radial distance from the collision point. The Pixel Detector is situated in the innermost, and the Semi Conductor Tracker (SCT) is placed in the middle part, while the Transition Radiation Tracker (TRT) is located in the outermost part. Both pixel and SCT use silicon, and TRT uses the straw tube as a detecting technology. The insertible B layer is the part of the pixel

detector located between pixel layer 0 (B layer) and beampipe which is detailed in the following section.

Although these three subsystems are technically independent, they perform complementary to fulfill the basic experimental tasks conducted by the ID. For charged tracks above a given p_T threshold and within the pseudo-rapidity range $|\eta| < 2.5$, the ID is designed to provide hermetic and robust pattern identification, excellent momentum resolution, and both primary and secondary vertex measurements. It also plays an essential role in electron identification over $|\eta| < 2$ and a wide range of energies.

The schematic description of the ID and relative positions of its sub-systems is shown Fig 2.5.

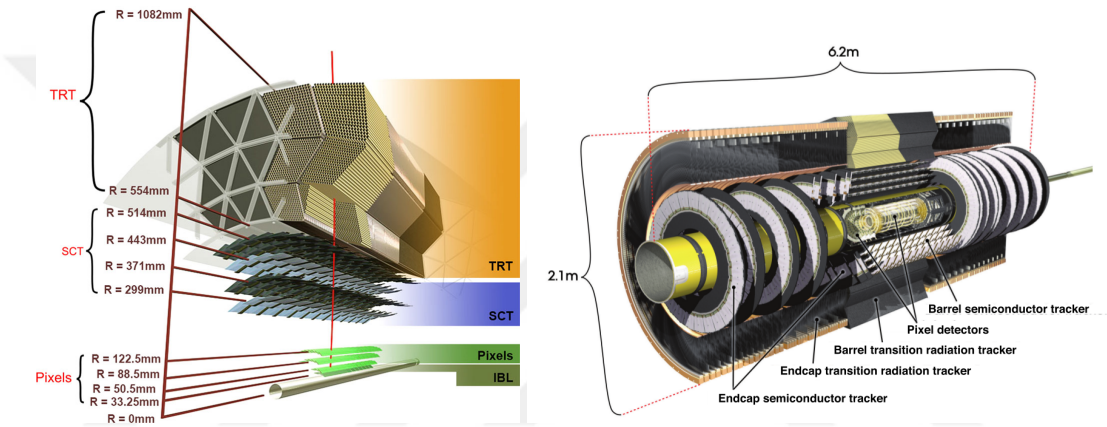

Figure 2.5 Main components of the inner detector [18] [6].

The inner detector provides a combined track momentum resolution [6] described in the below Equation.

$$\frac{\sigma_{p_{\mathrm{T}}}}{p_{\mathrm{T}}} = 0.05\%\ p_{\mathrm{T}} \oplus 1\%. \tag{2.7}$$

The details of the ID components are described in the following sections.

2.5.1 Insertible B Layer (IBL)

The Insertible B layer is the innermost component of the inner detector and has a radius of 3.3 cm. It is located very close to the beam pipe [19]. This new layer, a fourth-pixel detector layer, is installed for Run 2 to improve the precision and robustness of the track reconstruction [18]. For the low p_{T} tracks the impact parameter resolution are improved by a factor of two [20], which improves our B Physics analysis resolution.

The IBL consist of 14 azimuthal carbon stave housing 280 silicon pixel modules, staves are placed at 33.25 mm radial distance covering the beampipe. Staves covering the

region of $|\eta| < 2.7$ having two-chip planar modules, while the staves covering the region $2.7 < |\eta| < 3$ having 8 single chip with 3D sensors [18].

2.5.2 The Silicon Pixel Detector

The silicon pixel detector is designed to provide a very high-granularity, high-precision set of measurements as close to the interaction point as possible. It consists of three barrel layers at radii of 50.5 mm (also called B layer), 88.5 mm (layer1) and 120.5 mm (layer2). To cover a pseudo-rapidity range of $|\eta| < 2.5$, three end-cap disks with inner radius of 89 mm placed at z position of $\pm$ 495 mm, $\pm$ 580 mm, $\pm$ 650 mm at each side of the detector. To suppress the electronic noise, the cooling system keeps the detector at a temperature of 0 °C.

The pixel detector provides high precision space-point measurements of 10 μm in the R-ϕ direction and 115 μm in the R-z direction [21] by defining the first three hits. Besides, its capability helps to reconstruct the tracks of short-lived particles as well as their corresponding vertices. The hits in the detector are registered and readout if the signal in a given pixel exceeds an adjustable threshold [22].

2.5.3 The Semiconductor Tracker (SCT)

The SCT comprises of 4088 two-sided modules spanning 6.3 million channels[23]. Each module contains two layers of silicon micro-strip wafers fixed back-to-back and a hybrid system with the read-out electronics.

The modules are arranged in four barrels between 299 and 500 mm long with a length of 1492 mm, covering the pseudo-rapidity range $|\eta| < 1.1 - 1.4$, and nine forward wheels on each side with radii of 56 cm at positions from 853.8 mm to 2720.2 mm, extending the coverage to $1.1 - 1.4 < |\eta| < 2.5$. Thus, it provides at least four precision hit measurements for each track and contributes to the momentum, impact parameter, and vertex position. Two detector pairs are glued together back-to-back with a 40 mrad stereo angle, separated by a heat transport plate, and the electronics are mounted above the detectors [13]. The position resolution of SCT is 17 μm in Rϕ (azimuthal) and 580 μm z-direction (along the beam) [21]. The detector operates at -7 °C to suppress the electronic noise and at a bias voltage of 150 V. The detector registers a hit if the pulse height exceeds a preset threshold corresponding to a charge of 1 fC [22].

2.5.4 Transition Radiation Tracker (TRT)

The outer tracker of ATLAS is a combined straw tracker and transition radiation detector covering the radial section from 560 mm to 1080 mm. While the barrel region covers the pseudo-rapidity range $|\eta| < 1.1$ with a 144 cm long straws with a readout at their ends, the end-caps have 37 cm straws placed radially in wheels and extend the coverage to $|\eta| < 2.0$. The TRT provides on average 35 two-dimensional measurement points with a resolution of about 130 μm for charged particle tracks with $|\eta| < 2.0$ and $p_T > 500$ MeV. The TRT is composed of 298304 carbon-fibre reinforced Kapton straws (drift tubes) filled with an argon- or xenon-based gas mixture, 4 mm in diameter and held at a potential of 1530 V, with a 31 μm diameter gold-plated tungsten wire at the centre referenced to ground [24]. The high negative voltage on the straw wall creates an electric field, causing the primary electrons to be accelerated towards the central anode and liberate more electrons, resulting in a detectable current signal. The signal generated inside the straws is then amplified, shaped, and finally discriminated providing a timed leading edge that is translated to a drift circle. The space between the straws is filled with layers of materials with varying dielectric characteristics. Transition radiation is emitted when a relativistic particle passes through a boundary between two media with different permittivity values. The radiated photons ionize the gas providing much larger signals that are discriminated with a high threshold. Since electrons exhibit more transition radiation, the TRT provides particle identification capability [25]. During Run1, it is filled with a gas mixture of 70% Xe, 27% CO_2 and 3% O_2 [6]. However in Run2, straws with large gas leaks are filled with 70% Ar, 27% CO_2 and 3% O_2, Argon is cheaper than xenon but has lower efficiency to absorb the TR photons.

2.6 Calorimeter System

The ATLAS Calorimetric System (CS) is located between the ID and the Muon System (MS) and is divided into electromagnetic, hadronic and forward calorimeter parts.

The CS is designed to provide precise measurements of the electron, protons, and jet energies. It also helps to determine the missing transverse energy, which requires both excellent energy measurement resolution and hermeticity.

Additionally, the CS determines the spatial isolation of particles, which is very crucial to the suppression of the background, and classifies particles (mostly electrons and photons) based on their shower form and longitudinal energy leakage. Furthermore, it can provide muon identification separately from the MS, which is important for the performance study of the MS.

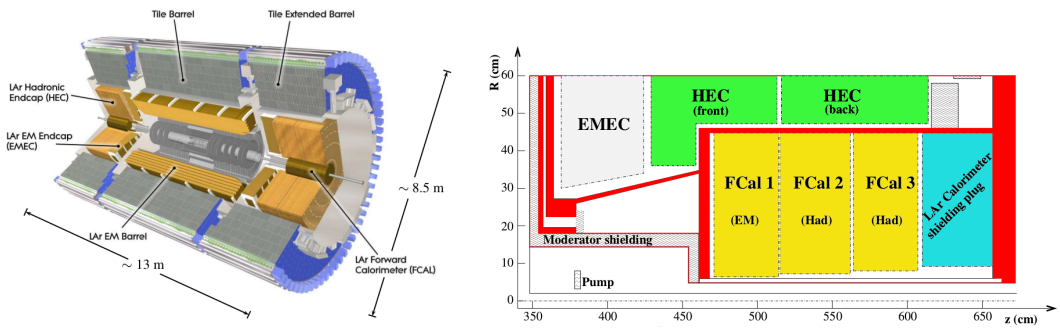

Figure 2.6 Cut-away view of calorimeter system [6].

Particles entering the calorimeter initiate the particle showers. For energetic electrons or photons, a particle shower is produced by electromagnetic interaction (mainly pair production for photons and bremsstrahlung for electrons). Electromagnetic (EM) objects such as electrons and photons are stopped inside Electromagnetic Calorimeter (EMC), and their entire energy is absorbed and measured. Hadrons are stopped at the Hadronic Calorimeters, which are located in an upper layer of EMC, provided by a steel/scintillator-tile calorimeter. The differnt parts of the calorimeter systems are defined briefly in the following sections.

2.6.1 Electromagnetic Calorimeter

An electromagnetic calorimeter is a type of sampling calorimeter that employs a steel-coated lead as an absorber and Liquid Argon (LAr) as an active material. The thickness of the lead absorber is η dependent. The calorimeter's overall thickness is about 22 radiation lengths(X_0) and more than 24 at Barrel regions [6]. Barrel part (EM LAr Barrel) has a coverage of $|\eta| < 1.475$, and two end caps called Electromagnetic End Cap Calorimeter (EMEC) with a coverage of $1.375 < |\eta| < 3.2$.

It is characterized by the accordion-shaped structure of its detection elements due to the uniformity of the detector in ϕ symmetry. Besides, a pre-sampler layer with a coverage of $|\eta| < 1.8$ is supplemented to provide additional measurement to correct the energy losses in the cryostat, service regions, and ID. The EM LaR consists of three sections: front, middle, and back. Each compartment is segmented into different sizes of cells. Each section of the EM is presented in Figure 2.7.

The energy resolution of the calorimeter is given by the following equation :

$$\frac{\delta E}{E} = \frac{a}{\sqrt{E}} \oplus \frac{b}{E} \oplus c \tag{2.8}$$

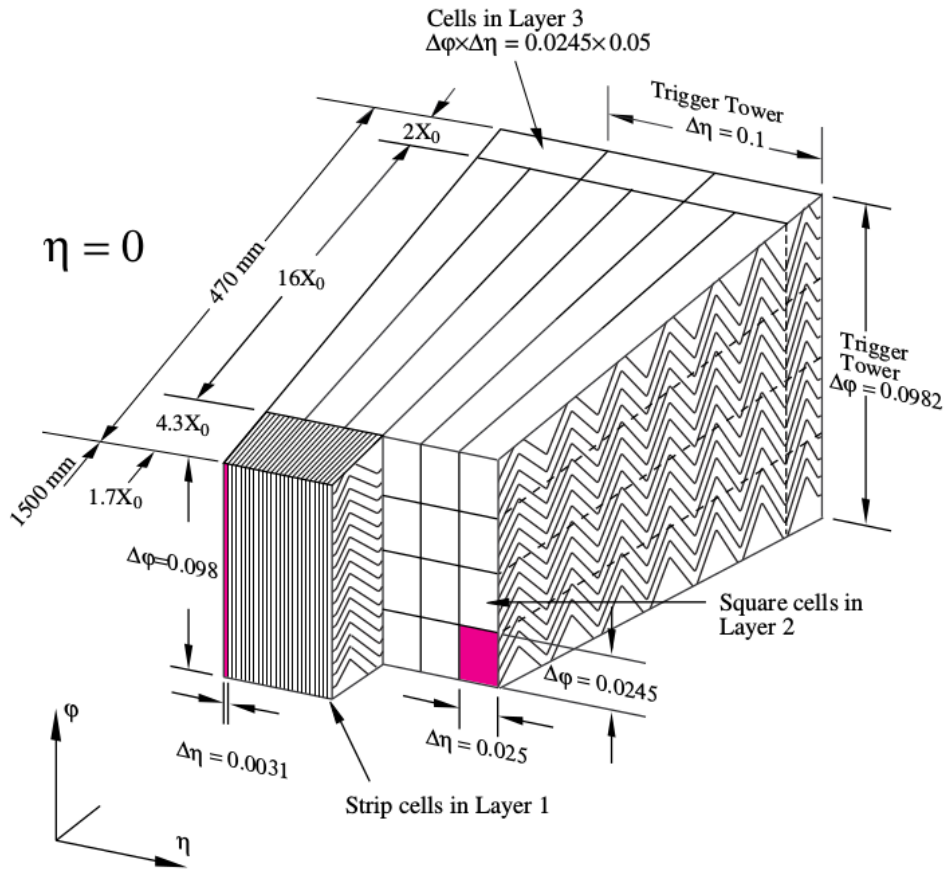

Figure 2.7 Ecal slice [6].

Where E is in GeV and $\oplus$ denotes the addition in quadrature. The sampling term a based on the construction of the calorimeter, and the constant term c depends on the precise knowledge of the non-uniformities in the geometry of the calorimeter or in the pulse shapes, and term b is called noise term of the energy resolution. The typical values are : $a = \sqrt{0.1}$ GeV, $b = 0.17$ GeV and $c = 7 \times 10^{-3}$ [26].

2.6.2 Hadronic Calorimeter

The ATLAS hadronic calorimeter is divided into one barrel and two end-cap sections. The barrel part is the Tile Hadronic Calorimeter (TileCal) and occupies the pseudo-rapidity range ($|\eta| < 1.7$). It uses the tiles of plastic scintillator as an active material which is planted in iron absorbers [6]. The hadronic end-cap calorimeter (HEC) exceeds the ($1.5 < |\eta| < 3.2$) range using the LAr technology and copper as the absorbing material. The forward calorimeter is located in the forward region and covers the $3.1 < |\eta| < 4.9$ pseudo-rapidity range. It also uses LAr technology. Forward Calorimeter (FCAL) has three modules in each end cap. The first module is important for the measurement of the electromagnetic energy and uses copper absorbers. Last two

modules, measure the energy of the hadrons and use tungsten as an absorber. Although it cannot be employed for precision measurements associated with reconstructed tracks of charged particles due to having coverage out of the acceptance range of both the ID and MS, it provides a reliable measurement of the missing energy in each event as well as the jet energy measurements in the very forward region.

2.7 Muon Spectrometer

The Atlas Muon Spectrometer is built for the precision detection of muons and muon momentum measurements. The Atlas muon system consists of four sub-systems which are: Cathode Strip Chambers (CSC), Monitored Drift Tube(MDT), Resistive Plate Chambers(RPC), and Thin Gap Chambers (TGC). The muon chamber layout is shown in Figure 2.8. The Muon System is split into two types: precision and trigger detector systems. It provides independent momentum measurements and triggers information from the charged particle trajectories within the magnetic field supplied by toroid magnets.

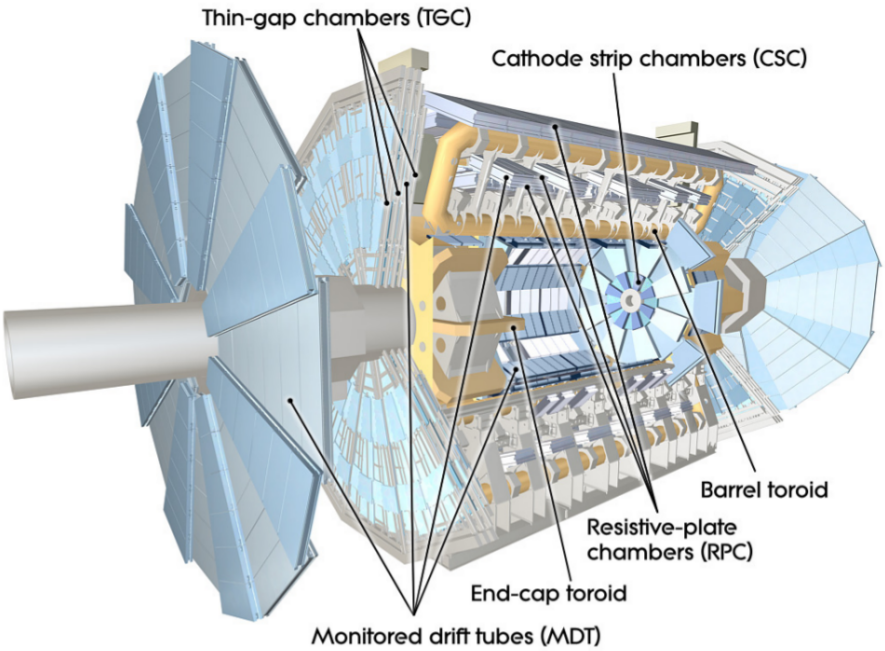

Figure 2.8 Muon chamber layout [6].

Muon precision system consisted of CSCs that covers $2.0 < |\eta| < 2.7$ and MDTs covering $|\eta| < 2.7$. The Muon trigger system is made up of two sub-detectors which are RPCs covering $|\eta| < 1.05$ of the barrel region and TGCs covering $1.05 < |\eta| < 2.7$ of the end cap region. Each sub-detector is expressed in detail in the following sections.

2.7.1 Resistive Plate Chambers (RPC)

The RPC detectors are composed of two parallel conductive plates separated by a small gap at around 2 mm. The plates are typically made of metal, such as aluminum or copper, and the gap is filled with a gas mixture at atmospheric pressure, such as isobutane or argon. When a charged particle passes through the gap, it ionizes the gas, creating a current pulse that can be detected by the electrodes on the plates. The gas composition is $C_2H_2F_4$ (94.7%) , iso-C_4H_{10} (5%), SF_6 (0.3%) with a nominal working voltage (V_0) of 9.6 kV, and a standby voltage (V_1) of 9.0 kV [27].

RPCs are used not only for triggering, but also for muon reconstruction to measure the track positions in non-bending (ϕ) coordinate [28]. Moreover, it provides a time measurement used to reject cosmic muons and to search for delayed signals from high-mass long-lived particles [29]. It covers the psedo-rapidity range of $|\eta| < 1.05$ and has nearly 380k electronic channels.

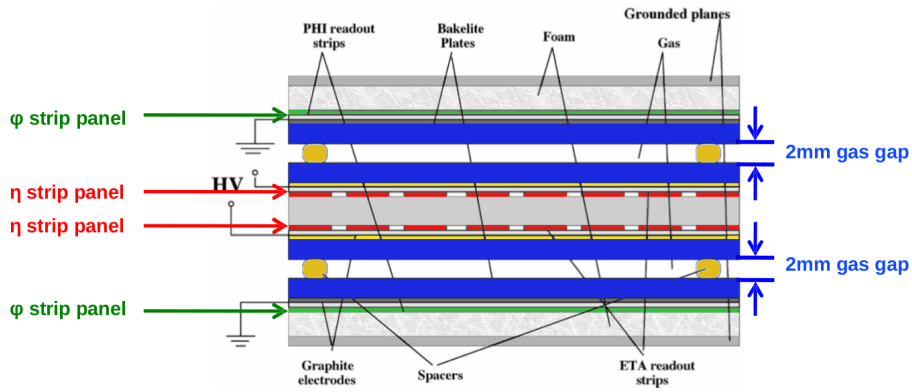

Figure 2.9 RPC plane structure [27].

The ATLAS RPC system consists of three layers of doublet chambers, each composed of two RPC gas gaps with readout electrodes and electronics. Two RPC doublets are attached to the two sides of the middle layer of MDT chambers (BM), and the third one to the one side of the outer MDT layer (BO).

As shown in Figure 2.9, each chamber contains a double-layer of RPCs, Layer0 is closer to interaction point, and Layer1 is away from it. A layer is made of a gas volume with 2 mm gaps filled with gas and operated in avalanche mode. Each gas volume is equipped with two panels of readout strips 25-35 mm wide in orthogonal coordinates (η, φ).

The electrodes are made of Bakelite. An RPC doublet chamber is made up of two sensitive gas gaps which are read out on both surfaces with orthogonal strips to produce eta (bending plane) and phi (azimuthal) coordinate measurements [27].

A resistive coat, covering the electrode surfaces, establishes an electric field of several kV/mm across the gap, capable of initiating the electron avalanche immediately after the primary ionization.

Although the resistivity is low enough to ensure the uniformity of the electric field, it is still transparent to the fast signal transients. This field configuration is a unique feature of RPCs, resulting in excellent spatial and timing resolution [27].

While the intrinsic detector time resolution is about 1.1 ns [30], the overall system resolution, covering the complete readout chain, is 1.9 ns [31, 27]. Inside the detector faraday cage, the front-end boards provide discriminating signals to the trigger and readout pad boxes, which digitize the data and apply the lower-level trigger logic [32]. There are 1094 RPC doublet chambers with a total detection surface of 6785 m^2, which has approximately about 370000 readout channels, and 848 pad boxes [31, 27]. These are the main components of our RPC trigger system. It is performed consistently during Run2 [33].In our case, it provides both single-muon triggers and di-muon triggers with p_{T} thresholds starting from 4 GeV [34].

2.7.2 Cathode Strip Chambers (CSC)

Cathode Strip Chambers are the precision tracking chambers in the innermost end cap region where the particle rates are beyond the MDT limits. It has around 31 K electronic channels and covers the$2.0 < |\eta| < 2.7$ pseudo-rapidity range. The nominal voltage is 1.3 kV and standby voltage is 1.9 kV. The chambers are filled with a gas mixture of Ar (80 $\%$) and CO_2 (20 $\%$) and ionization of the gas caused by the passage of a charged particle is transformed into an electron avalanche near the wires.

Its operation principles are the same as with multi-wire proportional chambers. There are 4 precision η and 4 transverse φ layers in each chamber. Each η layer has 192 channels, and each φ layer has 48 channels with different strip sizes. The anode wires are distributed radially in each chamber where the cathode strips are mounted, as well as the $\eta - \phi$ plane, so that the muon track position can be measured by interpolating the induced charges in different strip layers.

2.7.3 Monitored Drift Tube (MDT)

Monitored Drift Tubes are precision chambers that do the measurement in η coordinates. It covers the pseudo-rapidty range $|\eta| < 1.05$ in the barrel region and $1.05 < |\eta| < 2.7$, has about 360K electronic channel. The gas composition is Ar (93 $\%$) : CO_2 (7 $\%$):

H_2O (1000 ppm)

Each MDT chamber has two sets of either three or four layers of drift tubes separated by a spacer (except for BEE and BIS8 chambers, which have only one multilayer). The chambers at the inner station have more detection layers for better granularity. After installing the chambers in their positions in the spectrometer, the displacements and mechanical deformations are monitored with an optical alignment system. The schematic of the MDT chamber can be seen in the Figure 2.10.

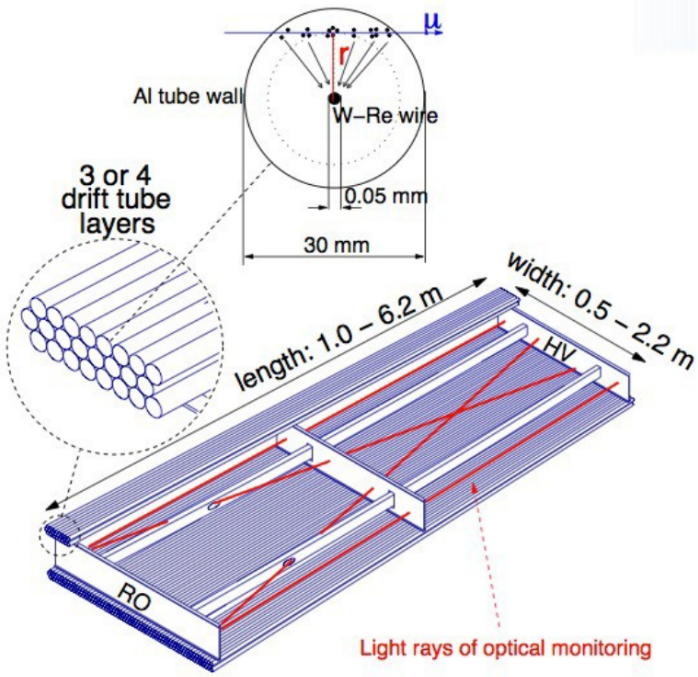

Figure 2.10 MDT chamber structure [6].

As with most gaseous detectors, the detecting principle of an MDT is based on ionization. When a charged particle passes through the tube, it ionizes the gas and releases electrons from the gas atoms. The electrons start drifting towards the wire and are accelerated by the electric field, while the positive ions drift in the opposite direction towards the tube wall. The accelerated primary electrons gain more energy and cause the ionization of more atoms, creating an avalanche close to the wire where the potential is highest. The secondarily generated ions drift through to the tube wall by traveling the whole distance from the wire to the wall. Then the induced signal on the wire circulated to the end of the tube. An amplifier (followed by a discriminator) is used to feed the pulse and the pulse is sent to the time-to-digital converter (TDC) which is installed on the chamber.

In ATLAS, MDT and RPC's are specially positioned. RPCs and MDTs are often used together in particle physics experiments because they complement each other in their

ability to measure the trajectory of charged particles. RPCs have a large active area and are good at detecting particles with high transverse momentum, but they have limited spatial resolution and are not very efficient at detecting low-momentum particles. MDTs have a smaller active area but higher spatial resolution and are more efficient at detecting low-momentum particles, but they are not as good at detecting particles with high transverse momentum. By combining the strengths of both types of detectors, it is possible to accurately measure the trajectory of a wide range of charged particles.

2.7.4 Thin Gap Chambers (TGC)

TGCs are multi-wire proportional chambers with thin gas gaps having anode-cathode gap 1.4 mm The high electric field around the TGC wires with respect to their small wire distance provides a good time resolution of the tracks, except for the tracks passing midway between two wires, where the drift field vanishes [6].

The chambers are divided into three groups known as M1, M2, and M3. The first station, M1, is a triplet that is located around 13 meters away from the interaction point (IP). The second station is a doublet that is about 14 meters away from the IP, and the third station is also a doublet that is around 15 meters away from the station [27].

The TGC chambers wire group are positioned in such a way that the radial strips measure the azimuthal coordinate with resolution around 3 mrad [6]. And other wire group alignments provides good time and space resolution. The muon p_{T} is calculated by the angle of the segments with respect to a straight line pointing to nominal interaction point.

The TGC schematic is shown in Figure 2.11.

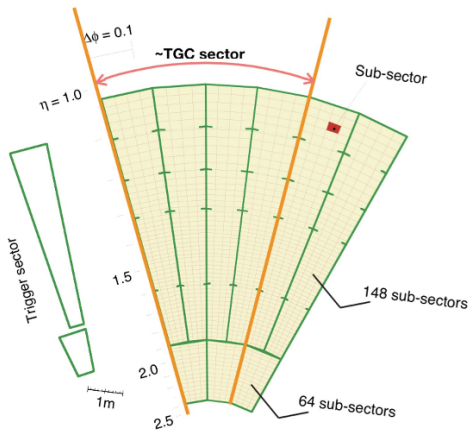

Figure 2.11 TGC sectors.

2.8 Trigger and DAQ

Besides the challenges of the detection and energy measurement of particles, there is another challenge which is the processing and filtering of the large volume of data originating from the particle collisions.

The bunches of protons collide at a rate of 40 MHz with a luminosity of $10^{34} cm^{-2} s^{-1}$ at the LHC, which leads to 10^9 interactions per second. Because it is technically impossible to store such volume of data, pre-selection needs to be employed to select as much of the interesting physics information as possible.

For that reason, trigger and DAQ systems are used. The trigger has to reduce the rate of (In Run2) 40 MHz down to $\sim$ 200 Hz rate for data storage.

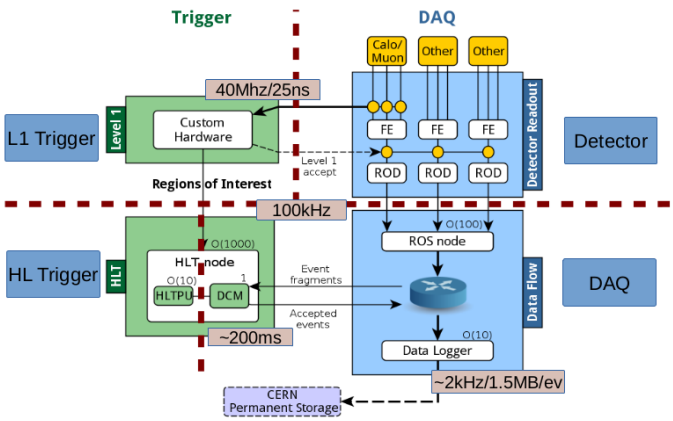

Figure 2.12 Trigger and DAQ scheme in ATLAS.

Three staged filter mechanisms are applied in the ATLAS Trigger system, which is a hardware-based Level 1 (L1) trigger and software-based (L2) and Event Filter (EF) which are together called High-Level Trigger (HLT).

2.8.1 L1 Trigger

The L1 trigger is hardware-based and identifies the regions of interests (ROI) for further processing. It searches for signatures of high p_{T} muons, photons, electrons, jets, and missing and total transverse energy.

The L1 system comprises L1Calo, L1Muon, L1Topo, and a Central Trigger Processor (CTP). L1Calo receives input from LAr and Tile Calorimeters, while L1Muon receives input from TGC and RPC muon trigger detectors. L1Topo has input from both L1Calo

and L1Muon and it allows for topological selections between L1 trigger objects like dR. The CTP has input from all L1 subsystems, and it applies prescales, bunch groups, deadtime, and monitoring of L1 items. In Run2, it supports multi-partition running.

2.8.2 High Level Trigger

High-level trigger (HLT) is composed of Level 2 (L2) and Event Filter (EF). HLT is not based on hardware but is almost entirely based on software algorithms running on computer farms. In Run2, it reduces the rate from 200 kHz seeded from L1 down to 2 kHz (HLT).

L2- Level2 Trigger

L2 is seeded by ROI, which is provided by L1, which gives an advantage of using only a small amount of detector data rather than using full data. This is resulting in short processing times instead of full reconstruction (full scan).

EF- Event Filter

Event filter (EF) uses offline-like analysis tools for processing. It takes a couple of seconds to process the event. On the contrary to L2, it has access to full detector data with a rate of around 200 Hz. Different types of HLT menus are presented at ATLAS by a combination of a different configuration of L1, L2 and EF trigger chains. Because of the storage limitation with these triggers, the bandwidth is balanced between the different ATLAS physics groups.

CHAPTER 3

DATA AND EVENT SELECTION

3.1 Data and MC files

The data samples used in this analysis were recorded by the ATLAS detector in proton-proton collisions at $\sqrt{s}$ = 13 TeV during the 2015-2018 data taking period called Run2. The 2015 pp dataset corresponds to an integrated luminosity of 3.2 fb^{-1}. Selected events are required to be taken during stable beam conditions. For this reason a selection of good event list called GoodRunList (GRL) is applied, the details of GRL is mentioned in Appendix A.1.

Four MC samples have been used in this analysis shown in Table 3.1. The first two samples are B^+ and B^- signal decay process ($B^\pm \rightarrow J/\psi K^\pm \rightarrow \mu^+\mu^- K^\pm$), while the last two samples simulates the wrong mass assignment for B^+ decay, where pion mass assigned to kaon track ($B^+ \rightarrow J/\psi\pi^+$). The samples were generated with PYTHIA8 [35] and EvtGen [36] using the ATLAS A14 tune [37] and CTEQ6L1 [38] pdf . The ATLAS detector and its response were simulated using GEANT4 [39]. To compare the cross-section measurements with theoretical predictions, FONLL [40] with CTEQ6.6 [41] proton distribution function are also used, assuming a hadronisation function ($f_{b\rightarrow B^+}$) of (40.8 $\pm$ 0.7)$\%$ to fix the overall scale [42].

Table 3.1 Data15 and MC16a files used in this analysis.

Type	Name
Data15	data15_13TeV.periodAllYear.physics_Main.PhysCont.DAOD_BPHY5.grp15_v01_p4238
MC16a	mc15_13TeV.300404.Pythia8BEvtGen_A14_CTEQ6L1_Bp_Jpsi_mu3p5mu3p5_Kp_BMassFix.merge.AOD
MC16a	mc15_13TeV.300405.Pythia8BEvtGen_A14_CTEQ6L1_Bm_Jpsi_mu3p5mu3p5_Km_BMassFix.merge.AOD
MC16a	mc15_13TeV.300406.Pythia8BEvtGen_A14_CTEQ6L1_Bp_Jpsi_mu3p5mu3p5_Pip_BMassFix.merge.AOD
MC16a	mc15_13TeV.300437.Pythia8BEvtGen_A14_CTEQ6L1_Bm_Jpsi_mu3p5mu3p5_Pim_BMassFix.merge.AOD

Table 3.2 MC16a Truth0 files used in this analysis.

Type	Name
MC16a	mc15_13TeV.300471.Py8BEG_A14_CTEQ6L1_Bp_Jpsi_mu0p0mu0p0_Kp_BMassFix.evgen.EVNT.e8336
MC16a	mc15_13TeV.300472.Py8BEG_A14_CTEQ6L1_Bm_Jpsi_mu0p0mu0p0_Km_BMassFix.evgen.EVNT.e8336

3.2 Event Selection and Reconstruction of J/ψ Candidates

The first step in event selection is mainly done by the official BPHY5 derivation software [43], which is an Athena-based software used to convert xAOD to DAOD data file format. All primary vertex selection, track fitting and mass reconstruction are finished at this level. Then, with a ROOT [44] and C++-based software (ntuple maker), ntuples with all the candidates are created to study.

In this analysis, the events with one reconstructed primary vertex having three associated ID track is needed. Muon tracks must pass the di-muon trigger which requires the presence of at least two oppositely charged muon candidates of $p_{\mathrm{T}} > 4$ GeV and $|\eta| < 2.5$. These tracks must be reconstructed in the MS and matched with a track in the inner detector, and required to have at least one pixel and four SCT hits, and also muon MCP [45] selection requirements to ensure the accurate ID measurement. The kaon candidates are required to be the loose track as recommended by tracking CP [46], which also satisfies $p_{\mathrm{T}} > 1$ GeV and $|\eta| < 2.5$ condition.

J/ψ reconstruction starts with the trigger selection, two triggers are used in this analysis are shown in the Table 3.3. Events are required to have at least one pair of reconstructed muons, and each pair is fitted using a vertexing algorithm. The fit is applied by constraining each di-muon candidate to a common vertex. The di-muon invariant mass (2.6 GeV $< M_{\mu\mu} <$3.6 GeV) and the quality of the vertex fit ($\chi^2/ndof < 30$) are imposed with very loose selections that are fully efficient for signal candidates. Muon pairs with a common vertex are considered as $J/\psi \to \mu^+\mu^-$ candidates.

Table 3.3 Selected Run2 triggers for 2015 data.

Year	Trigger
2015	HLT_2mu4_bJpsimumu_noL2
2015	HLT_mu6_mu4_bJpsimumu_noL2

3.3 Reconstruction of B^+ Candidates

To reconstruct the $B^{\pm}$ candidates, the muon tracks of the selected J/ψ candidates are fitted to a common vertex with an additional third track of $p_{\mathrm{T}} > 1$ GeV. The three-track fit is performed by constraining the muon tracks to J/ψ mass. The kaon mass is assigned to the third track. In the analysis, the primary vertex with the smallest 3D impact parameter (PV_MIN_A0) is used. The quality of the resulting fit is characterized by the $\chi^2/ndof$, where global χ^2 involving all three tracks is used. Selected candidates are required to fulfill the requirement of $\chi^2/ndof < 4$, the other requirements describing the candidate selections are:

- Transverse decay length of the $B^{\pm}$ meson: $|L_{xy}| > 0.1\ mm$
- Significance of the longitudinal impact parameter : $|z_0/\sigma(z_0)| < 5$
- Significance of the 3D impact parameter: $|a_0/\sigma(a_0)| < 5$
- Production point of the B meson in radial xy plane: $|R_{xy}| < 30\ mm$
- Each $B^{\pm}$ candidate should be in the kinematic range 9 GeV < p_{T} ($B^{\pm}$) < 120 GeV and $|y(B^{\pm})| < 2.5$.

These requirements are considered to clean the signal and are found to be efficient in accepting signal events while strongly rejecting background events. We employ a one candidate per event strategy, which requires first selecting the candidates that passed our analysis cuts defined above, and afterwards selecting the candidate with the lowest $\chi^2/ndof$ as the best candidate and storing it. Table 3.4 summarises the cuts used during the analysis stage, and the optimisation of selected cuts is described at Appendix B.

Table 3.4 $B^{\pm}$ reconstruction cuts.

Cuts	Value
$(J/\psi)\chi^2/ndof$	< 30
$(M_{J/\psi})$	2.6 GeV$< M_{\mu\mu} <$ 3.6 GeV
$(B^{\pm})\chi^2/ndof$	< 4.0
$p_{\mathrm{T}}(K^{\pm})$	> 1 GeV
$p_{\mathrm{T}}(\pi^{\mp})$	> 1 GeV
$\lvert\eta\rvert(K^{\pm})$	< 2.5
$P_T(\mu)$	> 4.0 GeV (each μ)
$\lvert\eta\rvert(\mu)$	< 2.3 (each μ)
Pixel Hit	≥ 1
SCT Hit	≥ 4
$\lvert L_{xy}(B^{\pm})\rvert$	> 0.1 mm
$\lvert z_0/\sigma(z_0)\rvert$	< 5
$\lvert a_{0xy}/\sigma(a_{0xy})\rvert$	< 5
$\lvert R_{xy}\rvert$	< 30 mm
Mass Window	5 GeV < $M_{B^{\pm}}$ < 5.779 GeV
TrackWP	Loose
MuonWP	Tight

CHAPTER 4

YIELD CALCULATION

The first step after getting the B meson candidates as described in the previous section (Section 3.3), is to get the signal yield. Using 9 GeV < p_{T} ($B^{\pm}$) < 120 GeV and $|y(B^{\pm})| < 2.5$ kinematic range, the reconstructed $B^{\pm}$ candidate mass distribution is fitted between 5000 MeV < M($B^{\pm}$) < 5779.26 MeV mass window. p_{T} and y bins used in this analysis are shown below, for the double differential bin, combination of p_{T} and y bin below is used (see Appendix E).

- p_{T} bin ranges: 9, 13, 16, 20, 25, 35, 50, 70, 120 GeV
- y bin ranges: 0, 0.5, 1.0, 1.5, 2.25

To obtain the B^{+} signal yield, by using the RooFit [47] library a C++ program is written, and extended binned maximum likelihood fit is applied to the invariant mass of the candidate. In an extended binned likelihood fit for a signal and multi background model, the probability of obtaining the data in each bin is given by the sum of the probabilities for the signal and background contributions. The likelihood function for such a model can be written in general:

$$\mathcal{L} = \prod_i (n_s \cdot \mathcal{F}_s(m_i, m, \sigma) + n_c \cdot \mathcal{F}_c(m_i, s) + n_{B_x} \cdot \mathcal{F}_{B_x}(m_i, m_{pos}, s) + n_{B_\pi} \cdot \mathcal{F}_{B_\pi}(m_i)) \quad (4.1)$$

$$n = n_s + n_c + n_{B_x} + n_{B_\pi} \quad (4.2)$$

Where n is the total number of events (signal+background) in regarding bin. Here, $\mathcal{L}$ is the likelihood function defines the combination of signal and background probability density functions. n_s is the signal yield, n_c is number of combinatorial background candidates, n_{B_x} is number of partially reconstructed B hadrons candidates, and n_{B_π} is the yield for the decay channel $B^{\pm} \to J/\psi\pi^{\pm}$ that misidentified as $B^{\pm} \to J/\psi K^{\pm}$ candidates, and this fraction is fixed to a value for each bin that derived from MC simulations shown in Equation 4.3.

$$n_{B_\pi} = n_s \cdot \frac{N_{J/\psi\pi^{\pm}}}{N_{J/\psi K^{\pm}}} \quad (4.3)$$

$\mathcal{F}_s$, $\mathcal{F}_c$, $\mathcal{F}_{B_x}$, $\mathcal{F}_{B_\pi}$ and are the probability density functions for the signal and background candidates described in detail below.

- $\mathcal{F}_s$: Signal pdf described with Modified Gaussian

$$P(m, m_0, \sigma) = exp[-0.5 \cdot a^{1+\frac{1}{1+0.5\cdot a}}] \tag{4.4}$$

  where $a = \frac{m-m_0}{\sigma}$, m is the mass of the B^+ meson candidate, and m_0 is the expected mass of the B^+ candidate. σ is the width of the gaussian.

- $\mathcal{F}_c$: Combinatorial background pdf represented with exponential function. The sources of combinatorial background is either from the random combination of J/ψ daughter muons or of di-muon with a random track from other B-hadron decays.

$$P(m, s) = exp(s \cdot m) \tag{4.5}$$

  where, m is the mass of the B meson candidate and s is a constant defining the slope in our case.

- $\mathcal{F}_{B_x}$: Pdf for the partially reconstructed B hadrons, which are misidentified as signal candidate described by the complementary error function (erfc).

$$P(m, m_{pos}, s) = 1 - erf(\frac{m_0 - m_{pos}}{s}) \tag{4.6}$$

  where, m is the mass of the candidate, m_{pos} is the position of the partially reconstructed hadron mass and s is the slope of the complimentary error function.

- $\mathcal{F}_{B_\pi}$: Pdf describing the background due to $B^\pm \to J/\psi\pi^\pm$ decay, in which the kaon mass is wrongly assigned to charged pion. Kernel density estimator (KDE) is used as pdf and shape information is collected from MC files. This decay is Cabibbo-suppressed with a relative ratio shown in Equation 4.7 with respect to signal with the world averaged values from PDG [48]. Then the R value in Equation 4.7 is corrected with efficiency(ϵ) and acceptance ($\mathcal{A}$) resulting in Equation 4.8 before using in the fit.

$$R = \frac{\mathcal{B}(B^+ \to J/\psi\pi^+)}{\mathcal{B}(B^+ \to J/\psi K^+)} = (3.85 \pm 0.04) \times 10^{-2} \tag{4.7}$$

$$R(p_{\mathrm{T}}, |y|) = R \cdot \frac{\epsilon_{J/\psi\pi^\pm} \cdot \mathcal{A}_{J/\psi\pi^\pm}}{\epsilon_{J/\psi K^\pm} \cdot \mathcal{A}_{J/\psi K^\pm}} \tag{4.8}$$

In Figure 4.1 the quality of fit is described by the pull distribution shown at the bottom pad of the figure. The pull in RooFit is defined as :

$$\text{pull} = \frac{N^{data} - N^{fit}}{\sigma^{fit}} \tag{4.9}$$

Where N^{data} is the number of candidate in given bin in data, N^{fit} the prediction of number of candidate from the fit within a statistical uncertainty σ^{fit}.

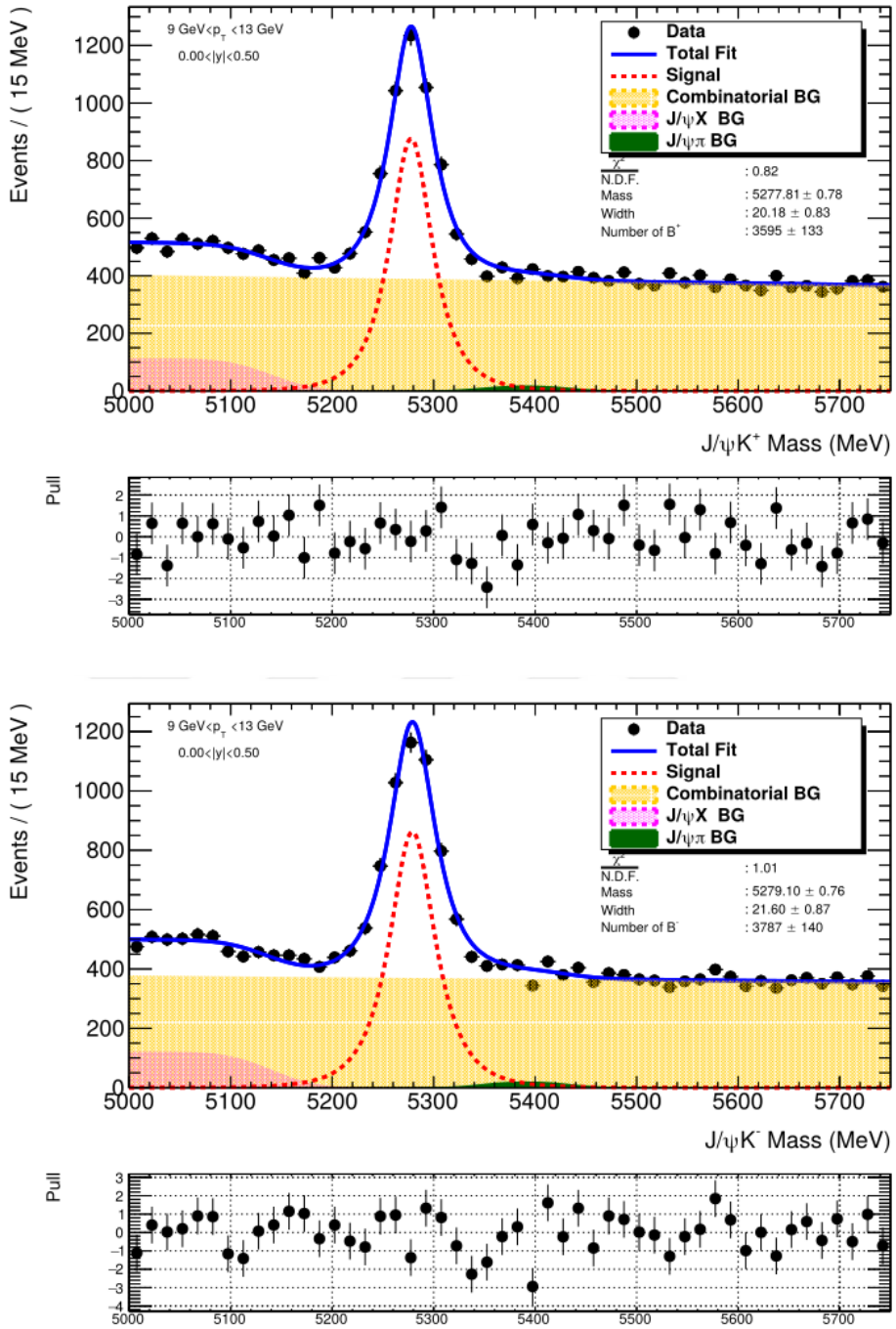

Figure 4.1 B^+ (up) and B^- (down) fit result for the first double differential bin. Where black dots with error bars shows the data, blue line shows the total fit, red dotted line shows the signal, orange color is combinatorial background, pink color is partially reconstructed b-hadron background and green area at the bottom is the wrongly assigned charged pion mass background.

CHAPTER 5

EVENT REWEIGHTING

Production of MC files requires a lot of time and resources. Because of this, the analysis teams typically created official MC sets prior to or during the time of data collection. As a result, it was impossible to reproduce the trigger, detector state, pileup conditions, etc. precisely. Correcting MC to accurately depict the data is necessary to minimize the effect.

Each event is assigned a weight, and Equation 5.1 and 5.2 are used to determine the total weight of a certain event. These are corrections for the reconstructed and generator levels. The correction at the generator level both affects the acceptance and efficiency. The acceptance and efficiency are both impacted by the generator-level correction.

$$w_i^{Reco} = w_{Pre} \times w_{Trg} \times w_{\mu_{Reco}} \times w_{PVz} \times w_{pT} \times w_{|y|} \tag{5.1}$$

$$w_i^{Gen} = w_{PVz} \times w_{pT} \times w_{|y|} \tag{5.2}$$

Where w_i^{Reco} is reconstructed level weight and w_i^{Gen} is the generator level weight which are :

- w_{Pre}: Trigger prescale. Prescale factor for HLT_2mu4_bjpsimumu_noL2 is calculated with a straightforward procedure, by taking the ratio with an unprescaled trigger luminosity(given in Table A.2), it is resulted with the Equation 5.3 .The prescale is only applied to event with 2mu4 trigger, otherwise no prescale is applied.

$$w_{Pre} = \frac{\mathcal{L}_{2mu4}}{\mathcal{L}_{mu6mu4}} = \frac{2569.98\, pb^{-1}}{3214.54\, pb^{-1}} = 0.799486 \tag{5.3}$$

- w_{Trg}: Trigger scale factor, which is calculated from the Equation D.1 in Appendix D.1.5 and detail for di-muon trigger scale factor is described at Appendix C.1.
- $w_{\mu_{Reco}}$: Muon Reconstruction correction, described in Appendix D.6.

- w_{PVz}: Primary vertex z point weight which is defined in Appendix D.2.
- w_{pT}: p_{T} bin weight, described in Appendix D.4.
- $w_{|y|}$: $|y|$ bin weight, described in Appendix D.5.

The Equation 5.4 is used to calculate the central values of the weighted events in the $p_{\mathrm{T}}, |y|$ bin. We are following the conservative approach to determine the uncertainty, which is shown in the Equation 5.5.

$$w(p_{\mathrm{T}}, |y|) = \sum_{i=1}^{nEvent} (w_i) \tag{5.4}$$

$$\sigma(p_{\mathrm{T}}, |y|) = \sqrt{\sum_{i=1}^{nEvent} (w_i^2)} \tag{5.5}$$

CHAPTER 6

CROSS SECTION CALCULATION

The corrected number of B meson candidates determined from fitted data and weighted MC are required to calculate the cross-section.

The cross-section for p_{T}, y and double differential bins are described as:

$$\frac{d\sigma(pp \to B^+X)}{dp_T} = \frac{N^{B^+}}{\mathcal{L} \cdot \beta \cdot \Delta p_T} \tag{6.1}$$

$$\frac{d\sigma(pp \to B^+X)}{dy} = \frac{N^{B^+}}{\mathcal{L} \cdot \beta \cdot \Delta y} \tag{6.2}$$

$$\frac{d^2\sigma(pp \to B^+X)}{dp_T dy} = \frac{N^{B^+}}{\mathcal{L} \cdot \beta \cdot \Delta p_T \Delta y} \tag{6.3}$$

Where;

- $\mathcal{L}$ is the integrated luminosity of the data file. Which is $(5.9968 \pm 0.3311) \times 10^{-5}$.
- $\mathcal{B}$ is the total branching ratio obtained by combining the world averaged values of the branching ratios for $\mathcal{B}(B^+ \to J/\psi K^+) = (1.006 \pm 0.027) \times 10^{-3}$ and $\mathcal{B}(J/\psi \to \mu^+\mu^-) = (5.961 \pm 0.033) \times 10^{-2}$ from the PDG2020 [48].
- Δp_T and Δy are the widths of transverse momentum and rapidity intervals respectively.
- N^{B^+} is the number of $B^+ \to J/\psi K^+$ signal candidates of data, which is extracted from fit and corrected with efficiency and acceptance.

$$N^{B^+} = \frac{1}{\mathcal{A}^{B^+}} \frac{N^{B^+}_{data}}{\varepsilon^{B^+}} \tag{6.4}$$

The Acceptance $\mathcal{A}$ and Efficiency ϵ in Equation 6.4 is defined as below:

$$\mathcal{A}^{B^+}(p_{\mathrm{T}}, |y|) = \frac{N^{det}_{gen}(p_{\mathrm{T}}, |y|)}{N_{gen}(p_{\mathrm{T}}, |y|)} \tag{6.5}$$

Where, $N_{gen}(p_{\mathrm{T}}, |y|)$ is the number of generated signal candidates in $p_{\mathrm{T}}, |y|$ phase space. The efficiency is defined as :

$$\epsilon^{B^+}(p_{\mathrm{T}}, |y|) = \frac{N_{reco}^{B^+}(p_{\mathrm{T}}, |y|)}{N_{gen}^{det}(p_{\mathrm{T}}, |y|)} \tag{6.6}$$

Where, $N_{gen}^{det}(p_{\mathrm{T}}, |y|)$ is the number of candidate seen by the detector determined from final state particles in that p_{T} and y phase space in generator level. $N_{reco}^{B^+}(p_{\mathrm{T}}, |y|)$ is the number of B^+ candidates that passes all our analysis cuts in reconstructed level.

For B^- candidates, we are using charge conjugates of the above formulas. Cross-sections are calculated both for B^+ and B^- separately and $B^\pm$ cross-section is defined as the mean of the two cross-section which shown in Equation 6.7 .

$$\sigma_{B^\pm} = (\sigma_{B^+} + \sigma_{B^-})/2 \tag{6.7}$$

CHAPTER 7

SYSTEMATIC UNCERTAINTIES

7.1 Introduction

Identifying all the relevant sources of systematic uncertainty in a consistent manner may be the most difficult part of evaluating systematic uncertainties. This requires a solid understanding of the measurement's nature, the underlying or apparent assumptions in the measurement procedure, and the uncertainties and assumptions incorporated in any theoretical models used to interpret the results [49].

The following groups of systematic uncertainty sources are taken into account:

- $\{\delta_1\}$ The uncertainty of the trigger efficiencies.
- $\{\delta_2\}$ The uncertainty of the muon reconstruction described in Section 7.6.
- $\{\delta_3\}$ The uncertainty of the hadron track reconstruction described in Section 7.5.
- $\{\delta_4\}$ The uncertainty of the acceptance and efficiency corrections related to the MC statistical uncertainty.
- $\{\delta_5\}$ The model dependence of the acceptance and efficiency corrections. It is obtained by varying in the MC simulation the $p_{\mathrm{T}}(B^+)$ and $|y(B^+)|$ distributions while preserving agreement with the data distributions.
- $\{\delta_6\}$ The uncertainty of the B^+ signal extraction procedure is explained in Section 7.9.
- $\{\delta_7\}$ The uncertainty of the luminosity measurement described in the Section 7.10.
- $\{\delta_8\}$ The uncertainty of the branching fraction discussed in the Section 7.11

The systematic uncertainties are summarized in Table 7.4 and 7.5. Contributions from the systematic uncertainties $\delta_1 - \delta_6$, calculated for visible cross sections and all bins

of the differential cross-sections, are added in quadrature separately for positive and negative variations. Uncertainties linked with the luminosity measurement (δ_7) and branching fractions (δ_8) are quoted separately for the measured visible cross sections. For differential cross-sections, the δ_7 and δ_8 uncertainties are not included in Tables 8.1–8.2 and Figures. 7.3–7.4

7.2 nPv Systematic

To determine the systematic for the number of primary vertices, the cross section is estimated both with and without considering the official pile up reweighting (PRW) tool [50]; the variation is considered as systematic uncertainty. The PRW tool is used to determine the central value, and the technique is outlined in Section D.3.2.

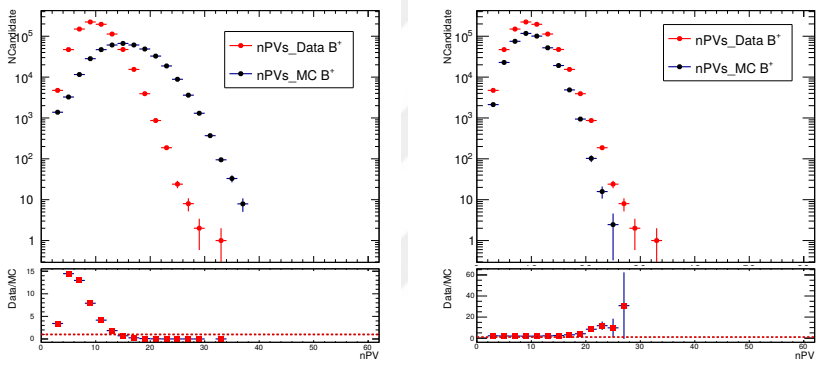

Figure 7.1 The number of primary vertex distribution for B^+ before(Left) and after(Right) using official pileup reweighting tool. The red points are the Data, the blue points are MC.

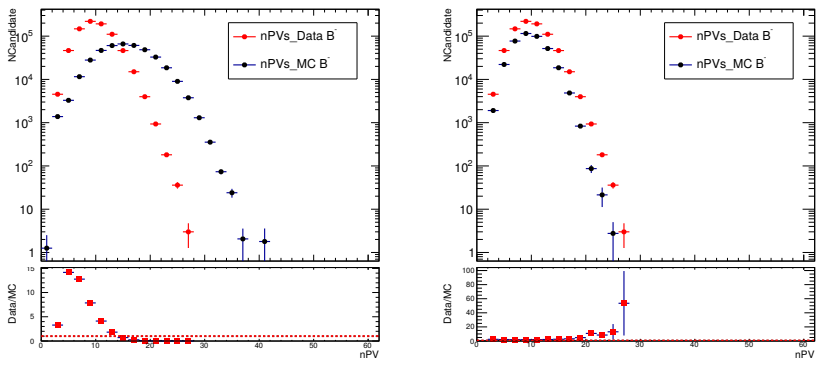

Figure 7.2 The number of primary vertex distribution for B^- before(Left) and after(Right) using official pileup reweighting tool. The red points are the Data, the blue points are MC.

7.3 $|y|$ and PV_z Systematic

Both $|y|$ and PV_z corrections are defined as first order polynomial functions.

$$y = a_0 + a_1 x = a_0(1 + \frac{a_1}{a_0}x) = a_0(1 + sx) \tag{7.1}$$

The uncertainty of a_0 is irrelevant because "a_0" is the same for all events at both detector and true levels, i.e., it produces no effect on cross-sections. Uncertainty in s produces the corresponding systematics in the following way:

- Recalculate x-sections using $s = s + \sigma(s)$, with x-section changes representing systematic uncertainties (in one direction).
- Recalculate x-sections using $s = s - \sigma(s)$, with x-section changes representing systematic uncertainties (in another direction).

If both variations result in x-section changes in one direction, the largest one is selected as systematic uncertainties.

7.4 p_{T} Systematic

The p_{T} weight is calculated from the hyperbolic function defined in Equation 7.2.

$$y(x) = a_0 - \frac{a_0 \cdot a_1}{x - a_2} = a_0(1 - \frac{a_1}{x - a_2}) \tag{7.2}$$

The systematic resulting from the p_{T} reweighting is calculated as follows:

- Fix a_1 to $a_1 + \sigma_{a_1}$ and get the fit function with a_0 and a_2 as free parameter. Calculate the cross section with new fit function.
- Fix a_1 to $a_1 - \sigma_{a_1}$ and get the fit function with a_0 and a_2 as free parameter. Calculate the cross section with new fit function.
- Fix a_2 to $a_2 + \sigma_{a_2}$ and get the fit function with a_0 and a_1 as free parameter. Calculate the cross section with new fit function.
- Fix a_2 to $a_2 - \sigma_{a_2}$ and get the fit function with a_0 and a_1 as free parameter. Calculate the cross section with new fit function.

Then choose the largest positive and negative cross section variation out of the four variations as positive or negative systematic uncertainties. Central $|y|$ calculations are used in p_{T} reweighting systematic.

7.5 Tracking Systematics

For the tracking systematics, the recipe in the Tracking CP [46] twiki page is used. In this analysis, loose working point is chosen. Two principal sources of uncertainty are considered for the track reconstruction efficiency.

- Material uncertainties.
- Physics model used in simulation.

The four p_{T}/η 2D histograms provided by the Tracking CP are employed, corresponding to four sources of tracking systematics. Each track is assigned a weight equal to (1-error), where the error is the quadratic sum of the values retrieved from the four histograms. The following are the loose working point scale factor histograms("OneMinusRatioEfficiencyVSEtaPt_AfterRebinning_"):

- "NominalVSOverall_5_Loose": Passive material of the ID scaled by 5% (Sys + 5% Extra).
- "NominalVSIBL_10_Loose": Passive material of the IBL scaled by 10% (SysIBLExtra)
- "NominalVSPP0_25_Loose": Passive material in the PP0 region scaled by 25% (SysPixServExtra)
- "NominalVSQGS_BIC_Loose": Change in the G4 physics model from FTFP BERT to QGSP_BIC (SysPhysModel)

$$\sigma_{\epsilon_{trk}} = \sqrt{\sigma^2_{Overall} + \sigma^2_{IBL} + \sigma^2_{PP0} + \sigma^2_{QGS_BIC}} \tag{7.3}$$

$$W_{trk} = 1 \pm \sigma_{\epsilon_{trk}} \tag{7.4}$$

Equation 7.3 is used to compute efficiency variation, while Equation 7.4 is utilized to calculate weight for systematic calculation. Cross-section variation is used as a systematic for tracking efficiency.

7.6 Muon Reconstruction Systematics

Systematics on muon reconstruction efficiency scale factors are calculated with the official tool [51] which is recommended in the MCP guidelines [45]. Tool provides 4 points with the central values which are:

- **MUON_EFF_STAT**: Statistical error on the SF. Variations by +1 or -1 sigma.
- **MUON_EFF_SYS**: Systematic error on the SF. Variations by +1 or -1 sigma.
- **MUON_EFF_STAT_LOWPT**: Stat error on the low p_{T} component of the SF. Variations by +1 or -1 sigma.
- **MUON_EFF_SYS_LOWPT**: Sys error on the low p_{T} component of the SF. Variations by +1 or -1 sigma.

Up(H) and down(L) values are the variations around the central value by +1 or -1 sigma.

$$\delta^{H}_{\mu_{Reco}} = |\sigma_{Central} - \sigma_{High}| \tag{7.5}$$

$$\delta^{L}_{\mu_{Reco}} = |\sigma_{Central} - \sigma_{Low}| \tag{7.6}$$

Where, $\sigma_{Central}$ is the central value of the x-section calculated with the central value of the related weights, σ_{High} is the x-section calculated with the $w_{\mu} + 1\sigma_{SF}$ weight, and σ_{Low} is the x-section calculated with the $w_{\mu} - 1\sigma_{SF}$ weight.

For each, the difference between the central values ($\delta^{H}_{\mu_{Reco}}$ and $\delta^{L}_{\mu_{Reco}}$) is computed, and the highest one is used as $\delta_{\mu_{Reco}}$ systematic.

7.7 Lxy Systematics

7.7.1 Overview

Another source of systematics study is the lifetime of the B^{+} meson, which can be calculated by varying the L_{xy} cut. The $B^{\pm}$ mean lifetime in PDG is

$$(1.638 \pm 0.004)x10^{-12}\,\mathrm{sec} \tag{7.7}$$

The relative uncertainty is

$$\delta_{Lxy} = 0.004/1.63 = 0.002442 \tag{7.8}$$

The systematics is calculated by varying the L_{xy} cut as 0.1 ± 0.0002442 . The results are included in Table 7.4.

7.7.2 Lxy Uncertainty due to Detector Resolution

To analyze the lifetime, the detector resolution, and the uncertainty effect, an MC16a ntuple with $L_{xy} > 0$ is created. First we checked the corrected L_{xy} defined as Lxy_{Corr}.

10% difference from the central value is taken into consideration to control the Lxy_{Corr}

$$\Delta_{Lxy} = Lxy^{true} - Lxy^{reco} \tag{7.9}$$

$$Lxy_{Corr}^{Central} = Lxy^{true} - (1.0 \times \Delta_{Lxy}) \tag{7.10}$$

$$Lxy_{Corr}^{Up} = Lxy^{true} - (1.1 \times \Delta_{Lxy}) \tag{7.11}$$

$$Lxy_{Corr}^{Down} = Lxy^{true} - (0.9 \times \Delta_{Lxy}) \tag{7.12}$$

By using above equations and using the cut below in every event.

$$Lxy^{reco} > Lxy_{Corr} \tag{7.13}$$

$$\delta_{Lxy_{Corr}^{Up}}[\%] = \frac{|Lxy_{Corr}^{Up} - Lxy_{Corr}^{Central}|}{Lxy_{Corr}^{Central}} \tag{7.14}$$

$$\delta_{Lxy_{Corr}^{Down}}[\%] = \frac{|Lxy_{Corr}^{Central} - Lxy_{Corr}^{Down}|}{Lxy_{Corr}^{Central}} \tag{7.15}$$

Systematics relating with the detector resolution studied in p_{T}, y, and double differential bins are shown at the Tables 7.1, 7.2, 7.3 and found to be small.

Table 7.1 δ_{Lxy} [%] relative ratio in p_{T} bin.

p_{T} [GeV]		$\delta_{Lxy_{Corr}}(B^{\pm})$[%]		$\delta_{Lxy_{Corr}}(B^{+})$ [%]		$\delta_{Lxy_{Corr}}(B^{-})$[%]	
min	max	$\delta_{Lxy_{Corr}^{Up}}$	$\delta_{Lxy_{Corr}^{Down}}$	$\delta_{Lxy_{Corr}^{Up}}$	$\delta_{Lxy_{Corr}^{Down}}$	$\delta_{Lxy_{Corr}^{Up}}$	$\delta_{Lxy_{Corr}^{Down}}$
9.0	13.0	0.013	0.038	0.006	0.067	0.018	0.012
13.0	16.0	0.042	0.005	0.024	0.034	0.061	0.023
16.0	20.0	0.051	0.036	0.045	0.018	0.057	0.054
20.0	25.0	0.019	0.063	0.016	0.047	0.054	0.080
25.0	35.0	0.041	0.054	0.031	0.054	0.051	0.053
35.0	50.0	0.057	0.032	0.042	0.006	0.072	0.070
50.0	70.0	0.071	0.000	0.028	0.023	0.113	0.023
70.0	120.0	0.098	0.002	0.117	0.088	0.079	0.085

Table 7.2 δ_{Lxy} [%] relative ratio in y bin.

$\|y\|$		$\delta_{Lxy_{Corr}}(B^{\pm})$[%]		$\delta_{Lxy_{Corr}}(B^{+})$ [%]		$\delta_{Lxy_{Corr}}(B^{-})$[%]	
min	max	$\delta_{Lxy_{Corr}^{Up}}$	$\delta_{Lxy_{Corr}^{Down}}$	$\delta_{Lxy_{Corr}^{Up}}$	$\delta_{Lxy_{Corr}^{Down}}$	$\delta_{Lxy_{Corr}^{Up}}$	$\delta_{Lxy_{Corr}^{Down}}$
0.0	0.5	0.044	0.034	0.071	0.047	0.019	0.021
0.5	1.0	0.013	0.019	0.002	0.025	0.028	0.013
1.0	1.5	0.016	0.037	0.044	0.069	0.010	0.008
1.5	2.25	0.057	0.035	0.019	0.065	0.093	0.005

Table 7.3 δ_{Lxy} [%] in double differential bin.

p_{T} [GeV]		$0.0 < \|y\| < 0.5$		$0.5 < \|y\| < 1.0$	
min	max	$\delta_{L_{xy}^{Up}}$ $(B^{\pm})$[%]	$\delta_{L_{xy}^{Down}}$ $(B^{\pm})$[%]	$\delta_{L_{xy}^{Up}}$ $(B^{\pm})$[%]	$\delta_{L_{xy}^{Down}}$ $(B^{\pm})$[%]
9.0	13.0	0.036	0.000	0.014	0.023
13.0	16.0	0.059	0.001	0.035	0.004
16.0	20.0	0.056	0.000	0.070	0.016
20.0	25.0	0.028	0.000	0.048	0.031
25.0	35.0	0.054	0.001	0.033	0.050
35.0	50.0	0.139	0.001	0.110	0.065
50.0	70.0	0.087	0.000	0.083	0.154
70.0	120.0	0.166	0.000	0.207	0.006
p_{T} [GeV]		$1.0 < \|y\| < 1.5$		$1.5 < \|y\| < 2.25$	
min	max	$\delta_{L_{xy}^{Up}}$ $(B^{\pm})$[%]	$\delta_{L_{xy}^{Down}}$ $(B^{\pm})$[%]	$\delta_{L_{xy}^{Up}}$ $(B^{\pm})$[%]	$\delta_{L_{xy}^{Down}}$ $(B^{\pm})$[%]
9.0	13.0	0.001	0.000	0.081	0.051
13.0	16.0	0.001	0.000	0.017	0.005
16.0	20.0	0.000	0.001	0.026	0.002
20.0	25.0	0.000	0.002	0.047	0.066
25.0	35.0	0.000	0.000	0.049	0.075
35.0	50.0	0.000	0.000	0.046	0.031
50.0	70.0	0.001	0.001	0.019	0.165
70.0	120.0	0.001	0.000	0.122	0.000

7.8 MC Systematics

The systematic uncertainties $\delta_1 - \delta_5$ are derived from MC reweighting, and δ_{MC} is calculated using Equation 7.16, with the final results are shown in Table 7.6 in double differential bins.

$$\delta_{MC} = \sqrt{\delta_{L_{xy}}^2 + \delta_{\mu}^2 + \delta_{p_{\mathrm{T}}}^2 + \delta_{Track}^2 + \delta_{vz}^2 + \delta_{Y}^2 + \delta_{Eff}^2} \tag{7.16}$$

The δ_{MC}[%] calculations are shown in the Table 7.6.

Table 7.4 δ_{MC} [%] in double differential bin.

p_T [GeV]		$0.0 < \|y\| < 0.5$								$0.5 < \|y\| < 1.0$							
min	max	$\delta_{L_{xy}}$	δ_μ	δ_{p_T}	δ_{Track}	δ_{vz}	δ_Y	δ_{Eff}	δ_{Total}	$\delta_{L_{xy}}$	δ_μ	δ_{p_T}	δ_{Track}	δ_{vz}	δ_Y	δ_{Eff}	δ_{Total}
9.0	13.0	0.03	2.80	3.14	0.38	0.00	0.00	0.50	4.25	0.02	2.84	3.26	0.47	0.00	0.00	0.50	4.38
13.0	16.0	0.02	2.37	0.30	0.39	0.00	0.01	0.50	2.47	0.01	2.24	0.33	0.45	0.00	0.00	0.50	2.36
16.0	20.0	0.03	2.15	0.14	0.44	0.00	0.01	0.50	2.26	0.01	1.90	0.15	0.47	0.00	0.00	0.50	2.03
20.0	25.0	0.01	1.99	0.06	0.50	0.00	0.01	0.50	2.11	0.02	1.66	0.06	0.49	0.00	0.00	0.50	1.80
25.0	35.0	0.02	1.68	0.04	0.55	0.00	0.01	0.50	1.84	0.00	1.37	0.04	0.52	0.02	0.02	0.50	1.54
35.0	50.0	0.01	1.43	0.14	0.74	0.14	0.15	0.50	1.70	0.01	1.03	0.00	0.53	0.00	0.00	0.50	1.26
50.0	70.0	0.00	1.01	0.00	0.61	0.00	0.01	0.50	1.28	0.00	0.78	0.01	0.54	0.00	0.01	0.50	1.07
70.0	120.0	0.00	0.76	0.03	0.62	0.01	0.01	0.50	1.11	0.00	0.64	0.03	0.55	0.00	0.01	0.50	0.98

p_T [GeV]		$1.0 < \|y\| < 1.5$								$1.5 < \|y\| < 2.25$							
min	max	$\delta_{L_{xy}}$	δ_μ	δ_{p_T}	δ_{Track}	δ_{vz}	δ_Y	δ_{Eff}	δ_{Total}	$\delta_{L_{xy}}$	δ_μ	δ_{p_T}	δ_{Track}	δ_{vz}	δ_Y	δ_{Eff}	δ_{Total}
9.0	13.0	0.01	3.10	3.35	0.70	0.00	0.03	0.50	4.65	0.02	2.53	3.29	1.00	0.00	0.02	0.50	4.30
13.0	16.0	0.03	2.53	0.32	0.68	0.16	0.13	0.50	2.69	0.01	1.95	0.37	1.09	0.01	0.03	0.50	2.32
16.0	20.0	0.01	1.87	0.16	0.71	0.07	0.01	0.50	2.07	0.02	1.61	0.15	1.19	0.00	0.01	0.50	2.06
20.0	25.0	0.06	1.71	0.06	0.92	0.01	0.21	0.50	2.02	0.01	1.33	0.05	1.27	0.00	0.01	0.50	1.91
25.0	35.0	0.01	1.39	0.04	0.76	0.00	0.01	0.50	1.66	0.00	1.14	0.04	1.40	0.01	0.02	0.50	1.87
35.0	50.0	0.00	1.12	0.02	0.76	0.00	0.03	0.50	1.44	0.02	0.93	0.01	1.47	0.02	0.02	0.50	1.81
50.0	70.0	0.00	0.89	0.02	0.75	0.00	0.01	0.50	1.26	0.00	0.73	0.09	1.54	0.08	0.05	0.50	1.78
70.0	120.0	0.00	0.93	0.09	0.76	0.07	0.07	0.50	1.31	0.00	0.70	0.01	1.57	0.01	0.01	0.50	1.79

7.9 Fit Systematic

Fit systematic (δ_6) is sourcing from the B^+ yield operations (fits) and calculated as

$$\delta_{Fit} = \sqrt{\delta^2_{Signal} + \delta^2_{JpsiX} + \delta^2_{Comb} + \delta^2_{PDG}} \tag{7.17}$$

Two systematic checks are performed for each central PDF, and the best one is chosen to serve as that central PDF's systematic. Where each component is described as:

- δ_{Signal} is the uncertainty from the signal PDF
  - ∗ **Central:** Modified Gaussian
  - ∗ 1st **Systematic Check:**Double Modified Gaussian
  - ∗ 2nd **Systematic Check:** Johnson + Modified Gaussian
- δ_{JpsiX} is the uncertainty from the partially reconstructed hadron background PDF.
  - ∗ **Central:** Erfc
  - ∗ 1st **Systematic Check:**TanH
  - ∗ 2nd **Systematic Check:** Argus $\otimes$ Gaussian
- δ_{Comb} is the uncertainty from the combinatorial background PDF.
  - ∗ **Central:** Exponential PDF.
  - ∗ 1st **Systematic Check:** Exponential with 2nd order polynomial.
  - ∗ 2nd **Systematic Check:** 2nd order polynomial.

- δ_{PDG} is the uncertainty from the $J/\psi\pi^{\pm}$ background ratio described in Equation 4.7. The central value is fixed with the ratio and the associated systematic is sourced from the PDG value, which is propagated with efficiency and acceptance correction.

$\delta_{Fit}[\%]$ components in double differential bin are shown at the Figure 7.5. Each of the four central PDF's final systematic and also the total systematic, which is calculated by Equation 7.17 is shown in the table.

Table 7.5 δ_{Fit} [%] in double differential bin.

p_T [GeV]		$0.0 < \|y\| < 0.5$					$0.5 < \|y\| < 1.0$				
min	max	δ_{Signal}	δ_{Comb}	δ_{JpsiX}	δ_{PDG}	δ_{Total}	δ_{Signal}	δ_{Comb}	δ_{JpsiX}	δ_{PDG}	δ_{Total}
9.0	13.0	0.01	0.19	0.59	0.02	0.62	0.06	0.17	0.78	0.07	0.80
13.0	16.0	0.54	0.53	0.55	0.54	1.09	0.00	0.27	0.73	0.01	0.78
16.0	20.0	0.01	0.05	0.09	0.01	0.11	0.15	0.15	0.33	0.05	0.40
20.0	25.0	0.00	0.09	0.06	0.00	0.11	0.01	0.13	0.38	0.01	0.40
25.0	35.0	0.00	0.00	0.21	0.01	0.21	0.01	0.16	0.24	0.01	0.29
35.0	50.0	0.01	0.08	0.26	0.03	0.27	0.01	0.08	0.14	0.02	0.17
50.0	70.0	0.02	0.18	0.10	0.07	0.22	0.08	0.21	0.45	0.09	0.51
70.0	120.0	2.27	2.25	2.02	2.45	4.51	0.07	1.19	0.45	0.22	1.29
p_T [GeV]		$1.0 < \|y\| < 1.5$					$1.5 < \|y\| < 2.25$				
min	max	δ_{Signal}	δ_{Comb}	δ_{JpsiX}	δ_{PDG}	δ_{Total}	δ_{Signal}	δ_{Comb}	δ_{JpsiX}	δ_{PDG}	δ_{Total}
9.0	13.0	0.03	0.33	0.49	0.02	0.59	0.07	1.88	1.48	0.02	2.40
13.0	16.0	0.41	0.40	0.44	0.41	0.83	0.01	1.96	1.33	0.00	2.37
16.0	20.0	0.00	0.20	0.41	0.01	0.45	0.07	1.72	1.20	0.07	2.10
20.0	25.0	0.01	0.27	0.57	0.01	0.63	0.01	1.52	2.02	0.02	2.52
25.0	35.0	0.01	0.32	0.36	0.01	0.48	0.02	0.87	1.10	0.02	1.40
35.0	50.0	0.01	0.31	0.26	0.03	0.40	0.07	1.86	1.96	0.09	2.71
50.0	70.0	0.30	0.29	0.12	0.06	0.44	0.14	3.47	3.28	0.17	4.78
70.0	120.0	0.27	1.13	1.15	0.17	1.65	1.76	3.83	2.95	1.92	5.49

7.10 Luminosity Systematic

Uncertainty in the integrated luminosity for 2015 data [12] is described in Equation 7.18:

$$\delta_8 = 2.1\,\% \tag{7.18}$$

7.11 BR Systematic

The δ_8 is calculated from the PDG Branching ratio.

$$BR(B^{\pm} \to J/\psi K^{\pm}) \times BR(J/\psi \to \mu^+\mu^-) = (6.08022 \pm 0.118155) \times 10^{-5} \tag{7.19}$$

$$\delta_9 = 1.94\,\% \tag{7.20}$$

7.12 Total Systematic

Total systematic and statistical uncertainties [%] in double differential bins

Table 7.6 Total systematic and statistical uncertainties [%] in double differential bins.

p_T [GeV]		$0.0 < \|y\| < 0.5$			$0.5 < \|y\| < 1.0$		
min	max	Syst[%]	Stat[%]	Syst $\oplus$ Stat	Syst[%]	Stat[%]	Syst $\oplus$ Stat
9.0	13.0	4.30	2.73	5.09	4.45	3.70	5.79
13.0	16.0	2.70	1.83	3.26	2.49	2.21	3.33
16.0	20.0	2.26	1.57	2.75	2.07	1.83	2.76
20.0	25.0	2.12	1.71	2.72	1.85	2.18	2.85
25.0	35.0	1.85	1.58	2.44	1.57	1.71	2.32
35.0	50.0	1.72	2.46	3.00	1.27	2.57	2.86
50.0	70.0	1.30	4.67	4.84	1.19	5.08	5.21
70.0	120.0	4.64	8.11	9.34	1.62	7.97	8.13
p_T [GeV]		$0.0 < \|y\| < 0.5$			$0.5 < \|y\| < 1.0$		
min	max	Syst[%]	Stat[%]	Syst $\oplus$ Stat	Syst[%]	Stat[%]	Syst $\oplus$ Stat
9.0	13.0	4.69	5.71	7.39	4.92	6.56	8.20
13.0	16.0	2.82	2.80	3.98	3.32	4.04	5.23
16.0	20.0	2.12	2.19	3.05	2.94	3.14	4.31
20.0	25.0	2.11	2.08	2.96	3.16	3.23	4.52
25.0	35.0	1.73	1.99	2.63	2.34	3.09	3.88
35.0	50.0	1.50	3.03	3.38	3.26	5.42	6.33
50.0	70.0	1.34	5.48	5.64	5.10	5.00	7.14
70.0	120.0	2.10	10.43	10.64	5.78	26.60	27.22

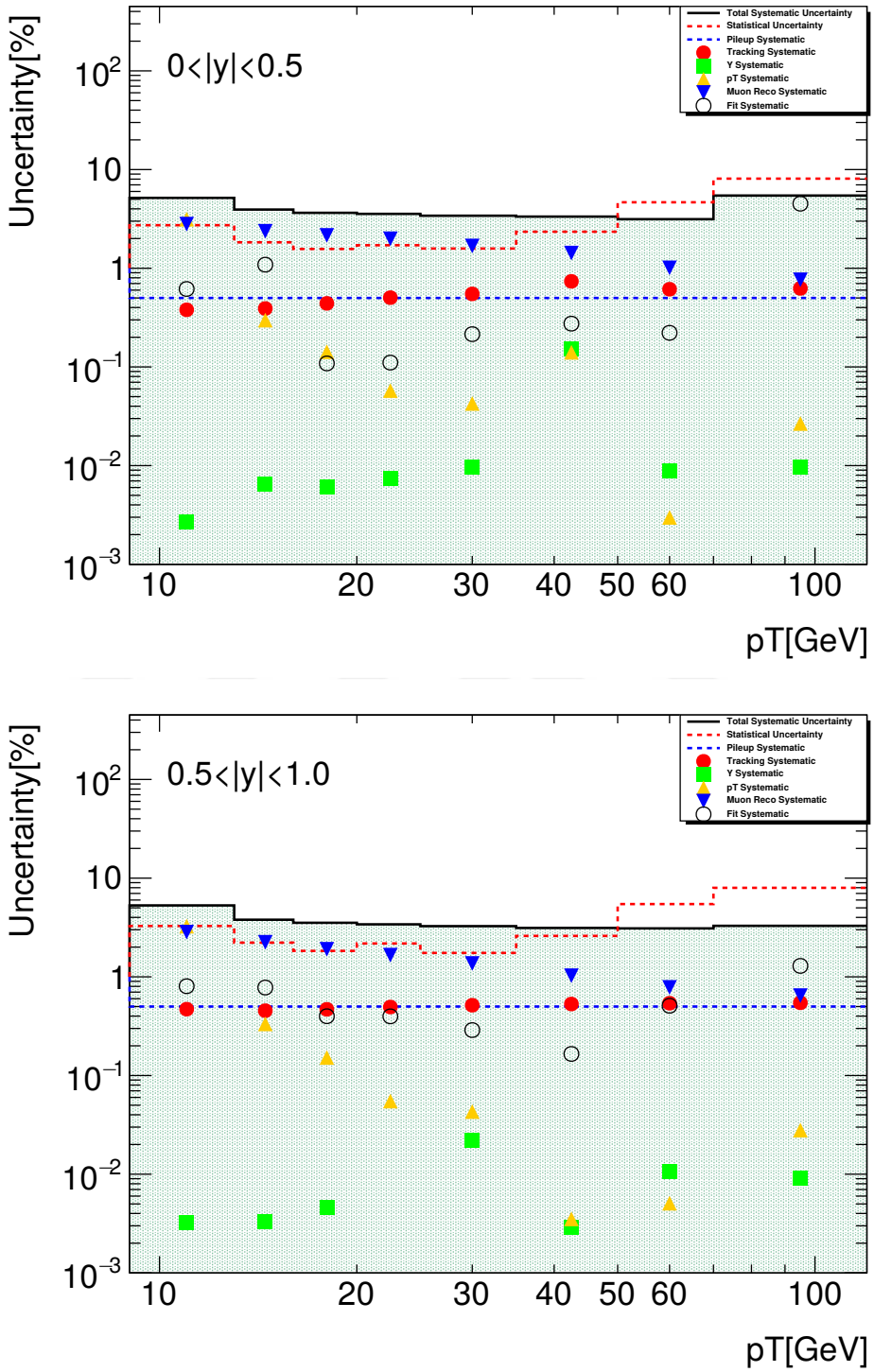

Figure 7.3 Percentage systematic and statistical uncertainties in double differential bins, for the first two y bins.

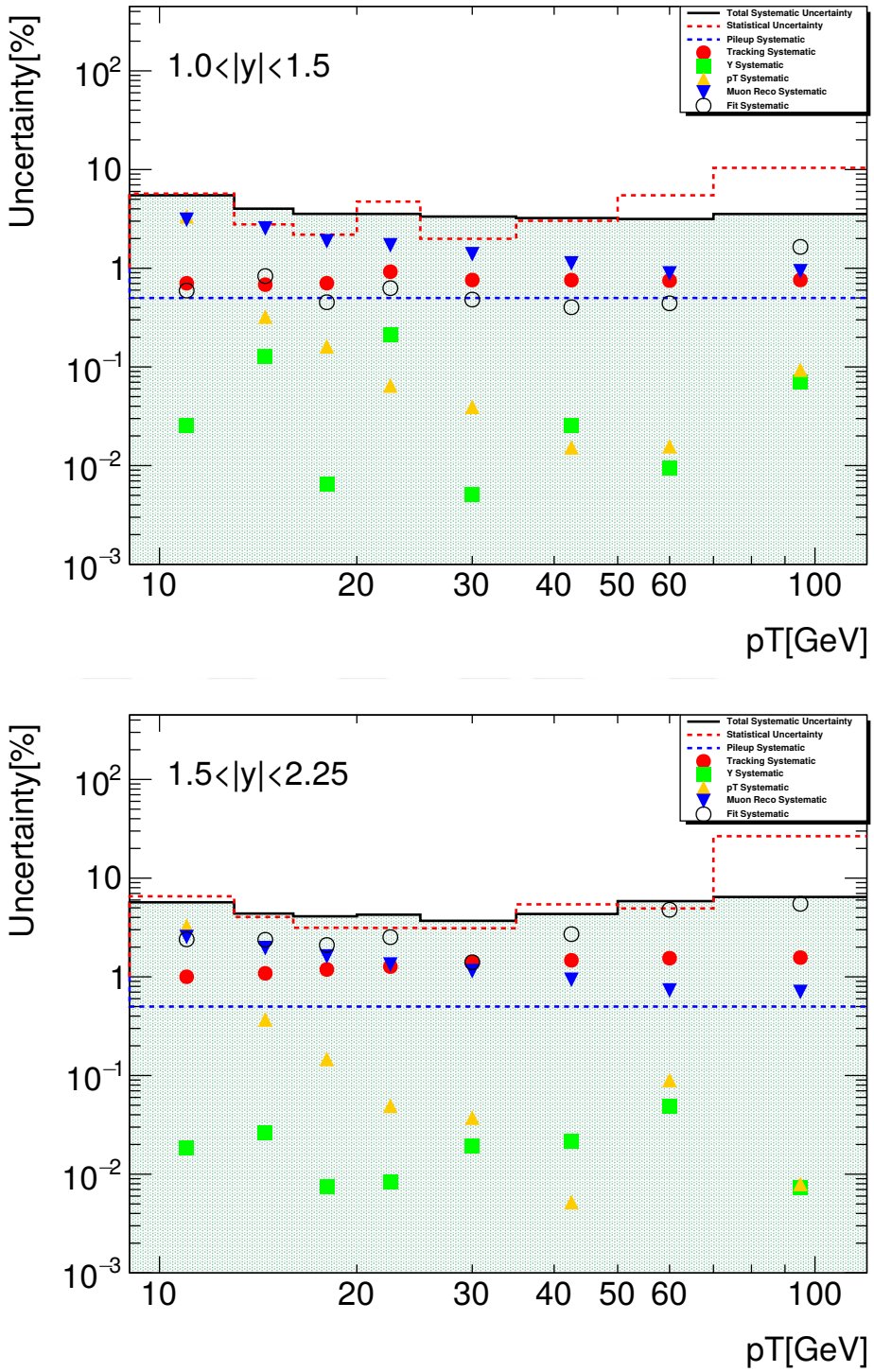

Figure 7.4 Percentage systematic and statistical uncertainties in double differential bins, for the last two y bins.

CHAPTER 8

RESULTS

The cross-section results are provided in the figures and tables below. The Data15 is represented by the black dots in the accompanying images, and the error bar displaying the stat+syst (total) uncertainty is indicated by the black line. The blue error bar on the data shows the statistical uncertainty.

8.1 Cross-section

Figure 8.1 is depicts cross-section in p_{T} and Figure 8.2 is showing the $|y|$ bin. In the $\frac{d\sigma}{dp_{\mathrm{T}}}$ and $\frac{d\sigma}{dy}$ plots the data is compared with FONLL (NNPDF30) and GM-VFNS predictions. Also the $\frac{Theory}{Data}$ ratio is given at the bottom pad of each plot.

The orange box represents the FONLL's upper and lower prediction ranges, while the red line displays the central results. The yellow line is GM-VFNS's central value, with a blue box showing the highest and lowest predictions.

8.1.1 Cross-section in p_{T} Bin

Table 8.1 shows the 13 TeV $B^{\pm}$ p_{T} bin cross-section results plotted in the Figure 8.1. Mean, statistical uncertainty and systematic uncertainty are shown separately.

Table 8.1 Cross-section in p_{T} bin.

p_{T} [GeV]		$B^{\pm}$ [μb/GeV] ($\lvert y\rvert < 2.25$)				
min	max	$\bar{\sigma}_{13\ \mathrm{TeV}}$	$\pm$	δ_{stat}	$\pm$	δ_{syst}
9.00	13.00	2.785 75	$\pm$	0.071 55	$\pm$	0.125 84
13.00	16.00	1.212 92	$\pm$	0.018 43	$\pm$	0.031 83
16.00	20.00	0.579 01	$\pm$	0.006 91	$\pm$	0.013 07
20.00	25.00	0.242 27	$\pm$	0.003 71	$\pm$	0.005 22
25.00	35.00	0.081 27	$\pm$	0.000 95	$\pm$	0.001 48
35.00	50.00	0.017 07	$\pm$	0.000 32	$\pm$	0.000 31
50.00	70.00	0.003 27	$\pm$	0.000 08	$\pm$	0.000 07
70.00	120.00	0.000 40	$\pm$	0.000 03	$\pm$	0.000 01

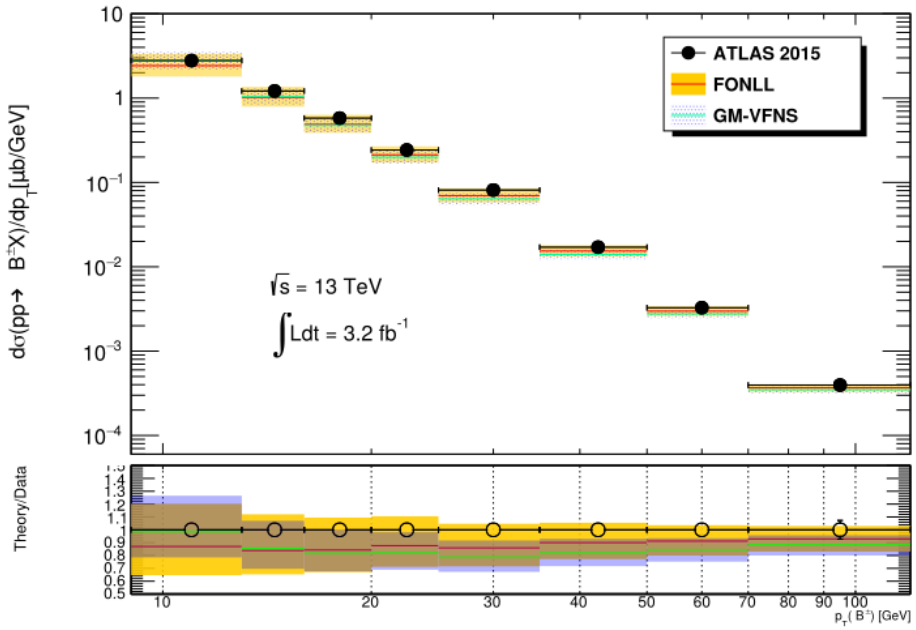

Figure 8.1 $B^{\pm}$ cross-section in p_{T} bin.

8.1.2 Cross-section in y Bin

Table 8.2 contains the 13 TeV $B^{\pm}$ $|y|$ bin cross-section results plotted in the Figure 8.2. Mean, statistical uncertainty and systematic uncertainty are shown separately.

Table 8.2 Cross-section in $|y|$ bin.

$\|y\|$		$B^{\pm}$ [μb](9<p_{T} <120 GeV)				
min	max	$\bar{\sigma}_{13\ \mathrm{TeV}}$	$\pm$	δ_{stat}	$\pm$	δ_{syst}
0.00	0.50	5.127	$\pm$	0.084	$\pm$	0.168
0.50	1.00	4.275	$\pm$	0.081	$\pm$	0.137
1.00	1.50	4.127	$\pm$	0.135	$\pm$	0.143
1.50	2.25	3.956	$\pm$	0.156	$\pm$	0.155

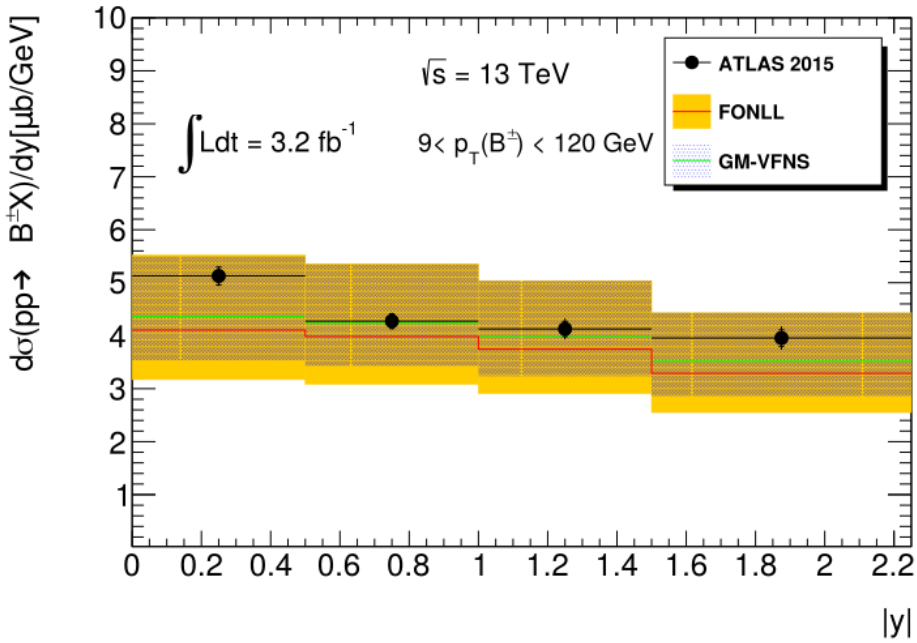

Figure 8.2 $B^{\pm}$ cross-section in $|y|$ bin.

8.1.3 Cross-section in Double Differential Bin

Table 8.3 contains the 13 TeV $B^{\pm}$ double differential bin cross-section results plotted in the Figure 8.3. Mean, statistical uncertainty and systematic uncertainty are shown separately.

Table 8.3 Cross-section in double differential bin.

p_T [GeV]		$B^{\pm}$ [μb/GeV] $(0.0 < \|y\| < 0.5)$					$B^{\pm}$ [μb/GeV] $(0.5 < \|y\| < 1.0)$				
min	max	$\bar{\sigma}_{13\ \mathrm{TeV}}$	$\pm$	δ_{stat}	$\pm$	δ_{syst}	$\bar{\sigma}_{13\ \mathrm{TeV}}$	$\pm$	δ_{stat}	$\pm$	δ_{syst}
9.00	13.00	0.745 07	$\pm$	0.020 35	$\pm$	0.032 03	0.593 56	$\pm$	0.019 44	$\pm$	0.026 43
13.00	16.00	0.315 08	$\pm$	0.005 77	$\pm$	0.008 51	0.274 27	$\pm$	0.006 09	$\pm$	0.006 82
16.00	20.00	0.147 82	$\pm$	0.002 32	$\pm$	0.003 34	0.131 64	$\pm$	0.002 41	$\pm$	0.002 72
20.00	25.00	0.063 07	$\pm$	0.001 08	$\pm$	0.001 33	0.056 48	$\pm$	0.001 23	$\pm$	0.001 04
25.00	35.00	0.020 52	$\pm$	0.000 32	$\pm$	0.000 38	0.018 55	$\pm$	0.000 32	$\pm$	0.000 29
35.00	50.00	0.004 40	$\pm$	0.000 10	$\pm$	0.000 08	0.004 12	$\pm$	0.000 11	$\pm$	0.000 05
50.00	70.00	0.000 90	$\pm$	0.000 04	$\pm$	0.000 01	0.000 84	$\pm$	0.000 05	$\pm$	0.000 01
70.00	120.00	0.000 11	$\pm$	0.000 01	$\pm$	0.000 01	0.000 10	$\pm$	0.000 01	$\pm$	0.000 00

p_T [GeV]		$B^{\pm}$ [μb/GeV] $(1.0 < \|y\| < 1.5)$					$B^{\pm}$ [μb/GeV] $(1.5 < \|y\| < 2.25)$				
min	max	$\bar{\sigma}_{13\ \mathrm{TeV}}$	$\pm$	δ_{stat}	$\pm$	δ_{syst}	$\bar{\sigma}_{13\ \mathrm{TeV}}$	$\pm$	δ_{stat}	$\pm$	δ_{syst}
9.00	13.00	0.577 92	$\pm$	0.032 98	$\pm$	0.027 08	0.579 47	$\pm$	0.037 95	$\pm$	0.028 52
13.00	16.00	0.258 64	$\pm$	0.007 20	$\pm$	0.007 29	0.243 28	$\pm$	0.009 84	$\pm$	0.008 07
16.00	20.00	0.129 73	$\pm$	0.002 84	$\pm$	0.002 75	0.113 21	$\pm$	0.003 56	$\pm$	0.003 33
20.00	25.00	0.053 30	$\pm$	0.002 52	$\pm$	0.001 13	0.046 28	$\pm$	0.001 45	$\pm$	0.001 46
25.00	35.00	0.017 76	$\pm$	0.000 35	$\pm$	0.000 31	0.016 30	$\pm$	0.000 51	$\pm$	0.000 38
35.00	50.00	0.003 82	$\pm$	0.000 12	$\pm$	0.000 06	0.003 16	$\pm$	0.000 17	$\pm$	0.000 10
50.00	70.00	0.000 75	$\pm$	0.000 04	$\pm$	0.000 01	0.000 52	$\pm$	0.000 03	$\pm$	0.000 03
70.00	120.00	0.000 09	$\pm$	0.000 01	$\pm$	0.000 00	0.000 06	$\pm$	0.000 02	$\pm$	0.000 00

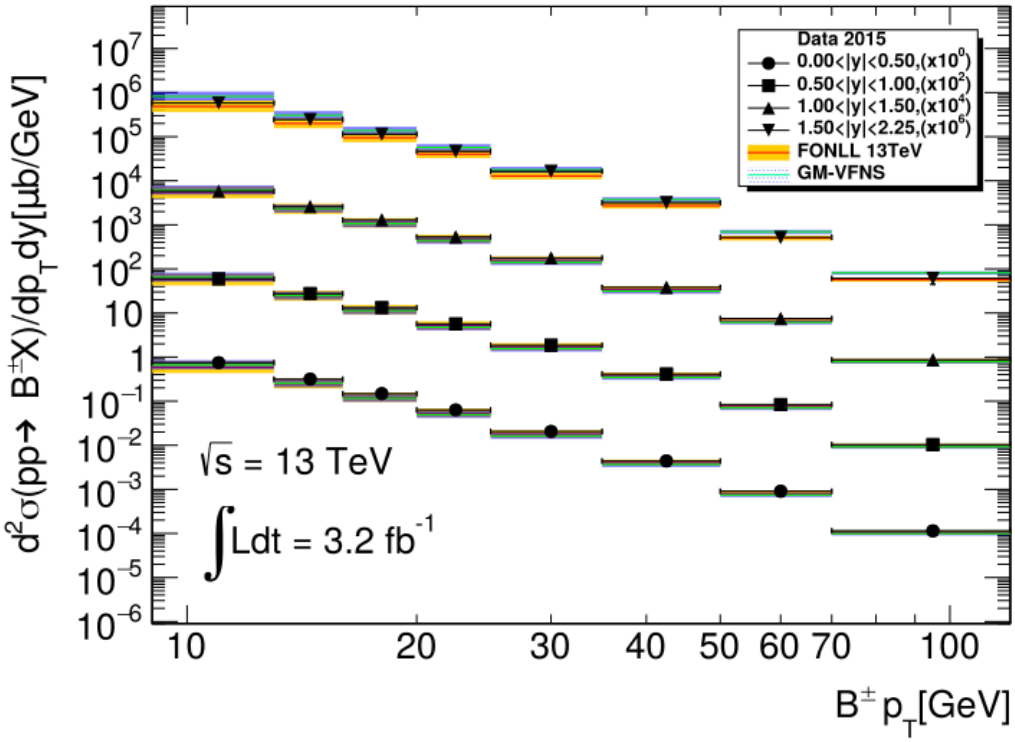

Figure 8.3 $B^{\pm}$ cross-section in double differential bin.

8.2 Cross-section Ratio

13 TeV B^+/B^- cross-section ratio is shown in the Figure 8.4 and Figure 8.5, resulting that the $\sigma_{B^+}/\sigma_{B^-}$ ratio of the Data15 is agreeing with MC15 (TRUTH0). The used Truth0 MC sets are described at the Table 3.2.

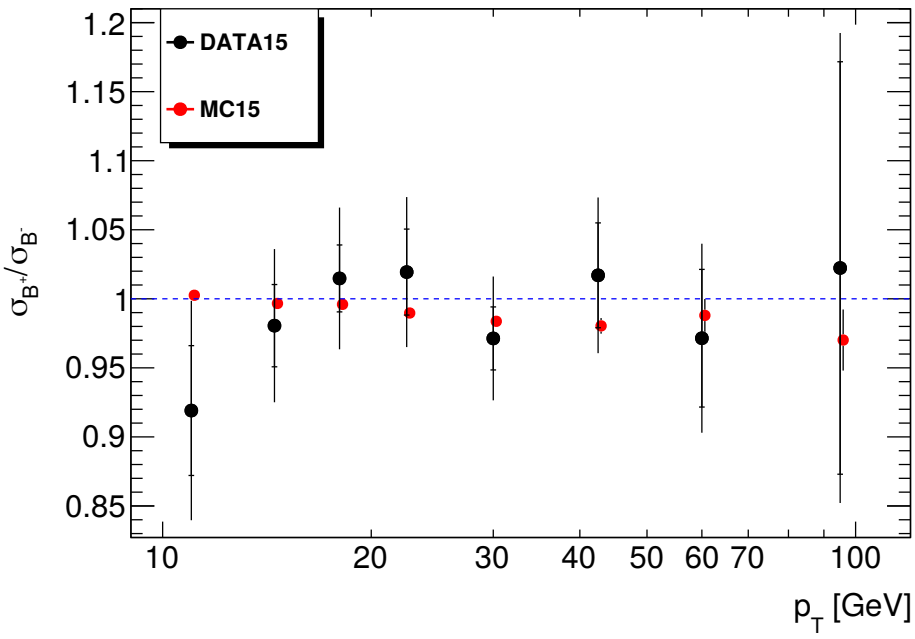

Figure 8.4 B^+ and B^- cross-section ratio shown in p_{T} bin for the DATA15 (Black) and MC15 (Red).

Figure 8.6 shows the 13/7 TeV cross-section ratio, the black dots are showing the data points, FONLL is represented with a blue line and GM-VFNS theory ratios represented with a red box with a red line as central value. The FONLL predictions used are shown in a table in Appendix G, and GM-VFNS are shown in the Appendix H.

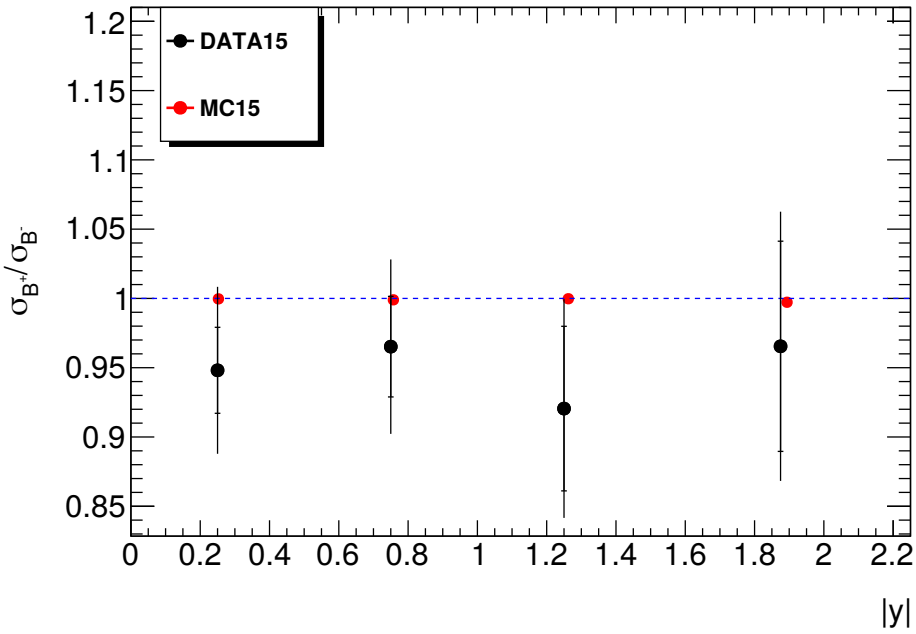

Figure 8.5 B^+ and B^- cross-section ratio shown in $|y|$ bin for the DATA15 (Black) and MC15 (Red).

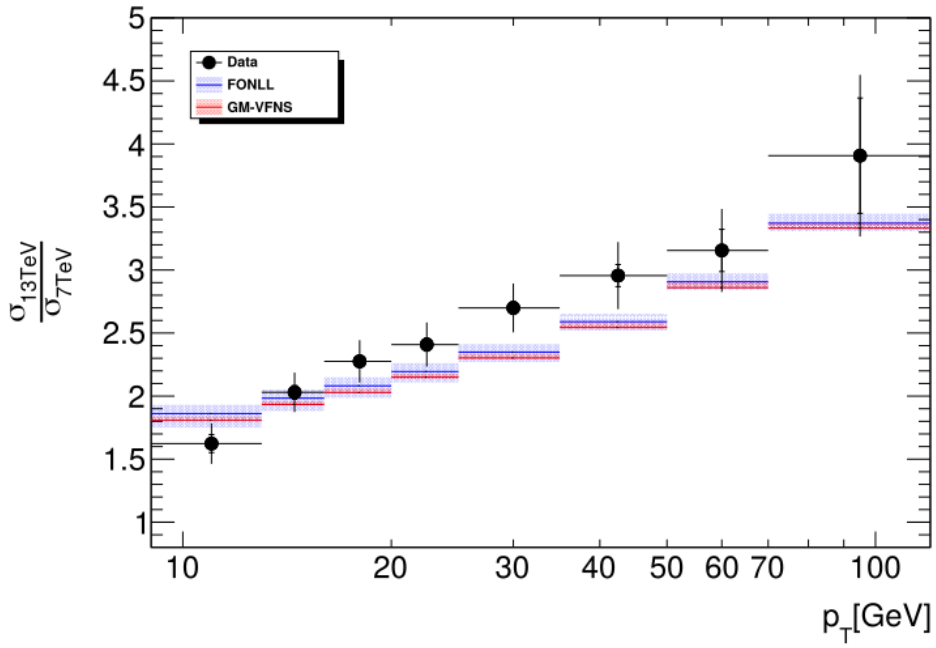

Figure 8.6 $B^{\pm}$ cross-section ratio of 13/7 TeV in p_T bin.

Table 8.4 $\sigma_{13\text{ TeV}}/\sigma_{7\text{ TeV}}$ cross-section ratios in p_{T} bin.

($\lvert y\rvert < 0.25$)		$\sigma_{13\text{ TeV}}/\sigma_{7\text{ TeV}}$								
p_{T} [GeV]		DATA			FONLL			GM-VFNS		
min	max	σ	δ_{stat}	δ_{syst}	Central	Down	Up	Central	Down	Up
9.00	13.00	1.623 227	0.071 500	0.160 890	1.861 394	1.750 500	1.931 217	1.807 758	1.814 330	1.838 262
13.00	16.00	2.029 956	0.054 651	0.156 401	1.983 824	1.881 636	2.052 072	1.933 509	1.928 250	1.959 473
16.00	20.00	2.275 627	0.045 982	0.167 921	2.081 810	1.986 281	2.148 905	2.028 294	2.023 196	2.059 074
20.00	25.00	2.408 713	0.051 385	0.175 218	2.194 772	2.108 490	2.261 473	2.150 339	2.136 389	2.176 788
25.00	35.00	2.699 350	0.051 185	0.193 722	2.349 067	2.269 749	0.412 863	2.302 521	2.291 436	2.335 831
35.00	50.00	2.955 855	0.087 519	0.266 248	2.589 556	2.520 001	2.653 126	2.544 272	2.536 238	2.585 100
50.00	70.00	3.155 300	0.167 479	0.329 372	2.906 884	2.842 456	2.972 678	2.859 985	2.856 380	2.907 533
70.00	120.00	3.906 876	0.457 448	0.641 023	3.370 509	3.309 339	3.446 417	3.332 888	3.325 315	3.375 412

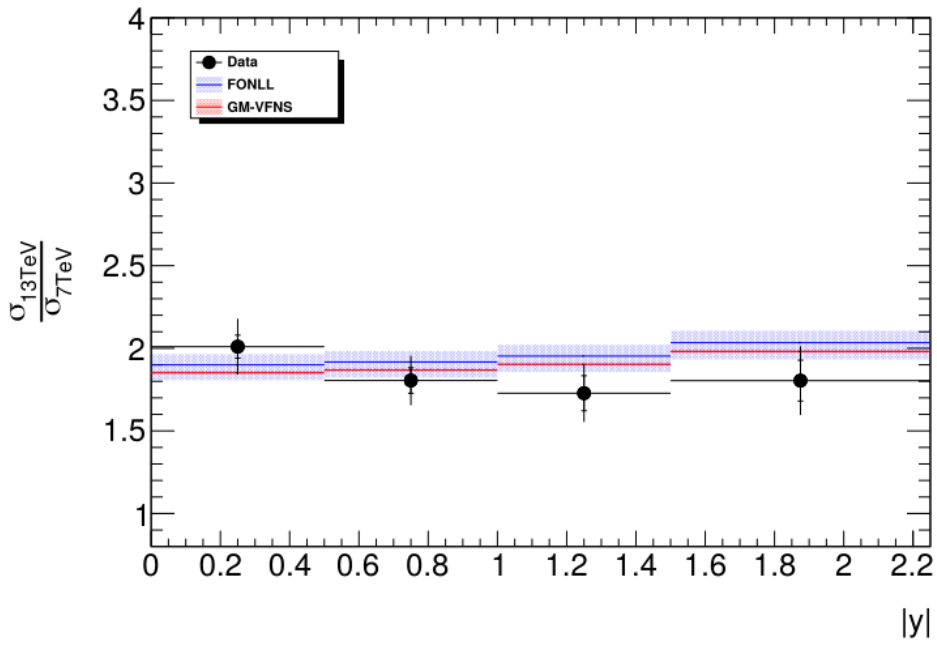

Figure 8.7 $B^{\pm}$ cross-section ratio of 13/7 TeV in $|y|$ bins.

Table 8.5 $\sigma_{13\text{ TeV}}/\sigma_{7\text{ TeV}}$ cross-section ratios in $|y|$ bin.

(9<p_{T} <125 GeV)		$\sigma_{13\text{ TeV}}/\sigma_{7\text{ TeV}}$								
$\lvert y\rvert$		DATA			FONLL			GM-VFNS		
min	max	σ	δ_{stat}	δ_{syst}	Central	Down	Up	Central	Down	Up
0.00	0.50	2.009 803	0.069 720	0.168 569	1.899 585	1.807 179	1.964 968	1.851 520	1.844 207	1.863 501
0.50	1.00	1.805 045	0.077 483	0.149 568	1.917 157	1.822 768	1.983 265	1.867 625	1.860 488	1.879 724
1.00	1.50	1.728 028	0.106 287	0.173 353	1.952 766	1.856 756	2.021 699	1.902 480	1.895 042	1.915 132
1.50	2.25	1.804 204	0.123 488	0.208 367	2.033 636	1.932 025	2.106 385	1.980 637	1.972 345	1.994 338

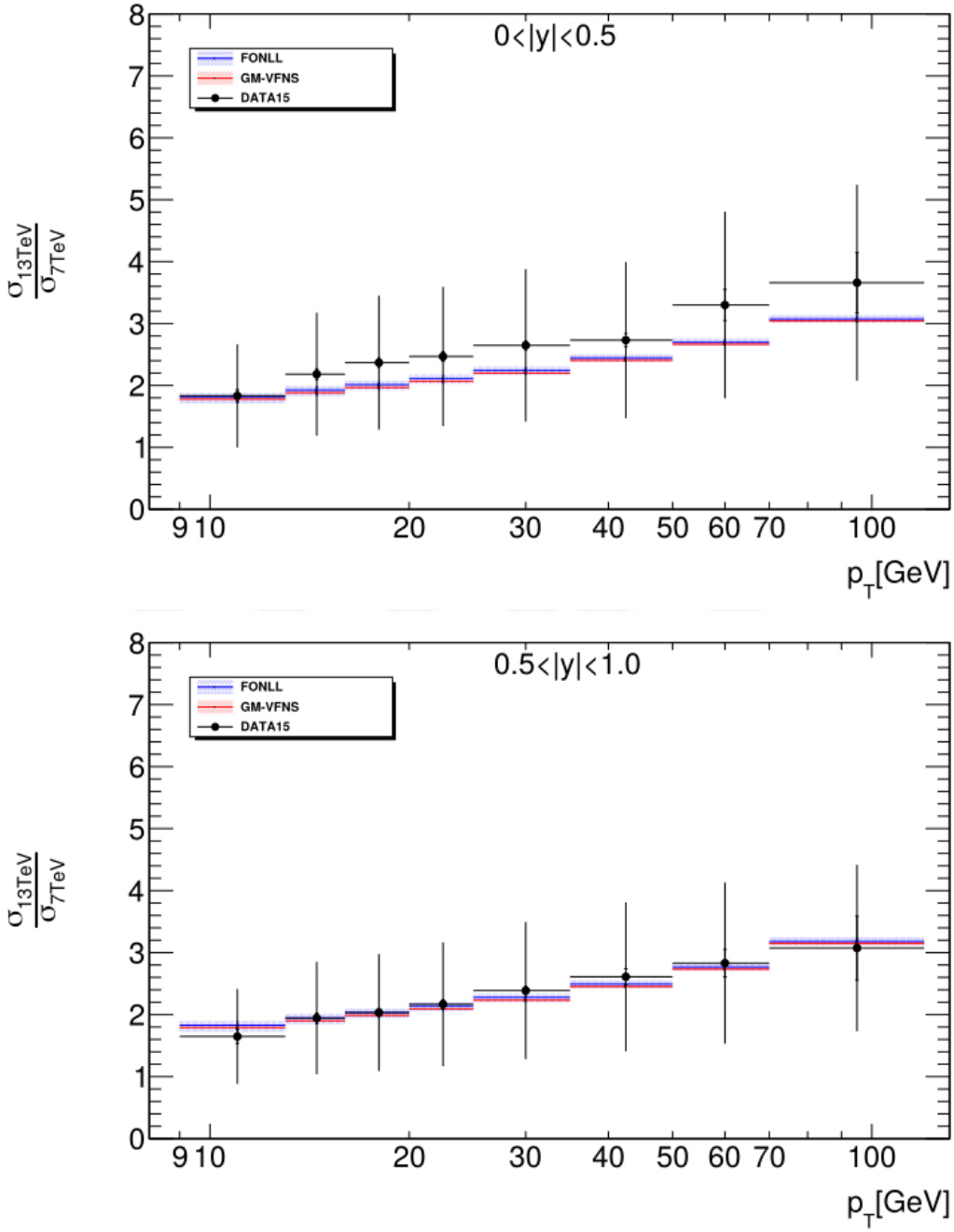

Figure 8.8 $B^{\pm}$ cross-section ratio of 13/7 TeV in first two rapidity bin of double differential bins, each plots shows regarding y bin.

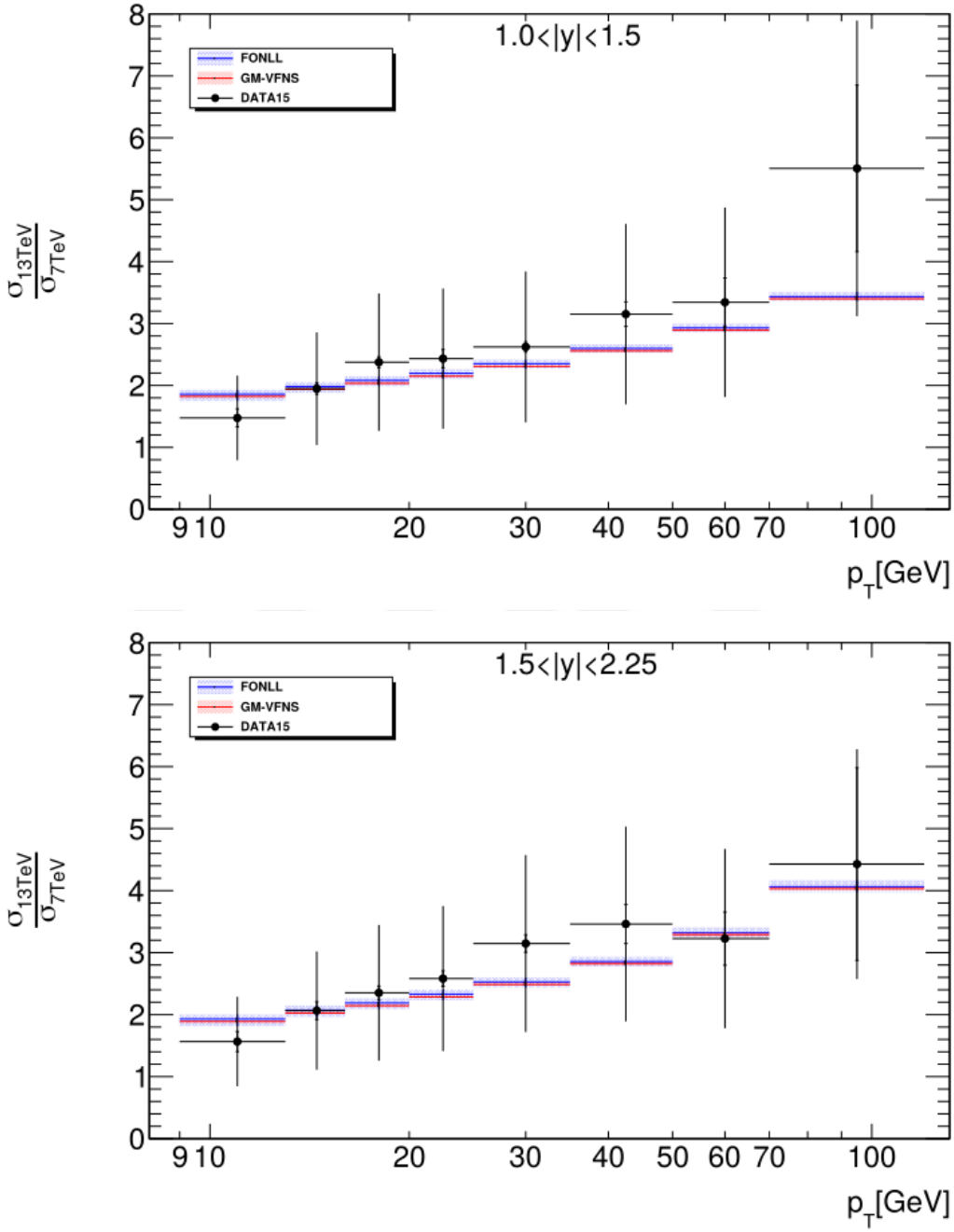

Figure 8.9 $B^{\pm}$ cross-section ratio of 13/7 TeV in last two rapidity bin of double differential bins, each plots shows regarding y bin.

CHAPTER 9

CONCLUSION

The production of B^+ and B^- bottom mesons has been measured in the kinematic region $9 < p_T(B^\pm) < 120$ GeV and $|y(B^\pm)| < 2.25$ with the ATLAS detector in pp collisions at $\sqrt{s} = 13$ TeV at the LHC, using an integrated luminosity of 3.2 fb^{-1}. The differential cross sections $d\sigma/dp_T$ and $d\sigma/d|y|$ and double-differential cross sections $d^2\sigma/dp_T d|y|$ for B^+ and B^- production have been determined.

The ratio of the B^+ and B^- differential cross sections have been found to be equal within experimental uncertainties, in agreement with the Pythia event generator predictions. Averaged $B^\pm$ differential and double-differential cross sections have been compared with the FONLL and GM-VFNS NLO QCD predictions. The predictions describe the data well within large theoretical uncertainties. The average $B^\pm$ mass is studied for the side study and results are found to be consistent with the PDG values as shown in Appendix F.

To drastically reduce the theoretical uncertainties the comparison has been repeated for the ratios of the $B^\pm$ production cross sections in pp collisions at $\sqrt{s} = 13$ TeV and $\sqrt{s} = 7$ TeV. The ratios are reasonably well described by both FONLL and GM-VFNS predictions.

REFERENCES

[1] Thomas Sven Pettersson and P Lefèvre. The Large Hadron Collider: conceptual design. Technical report. 1995. URL: https://cds.cern.ch/record/291782.

[2] ATLAS Collaboration. "The ATLAS Experiment at the CERN Large Hadron Collider". In: JINST 3 (2008), S08003. DOI: 10.1088/1748-0221/3/08/S08003.

[3] ATLAS Collaboration. "Measurement of the differential cross-section of B^+ meson production in pp collisions at $\sqrt{s} = 7$ TeV at ATLAS". In: JHEP 10 (2013), page 042. DOI: 10.1007/JHEP10(2013)042. arXiv: 1307.0126 [hep-ex].

[4] Leonid Gladilin, Zekeriya Uysal, and Marina Aleksandrova. Measurement of the $B^{\pm}$ production cross sections in pp collisions at $\sqrt{s} = 13$ TeV at ATLAS: Supporting document. Technical report. Geneva: CERN, 2022. URL: https://cds.cern.ch/record/2804949.

[5] Lyndon Evans and Philip Bryant. "LHC Machine". In: Journal of Instrumentation (2008). ISSN: 17480221. DOI: 10.1088/1748-0221/3/08/S08001.

[6] The ATLAS Collaboration. "The ATLAS Experiment at the CERN Large Hadron Collider". In: Journal of Instrumentation 3.08 (Aug. 2008), S08003–S08003. DOI: 10.1088/1748-0221/3/08/s08003.

[7] The CMS Collaboration. "The CMS experiment at the CERN LHC". In: Journal of Instrumentation (2008). DOI: 10.1088/1748-0221/3/08/S08004.

[8] The ALICE Collaboration and Aamodt. "The ALICE experiment at the CERN LHC". In: Journal of Instrumentation 3.08 (Aug. 2008). ISSN: 1748-0221. DOI: 10.1088/1748-0221/3/08/S08002.

[9] The LHCb Collaboration. "The LHCb Detector at the LHC". In: Journal of Instrumentation 3.08 (Aug. 2008), S08005–S08005. DOI: 10.1088/1748-0221/3/08/s08005.

[10] Julie Haffner. The CERN accelerator complex. Complexe des accélérateurs du CERN. General Photo. 2013. URL: http://cds.cern.ch/record/1621894.

[11] Oliver S. Bruning et al. "LHC Design Report Vol.1: The LHC Main Ring". In: (2004). URL: https://cds.cern.ch/record/782076.

[12] ATLAS Collaboration. Luminosity determination in pp collisions at $\sqrt{s} = 13$ TeV using the ATLAS detector at the LHC. ATLAS-CONF-2019-021. 2019. URL: https://cds.cern.ch/record/2677054.

[13] ATLAS Collobration. "ATLAS detector and physics performance: Technical Design Report, 1". In: Technical design report. ATLAS (1999). URL: http://cds.cern.ch/record/391176.

[14] A Salzburger. The ATLAS Track Extrapolation Package. Technical report. Geneva: CERN, 2007. URL: http://cds.cern.ch/record/1038100.

[15] G. Aad et al. "Studies of the performance of the ATLAS detector using cosmic-ray muons". In: Eur. Phys. J. C 71 (2011), page 1593. DOI: 10.1140/epjc/s10052-011-1593-6. arXiv: 1011.6665 [physics.ins-det].

[16] ATLAS Collaboration. ATLAS Magnet System: Technical Design Report, 1. ATLAS-TDR-6. 1997. URL: https://cds.cern.ch/record/338080.

[17] M Aleksa et al. "Measurement of the ATLAS solenoid magnetic field". In: Journal of Instrumentation 3.04 (May 2008), P04003. DOI: 10.1088/1748-0221/3/04/P04003.

[18] ATLAS Collaboration. "Alignment of the ATLAS Inner Detector in Run-2". In: Eur. Phys. J. C 80.12 (2020), page 1194. DOI: 10.1140/epjc/s10052-020-08700-6. arXiv: 2007.07624. URL: https://cds.cern.ch/record/2724037.

[19] Malte Backhaus. The upgraded Pixel Detector of the ATLAS Experiment for Run2 at the Large Hadron Collider. Technical report. Geneva: CERN, 2016. DOI: 10.1016/j.nima.2016.05.018. URL: http://cds.cern.ch/record/2110260.

[20] M Capeans et al. ATLAS Insertable B-Layer Technical Design Report. Technical report. 2010. URL: https://cds.cern.ch/record/1291633.

[21] G. Aad et al. "Expected Performance of the ATLAS Experiment - Detector, Trigger and Physics". In: (2009). arXiv: 0901.0512 [hep-ex].

[22] G. Aad et al. "The ATLAS Inner Detector commissioning and calibration". In: Eur. Phys. J. C70 (2010), pages 787–821. DOI: 10.1140/epjc/s10052-010-1366-7. arXiv: 1004.5293 [physics.ins-det].

[23] ATLAS Collaboration. ATLAS Inner Detector: Technical Design Report, 2. ATLAS-TDR-5. 1997. URL: https://cds.cern.ch/record/331064.

[24] E. Abat et al. "The ATLAS Transition Radiation Tracker (TRT) proportional drift tube: Design and performance". In: JINST 3 (2008), P02013. DOI: 10.1088/1748-0221/3/02/P02013.

[25] Bartosz Mindur. ATLAS Transition Radiation Tracker (TRT): Straw tubes for tracking and particle identification at the Large Hadron Collider. Technical report. Geneva: CERN, 2017. DOI: 10.1016/j.nima.2016.04.026. URL: http://cds.cern.ch/record/2139567.

[26] ATLAS Collobration. "Readiness of the ATLAS Liquid Argon Calorimeter for LHC Collisions". In: Eur.Phys.J.C70:723-753,2010 C70 (2010), pages 723–753. DOI: 10.1140/epjc/s10052-010-1354-y. arXiv: 0912.2642 [physics.ins-det].

[27] ATLAS Collaboration. ATLAS Muon Spectrometer Phase-II Upgrade Technical Design Report. Technical report. CERN, Geneva, July 2017.

[28] Georges Aad et al. "Muon reconstruction performance of the ATLAS detector in proton-proton collision data at $\sqrt{s} = 13$ TeV". In: Eur. Phys. J. C76.5 (2016), page 292. DOI: 10.1140/epjc/s10052-016-4120-y. arXiv: 1603.05598 [hep-ex].

[29] Georges Aad et al. "Searches for heavy long-lived charged particles with the ATLAS detector in proton-proton collisions at $\sqrt{s} = 8$ TeV". In: JHEP 01 (2015), page 068. DOI: 10.1007/JHEP01(2015)068. arXiv: 1411.6795 [hep-ex].

[30] G. Aielli et al. "Performance of a large-size RPC equipped with the final ATLAS front end electronics at X5-GIF irradiation facility". In: Nucl. Instrum. Meth. A456 (2000), pages 77–81. DOI: 10.1016/S0168-9002(00)00966-9.

[31] G Chiodini and S Spagnolo. "Off-line time calibration of the ATLAS RPC system". In: Journal of Instrumentation 8.02 (Feb. 2013), T02004–T02004. DOI: 10.1088/1748-0221/8/02/t02004.

[32] F Anulli et al. "The Level-1 Trigger Muon Barrel System of the ATLAS experiment at CERN". In: Journal of Instrumentation 4.04 (Apr. 2009), P04010–P04010. DOI: 10.1088/1748-0221/4/04/p04010.

[33] Georges Aad et al. "Performance of the ATLAS muon trigger in pp collisions at $\sqrt{s} = 8$ TeV". In: Eur. Phys. J. C75 (2015), page 120. DOI: 10.1140/epjc/s10052-015-3325-9. arXiv: 1408.3179 [hep-ex].

[34] G. Aielli et al. “New results on ATLAS RPC’s aging at CERN’s GIF”. In: IEEE Trans. Nucl. Sci. 53 (2006), pages 567–571. DOI: 10.1109/TNS.2006.870181.

[35] Torbjörn Sjöstrand, Stephen Mrenna, and Peter Skands. “A brief introduction to PYTHIA 8.1”. In: Computer Physics Communications (2008). ISSN: 00104655. DOI: 10.1016/j.cpc.2008.01.036. arXiv: 0710.3820.

[36] David J. Lange. “The EvtGen particle decay simulation package”. In: Nuclear Instruments and Methods in Physics Research, Section A: Accelerators, Spectrometers, Detectors and Associated Equipment. 2001. DOI: 10.1016/S0168-9002(01)00089-4.

[37] ATLAS Collaboration. “ATLAS Run1 Pythia8 tunes”. In: Atlas-Phys-Pub-2014-021 November (2014). URL: http://cds.cern.ch/record/1966419.

[38] Jonathan Pumplin et al. “New generation of parton distributions with uncertainties from global QCD analysis”. In: Journal of High Energy Physics (2002). ISSN: 10298479. DOI: 10.1088/1126-6708/2002/07/012.

[39] Agostinelli et al. “GEANT4 - A simulation toolkit”. In: Nuclear Instruments and Methods in Physics Research, Section A: Accelerators, Spectrometers, Detectors and Associated Equipment (2003). ISSN: 01689002. DOI: 10.1016/S0168-9002(03)01368-8.

[40] Matteo Cacciari et al. “Theoretical predictions for charm and bottom production at the LHC”. In: Journal of High Energy Physics (2012). ISSN: 11266708. DOI: 10.1007/JHEP10(2012)137. arXiv: 1205.6344.

[41] Hung Liang Lai et al. “New parton distributions for collider physics”. In: Physical Review D - Particles, Fields, Gravitation and Cosmology (2010). ISSN: 15507998. DOI: 10.1103/PhysRevD.82.074024. arXiv: 1007.2241.

[42] J et al. Beringer. “Review of Particle Physics Particle Data Group”. In: Physical Review D (2012). DOI: 10.1103/PhysRevD.86.010001.

[43] ATLAS Experiment. BPHY5 Twiki Page. URL: https://twiki.cern.ch/twiki/bin/viewauth/AtlasProtected/BPhysWorkingGroupBPHY5 (visited on 04/09/2021).

[44] Rene Brun and Fons Rademakers. “ROOT - An object oriented data analysis framework”. In: Nuclear Instruments and Methods in Physics Research, Section A: Accelerators, Spectrometers, Detectors and Associated Equipment (1997). ISSN: 01689002. DOI: 10.1016/S0168-9002(97)00048-X.

[45] ATLAS Experiment. ATLAS MCPAnalysisGuidelinesMC16. URL: https://twiki.cern.ch/twiki/bin/viewauth/AtlasProtected/MCPAnalysisGuidelinesMC16 (visited on 12/18/2020).

[46] ATLAS Experiment. Tracking CP Recommendations for Early 2018 Analyses. URL: https://twiki.cern.ch/twiki/bin/viewauth/AtlasProtected/TrackingCPRecsEarly2018 (visited on 04/30/2021).

[47] Wouter Verkerke and David P. Kirkby. "The RooFit toolkit for data modeling". In: eConf C0303241 (2003). Edited by L. Lyons and Muge Karagoz, MOLT007. arXiv: physics/0306116.

[48] P.A. Zyla et al. "Review of Particle Physics". In: PTEP 2020.8 (2020), page 083C01. DOI: 10.1093/ptep/ptaa104.

[49] Pekka Sinervo. "Definition and Treatment of Systematic Uncertainties in High Energy Physics and Astrophysics". In: (2003). URL: https://cds.cern.ch/record/931829.

[50] ATLAS Experiment. ExtendedPileupReweighting, Atlas TWiki. URL: https://twiki.cern.ch/twiki/bin/view/AtlasProtected/ExtendedPileupReweighting (visited on 10/01/2021).

[51] ATLAS Experiment. MuonEfficiencyScaleFactorsToolUsage, Atlas TWiki. URL: https://twiki.cern.ch/twiki/bin/view/Atlas/MuonEfficiencyScaleFactorsToolUsage (visited on 12/19/2021).

[52] ATLAS Experiment. GoodRunLists For Analysis Run2. URL: https://twiki.cern.ch/twiki/bin/viewauth/AtlasProtected/GoodRunListsForAnalysisRun2 (visited on 04/30/2021).

[53] ATLAS Experiment. LuminosityPublicResultsRun2, AtlasPublic TWiki. URL: https://twiki.cern.ch/twiki/bin/view/AtlasPublic/LuminosityPublicResultsRun2 (visited on 12/18/2019).

[54] ATLAS Experiment. ATLAS Luminosity Calculator. URL: https://atlas-lumicalc.cern.ch/ (visited on 12/18/2019).

[55] ATLAS Collaboration. "Measurement of Upsilon production in 7 TeV pp collisions at ATLAS". In: (Nov. 2012). DOI: 10.1103/PhysRevD.87.052004. arXiv: 1211.7255.

[56] ATLAS Experiment. ATLAS BeamSpotPublicResults. URL: https://twiki.cern.ch/twiki/bin/view/AtlasPublic/BeamSpotPublicResults (visited on 12/18/2020).

[57] ATLAS Experiment. ATLAS L1 Muon Trigger Public Results. URL: https://twiki.cern.ch/twiki/bin/view/AtlasPublic/L1MuonTriggerPublicResults (visited on 12/18/2019).

[58] Oliver Kortner et al. Design, Construction, and Commissioning of the BME sMDT Chamber for the ATLAS Muon Spectrometer. Technical report. Geneva: CERN, 2017. URL: https://cds.cern.ch/record/2265787.

[59] Luca Pizzimento. Performance of the BIS78 RPC detectors: a new concept of electronics and detector integration for high-rate and fast timing large size RPCs. Technical report. Geneva: CERN, 2020. URL: https://cds.cern.ch/record/2720934.

[60] OPC Foundation. OPC Foundation Unified Architecture. URL: https://opcfoundation.org/about/opc-technologies/opc-ua/ (visited on 01/10/2023).

[61] Esma Anais Mobs. "The CERN accelerator complex. Complexe des accélérateurs du CERN". In: (2016). URL: http://cds.cern.ch/record/2225847.

[62] Technical Design Report for the Phase-II Upgrade of the ATLAS Muon Spectrometer. Technical report. Geneva: CERN, 2017. URL: http://cds.cern.ch/record/2285580.

APPENDIX A

LUMINOSITY CALCULATION

In ATLAS experiment, total luminosity is calculated by means of an xml file called Good Run List. This lists are prepared by the Data Quality and Physics Groups. The details are provided below.

A.1 Good Run Lists

The Good Runs List (GRL) is a collection of cuts (run and luminosity block numbers) that are applied to a dataset in order to remove data that are not suitable for physics analysis. The GRL are selected officially by Atlas Data Quality, taking into account detector conditions. It is important to know the detector status and the reliability of the collected data. All detector parts vital for analysis are expected to be operational. The GRL is typically used to remove data that are affected by detector or data-acquisition problems, or by known sources.

It allows to focus on the data that are most relevant for the physics analysis, and to exclude data that could potentially bias the results. By removing data that are known to be problematic, the GRL helps to ensure that the physics analysis is based on a clean and reliable dataset. In addition to removing problematic data, the GRL can also be used to select specific data subsets for analysis. For example, the GRL can be used to select data taken under specific detector or data-acquisition conditions, or to select data corresponding to specific periods of time. The good runs list are obtained from the official page [52], and the official GRL used in Data2015 analysis is shown in the Table A.1, representing the luminosity of 3219.56 pb^{-1}.

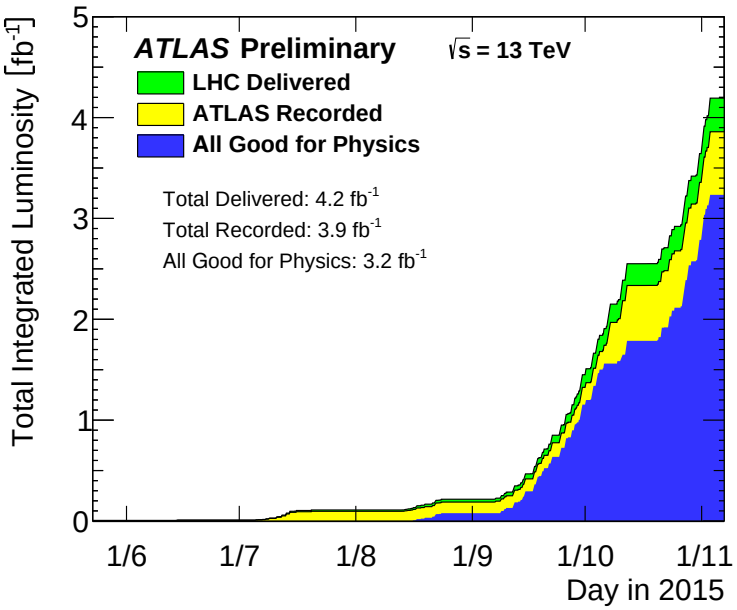

Figure A.1 Total ATLAS integrated luminosity 2015 [53].

A.2 Integrated Luminosity

Total Integrated Luminosity is calculated with using GRL xml file by using the web interface of Atlas Luminosity Calculator [54]. The 2015 Data integrated luminosity for the adviced xml file is shown in the Table A.1.

Table A.1 Run2 corresponding luminosity for 2015 data with given GRL files.

Year	GRL File	Integrated Luminosity (pb^{-1})
2015	physics_25ns_21.0.19	3219.56

The total collected luminosity for Run2 [53] is shown at Figure A.1. In 2015, 3.9 fb^{-1} data is collected and 3.2 fb^{-1} is tagged as good for Physics (see Figure A.1). Integrated luminosity for selected triggers are shown in the Table A.1.

Table A.2 Calculated luminosity values for selected triggers.

Year	Trigger	Int. Luminosity (pb^{-1})	Prescaled
2015	HLT_mu6_mu4_bjpsimumu_noL2	3214.54	No
2015	HLT_2mu4_bjpsimumu_noL2	2569.98	Yes

APPENDIX B

SELECTION OF THE CUTS

This section introduces optimisation of the selected kinematic cuts as well as the procedure for selecting some fine-tuning cuts.

B.1 Cut Optimisation

The subtraction method is used to improve the following cuts:

- $K^+(p_{\mathrm{T}})$,Kaon transverse momentum selection.
- $\theta_K^{'}$ and θ_K^* is studied, where $\theta_K^{'}$ is the angle between muon and kaon momenta in J/ψ rest frame. θ_K^* is the angle between kaon momentum in B^+ rest frame and B^+ line of flight in lab frame.
- L_{xy} is the decay length in xy plane.

Efficiency, purity and the significance of the signal is calculated with below equations :

$$\texttt{Efficiency} = \frac{N_c^S}{N_0^S} \tag{B.1}$$

$$\texttt{Purity} = \frac{N^S}{N^S + N^B} \tag{B.2}$$

$$\texttt{Significance} = \frac{N^S}{\sqrt{N^S + N^B}} \tag{B.3}$$

Where N^S represents the number of signals, N^B denotes the number of background candidates, N_c^S corresponds to the number of signal candidates who passed the cuts, and N_0^S denotes the number of signal candidates before applying the cut.

Kaon p_{T}

The below figure shows the signal significance study of Kaon p_{T} cut. While 1.5 GeV appears to be the best cut, we are using 1.0 GeV to follow the 7 TeV paper [3].

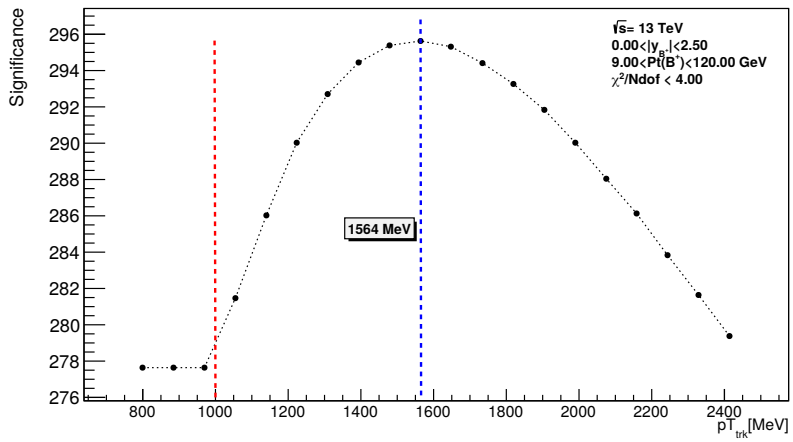

Figure B.1 Track p_{T} study.

B.1.1 Flight Distance L_{xy}

The L_{xy} parameter represents the flight distance of the signal candidate, and the below study depicts the change in significance with respect to a specific cut. $L_{xy} > 0.1$ mm is chosen to cover the majority of the signal while efficiently rejecting background candidates.

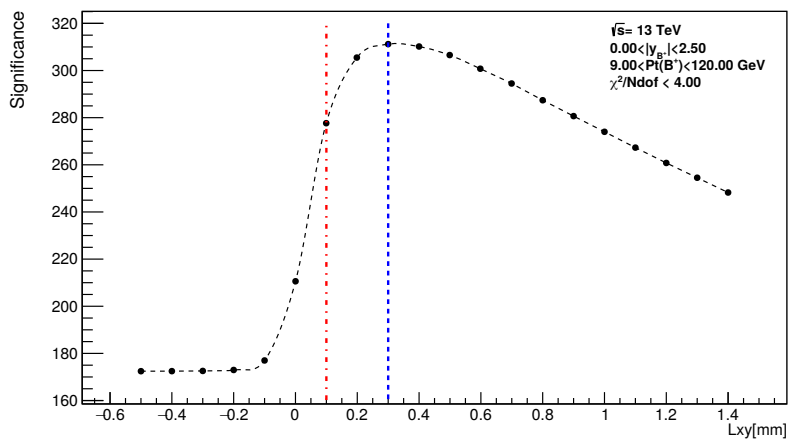

Figure B.2 Lxy significance distribution.

B.1.2 Cos(θ'_K)

Below figures are showing the cosine of the (θ'_K) angle between muon and kaon momenta in J/ψ rest frame. Efficiency, purity and significance is calculated and studied. No significant improvement observed, thus this cut is not used.

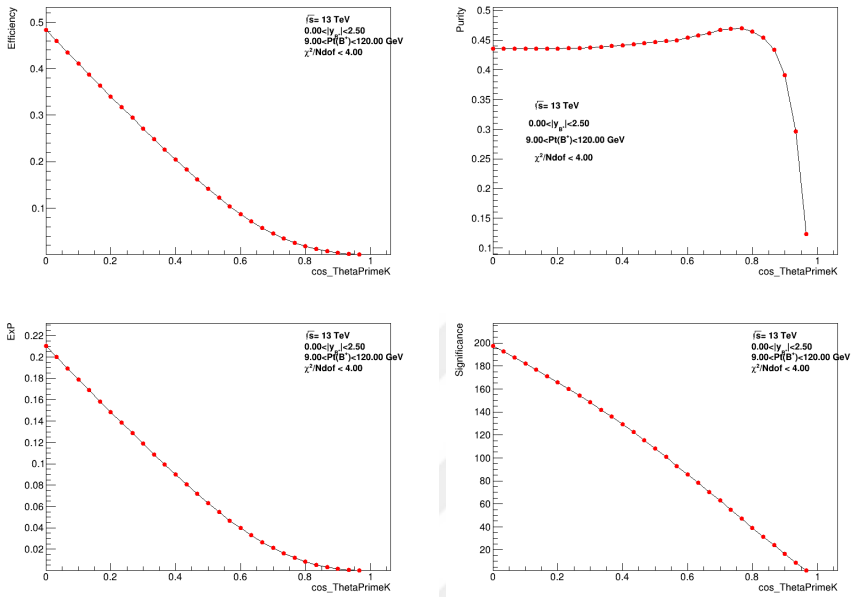

Figure B.3 Efficiency, purity, EP and significance plots.

B.1.3 Cos(θ^*_K)

Figure shows cosine of the (θ^*_K) angle between kaon momentum in B^+ rest frame and B^+ line of flight in lab frame. Efficiency, purity and significance is calculated and studied. No significant improvement observed thus this cut is not used in the selection cuts.

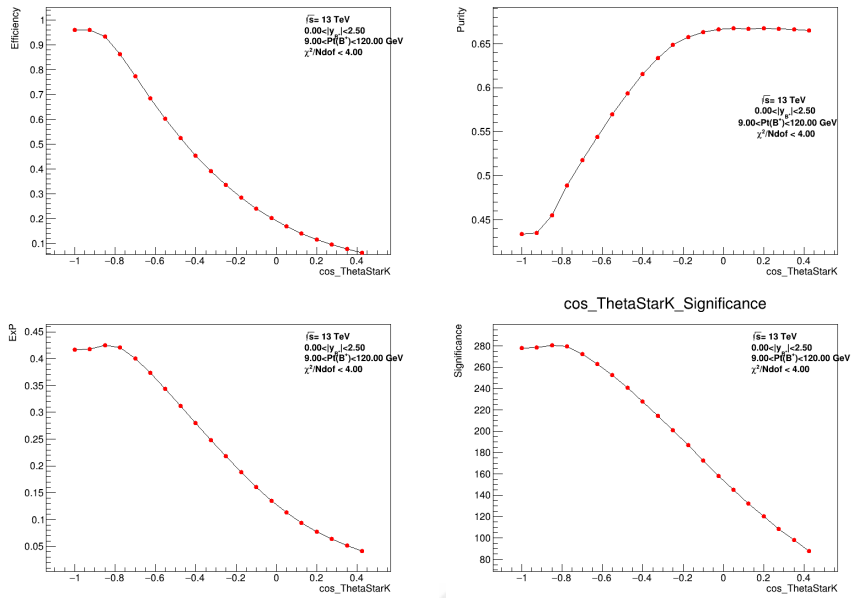

Figure B.4 Efficiency, purity, EP and significance plots.

B.2 Selection of the Cuts

In previous section (Appendix B), some kinematic cuts are optimised with sideband subtraction method, in this section we are investigating other remaining cuts and recommendations that are studied and used in the analysis to fine tune the signal. Those are muon MCP recommendations for R2 data collection period, R_{xy} radial distribution of the B^+ candidates, z_0 and a_{0xy} significance distributions, and trigger matching. Every event has more than one B^+ candidate. Our event structure is one candidate per event in both MC and Data. The event selection algorithm is to apply all analysis cuts and recommendations, collect selected B^+ candidates, and among these, select the best (lowest) $\chi^2/ndof$ candidate.

B.3 Primary Vertex Selection

Before starting to analyze the impact parameters of the tracks and some Recommendations, first we need to decide which primary vertex type will be used. We use 3 type of primary vertex in B physics analysis, which are :

- **PV_MAX_SUM_PT2 :** Vertex with the largest sum p_{T}^2 (the default one)
- **PV_MIN_A0 :** Collision vertex closest in 3D to the particle's trajectory, i.e. the vertex with the smallest 3D impact parameter a_0 .

- **PV_MIN_Z0 :** Collision vertex closest in $\Delta z_0 = pv_z - z_0$, where z_0 is the z coordinate of the intersection of the particle's trajectory with the beam axis in the $z - (xy)$ plane.

PV_MIN_A0 vertex is decided to use in our analysis.

B.4 MCP Recommendations for Muon Selection

To generate the J/ψ meson candidates, tight muons are selected as a working point, to achieve that MCP recommendations[1] for the Run2 analysis are used as the recipe [45].

MuonSelectorTools, a tool supplied by the MCP group for selecting high-quality muons, is used for this purpose. The tool chooses muons depending on several variables, including η cut identification quality (loose, medium, tight, High Pt) and ID track requirements. The definition of the tight working point utilised in the analysis is given in Section B.4.1.

B.4.1 Tight Selection

MCP recommendations describe loose, medium, tight, and high working points. Tight muons are included in medium muons because these working points are inclusive. The tight working point is defined and implemented in our analysis, which features the following muon candidate selection mechanism:

- number of precision layers > 1
- combined $\chi^2/ndf < 8$
- η, p_{T} dependent cuts on $\frac{q}{p}$ significance

ID track requirement:

- $nPIX + nPIX_{dead} > 0$
- $nSCT + nSCT_{dead} > 4$
- $nPIX_{hole} + nSCT_{hole} < 3$
- Succesful TRT hits :

[1] MCP and BPhysics group proposed that analyses use this centrally provided selection tool in order to enable methods to change the muon selection in case of difficulties or enhancements.

* $0.1 < |\eta| < 1.9$
* $nTRT_{hits} + nTRT_{outliers} > 5$
* $nTRT_{outliers} < 0.9n$

B.5 R_{xy} Selection

Because B^+ daughter tracks are required to have some hits in the inner detector parts, B^+ candidates must decay before the ID detector component, so the R_{xy} distribution must be carefully studied. Equation B.4 calculates R_{xy} of the B^+ vertex w.r.t. (0.,0.) w/o using of PV.

$$R_{xy} = \sqrt{x^2 + y^2} \tag{B.4}$$

where x and y are the x and y coordinates of the B^+ vertex respectively. To visualize

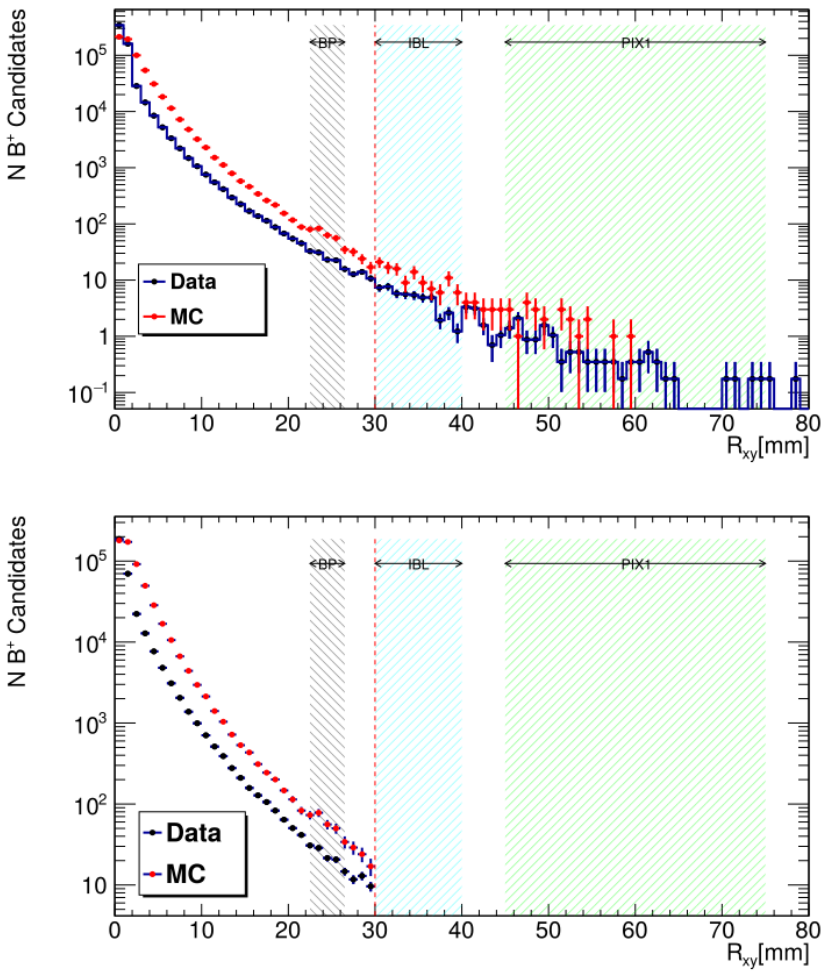

Figure B.5 Data (Red) vs MC (Blue) R_{xy} distribution, detector parts BP (Beam pipe), IBL (Inner B Layer) and PIX (Pixel) are also shown.

the situation, the radial distribution of the number of B^+ candidates and the related detector parts are shown on the Figure B.5. Because we need the muon and kaon track hits inside the ID parts, it is reasonable to choose the B^+ candidates created before IBL ($R_{xy} < 30$ mm), which is shown as a red dotted line.

B.6 The $S(z_0)$ and $S(a_{0xy})$ Selections

The z_0 and a_{0xy} parameters are investigated, and the effect of the cut is found to be primarily on the background. Equation B.5 defines the significance of the z_0, and Equation B.6 defines the significance of the a_{0xy}. These cuts are studied in detail, their effects on signal and background regions are carefully inspected, and in conclusion, the cuts are decided to be used in the analysis.

$$S(z_0) = \frac{z_0}{\sigma_{z_0}} \tag{B.5}$$

Here, $S(z_0)$ is the significance of z_0, numerator is z_0 impact parameter and enumerator σ_{z_0} is the error in z_0 impact parameter. The significance is defined as the ratio of the impact parameter with its error. Figure B.6 shows the z_0 significance distribution of

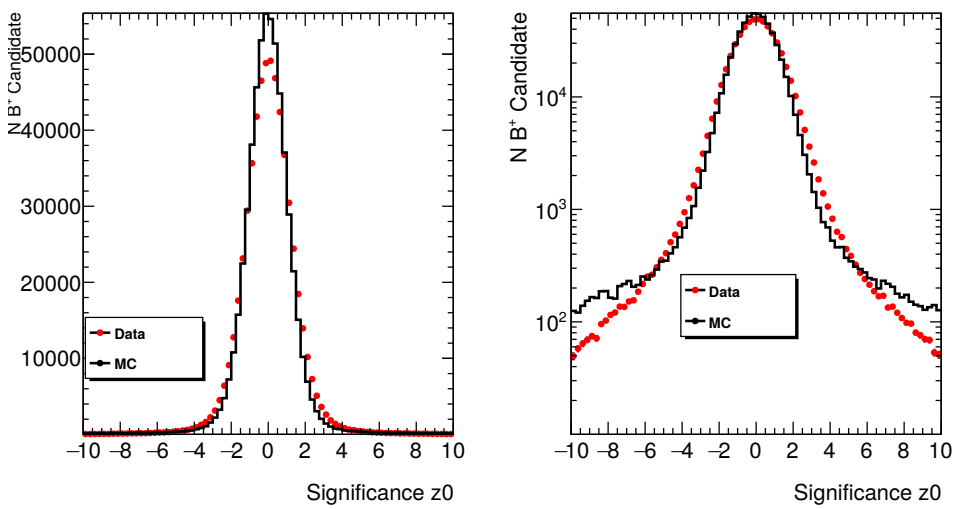

Figure B.6 Data15 (Red) vs MC16a (Blue) Significance z_0. Left figure shows the normal scale, right figure shows the logarithmic scale.

Data15 and MC16a, we select the candidates between $S(z_0) < 5.0$ which contains most of the signal candidates.

$$S(a_{0xy}) = \frac{a_{0xy}}{\sigma_{a_{0xy}}} \tag{B.6}$$

Here, Equation B.6 shows the significance of 3D impact parameter in xy plane.

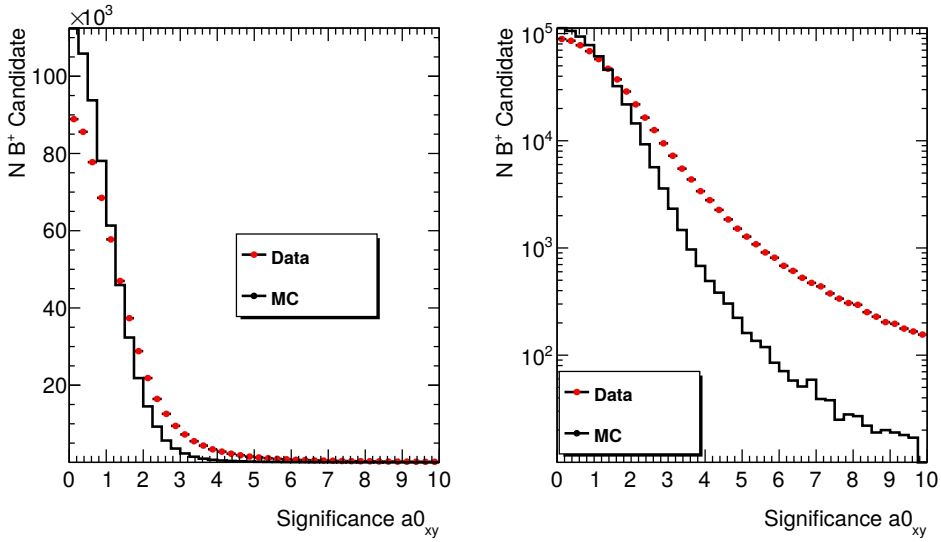

Figure B.7 Data(Red) vs MC(Blue) significance a_{0xy}, left normal scale, right logarithmic scale.

B.7 Trigger Matching

In our analysis it is needed to match the reconstructed offline muon object with the trigger chain objects. Then matched muons can be used to reconstruct the candidates. The base selection is done on ΔR requirement defined in Equation B.7, which is preferred to be below 0.01 for our analysis.

$$\Delta R(\mu_{off}, \mu_{Trig}) = \sqrt{(\Delta\eta)^2 + (\Delta\phi)^2} \tag{B.7}$$

Where μ_{off} is offline muon object and μ_{Trig} is the trigger chain object. For di-muon trigger match, each muon object must satisfy the condition.

APPENDIX C

TRIGGER EFFICIENCY

C.1 Di-muon Trigger Efficiency

The di-muon trigger efficiency refers to the efficiency with which di-muon events (events containing two muons) are selected by the trigger system. The trigger system is responsible for selecting events of interest for further analysis, based on a set of predetermined criteria, in our case some quality cuts and most importantly the p_{T} properties. We are interesting the muon legs with p_{T} greater and equal 4 or 6 GeV and its combinations. The efficiency of the di-muon trigger to select events that have passed the offline selection criteria, ϵ_{trig}, can be factorized into three terms [55]:

$$\epsilon_{\text{trig}} = \epsilon_{\text{RoI}}(p^{\mu}_{\text{T1}}, q_1 \cdot \eta^{\mu}_1) \times \epsilon_{\text{RoI}}(p^{\mu}_{\text{T2}}, q_2 \cdot \eta^{\mu}_2) \times c_{\mu\mu}(\Delta R, |y^{\mu\mu}|) \tag{C.1}$$

where ϵ_{RoI} is the efficiency of the trigger system to find an RoI for a single muon with transverse momentum, p^{μ}_{T}, and charge-signed pseudorapidity, $q \cdot |\eta^{\mu}|$, and $c_{\mu\mu}$ is a correction for effects related to the dimuon elements of the trigger. The dimuon correction, $c_{\mu\mu}$, consists of two components:

$$c_{\mu\mu}(\Delta R, |y^{\mu\mu}|) = c_a(|y^{\mu\mu}|) \times c_{\Delta R}(\Delta R, |\eta^{\mu\mu}|) \tag{C.2}$$

The asymptotic correction, c_a, accounts for the effect of the efficiency losses due to dimuon vertex fit and opposite charge requirements at large dimuon angular separation. The ΔR correction, $c_{\Delta R}$, includes the efficiency losses in the dimuon trigger if two muons are close enough together, so that only a single RoI is built by L1 trigger. The correction $c_{\Delta R}$ accounts for dependence of the dimuon trigger efficiency on the distance between two muon RoIs, which may overlap thus preventing the L1 trigger from resolving them apart. The correction is derived as a function of ΔR in three regions of dimuon pseudorapidity: barrel ($|\eta^{\mu\mu}| \leq 1.0$), overlap ($1.0 < |\eta^{\mu\mu}| \leq 1.2$), and endcap ($1.2 < |\eta^{\mu\mu}| \leq 2.3$). Muons with $p_{\mathrm{T}} > 8$ GeV are selected. The following fraction is calculated:

$$\rho_{\Delta R}(\Delta R, |\eta^{\mu\mu}|) = \frac{N_{\Delta R}(\texttt{EF_muX} \cdot \texttt{HLT_2mu4_bJpsimumu})}{N_{\Delta R}(\texttt{EF_muX})} \tag{C.3}$$

where $N_{\Delta R}$(EF_muX) is the number of J/ψ which fire at least one of single muon triggers listed below:

- `HLT_mu4_bJpsi_Trkloose`
- `HLT_mu6_bJpsi_Trkloose`
- `HLT_mu10_bJpsi_Trkloose`
- `HLT_mu18_bJpsi_Trkloose`

The numerator $N_{\Delta R}$(`EF_muX`$\cdot$`HLT_2mu4_bJpsimumu`) denotes the number of J/ψ which fire both single and dimuon triggers.

APPENDIX D

MC REWEIGHTING

The following sections study the majority of the variables that influence data matching. While some of them are only connected to detector conditions and may only be applied at the reconstructed level, others are also relevant to the generated level, allowing corrections to be made without altering the physics and kinematics at either level. The factors that we are examining can be summarized as follows:

- Beam Tilt
- Trigger Efficiency
- Refitted Primary Vertex Positions
- Number of Primary Vertices
- Scaling in p_{T} and y bins.

D.1 Beam Tilt

Beam tilt is calculated from the MC16a and Data15 using the primary vertex position information. The x, y, and xy planes are compared with the z plane. The points on the plots show the mean value of the x, y, or xy points corresponding to the z point.

D.1.1 Tilt in xy-z Plane

Beam profile in xy vs z plane for Data15 and MC16a were shown in Figure D.1, where $xy = \sqrt{x^2 + y^2}$. In each plot y axis shows the mean value of the xy in respective z coordinate, while the x axis shows the z coordinate of the vertex. Tilt angle is calculated as:

- Data15 : 0.03173 mrad
- MC16a :0.0002577 mrad.

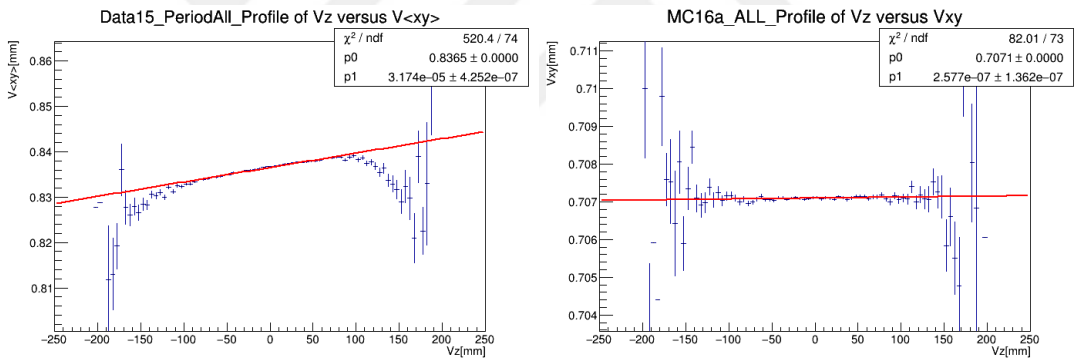

Figure D.1 Data(Left), and MC(Right) V_z vs. $V_{<xy>}$profile.

D.1.2 Tilt in x-z Plane

Figure D.2 shows the beam profile in the x vs z plane for Data15 and MC16a.The y axis in the figure represents the mean value of the x vertex point ($V_{<x>}$) in the respective z coordinate, while the x axis shows the vertex point's z value. The tilt angle is calculated as:

- Data15 : 0.00407 mrad
- MC16a :-0.000125 mrad.

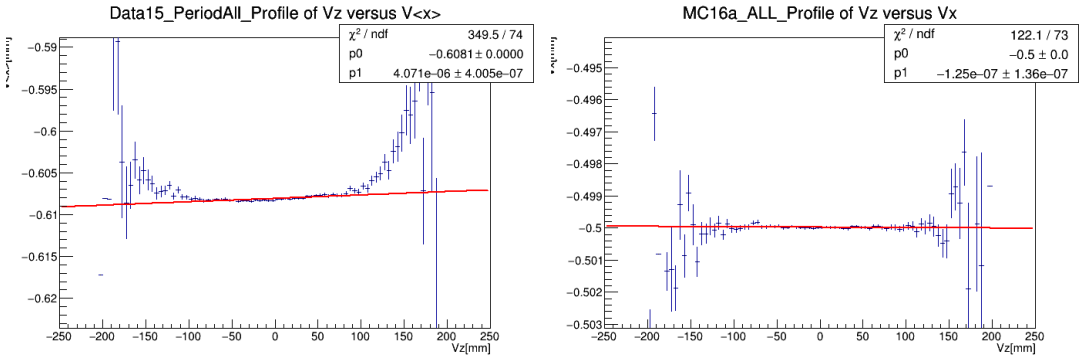

Figure D.2 Data (Left), and MC (Right) V_z vs. $V_{<x>}$ profile.

D.1.3 Tilt in y-z Plane

Beam profile in the x vs z plane for Data15 and MC16a were shown in Figure D.3. The y axis shows the mean value of the y vertex point ($V_{<y>}$) in respective z coordinate, and the x axis shows the z value of the vertex point. The tilt angle is calculated as:

- Data15 : -0.04789 mrad
- MC16a :-0.0005682 mrad.

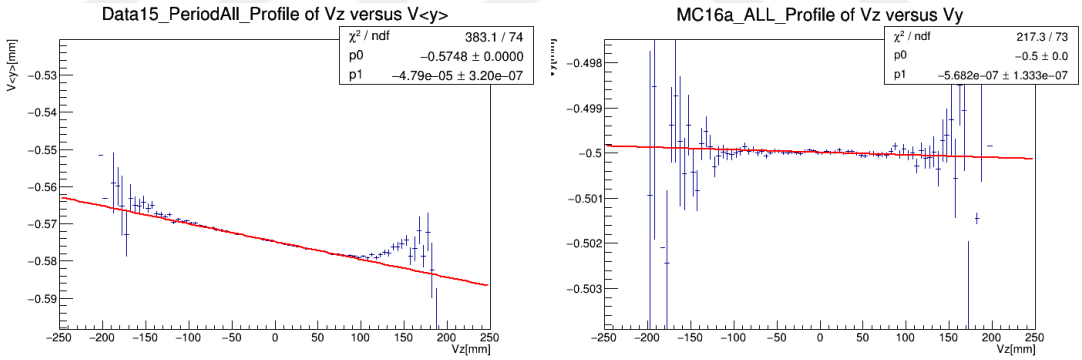

Figure D.3 Data (Left), and MC (Right) V_z vs. $V_{<y>}$ profile.

D.1.4 Tilt Conclusion

In Figure D.4 left plot shows the beam tilt per period, including all periods and MC, and right plot shows the public result [56] of beamspot tilt in the x-z plane in miliradian. In Figure D.5, the left plot shows the beam tilt for DATA15 (per period and all period), MC16a, and the right plot shows the public result of beam spot [56] tilt in the y-z plane. The refitted PV_x and PV_y distribution for MC16a does not describe the Data15 well. There is no straightforward procedure for correcting discrepancies between the DATA15

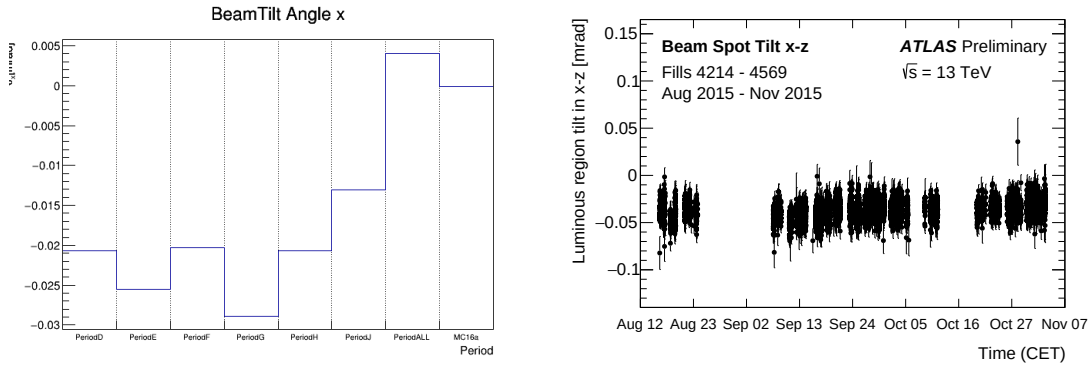

Figure D.4 x-z profile for Data and MC tilt (Left) and beamspot tilt public result (Right).

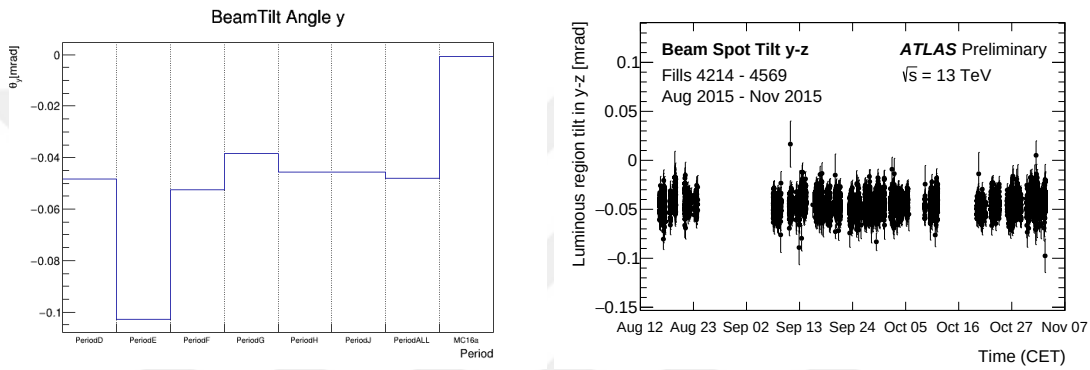

Figure D.5 y-z profile for Data and MC tilt (Left) and beamspot tilt public result (Right).

and MC16a PV_x and PV_y distributions. The tilt in MC is very small, and nearly zero. The tilt in the DATA is clearly seen, although it is very small. The relative momenta biases due to the beam tilt should be within 5×10^{-5} GeV $= 0.05$ MeV and thus be neglected.

In conclusion, expected values are small and the effects of the disagreements will be estimated and added into systematic. The discrepancy between the DATA and MC PV_z distributions is corrected using reweighting, which is described in Section D.2. The procedure is straightforward, and the expected effects are small.

D.1.5 Trigger Scale Factors

The procedures required for the trigger efficiency corrections are calculated in Appendix C.1. We should choose how to properly combine the two triggers during the analysis process. Our strategy is to choose one trigger per event, with the below recipe shown in Figure D.6. For the base, each muon should have at least 4 GeV transverse momentum.

If both muon p_T are below 6 GeV, then HLT_2mu4_bjpsimumu_noL2 trigger is selected. If any muon p_T exceed 6 GeV then trigger should be HLT_mu6_mu4_bjpsimumu_noL2. After selecting the trigger, HLT muons must match with the reconstructed muons within

4 GeV	< pT(mu) <	6 GeV
Base Cut	HLT_2mu4	HLT_mu6mu4

Figure D.6 Selection range for triggers.

$\Delta R < 0.01$. Where $\Delta R = \sqrt{(\Delta\eta)^2 + (\Delta\phi)^2}$. Then the efficiency for the di muon trigger HLT_muX_muY_bDimu where (Y>X) should be calculated from the Equation C.1. The trigger scale factor for both triggers is calculated with the below formula:

$$\mathcal{R}_{sf} = \frac{\epsilon_{Data15}}{\epsilon_{MC16a}} \tag{D.1}$$

Where efficiency for HLT_2mu4_bjpsimumu_noL2 is calculated with :

$$\epsilon_{HLT_2mu4_bDimu} = (\epsilon^{\mu_1}_{HLT_mu4} \cdot \epsilon^{\mu_2}_{HLT_mu4}) \cdot c_{\mu\mu}(\Delta R_{\mu\mu}, |y^{\mu\mu}|, \tau_{\mu\mu}) \tag{D.2}$$

and efficiency for HLT_mu6_mu4_bjpsimumu_noL2 is calculated with :

$$\begin{aligned}\epsilon_{HLT_mu6_mu4_bDimu} = (&\epsilon^{\mu_1}_{HLT_mu6} \cdot \epsilon^{\mu_2}_{HLT_mu4} + \epsilon^{\mu_1}_{HLT_mu4} \cdot \epsilon^{\mu_2}_{HLT_mu6} \\ &- \epsilon^{\mu_1}_{HLT_mu4} \cdot \epsilon^{\mu_2}_{HLT_mu4}) \cdot c_{\mu\mu}(\Delta R_{\mu\mu}, |y^{\mu\mu}|, \tau_{\mu\mu})\end{aligned} \tag{D.3}$$

The ratios of the efficiencies between Data and MC are the scale factors of these triggers. By applying these definitions, we get:

$$\mathcal{R}_{sf}(HLT_2mu4_bDimu) = \frac{\epsilon_{HLT_2mu4_bDimu}(Data15)}{\epsilon_{HLT_2mu4_bDimu}(MC16a)} \tag{D.4}$$

$$\mathcal{R}_{sf}(HLT_mu6_2mu4_bDimu) = \frac{\epsilon_{HLT_mu6_mu4_bDimu}(Data15)}{\epsilon_{HLT_mu6_mu4_bDimu}(MC16a)} \tag{D.5}$$

All calculations are performed per event and contribute to the overall weight of the event described in Section 5.

D.2 Refitted Primary Vertex

D.2.1 Overview

The refitted PV x, y, and z distributions are investigated. This provides a detailed picture of the characteristics of the beam and its interaction point. The primary vertex

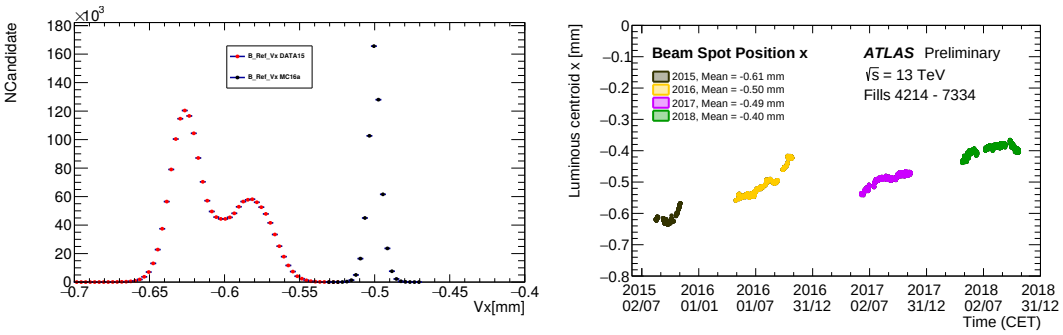

Figure D.7 (Left) Data15 (red) and MC16a (blue) refitted primary vertex x position profile plot. (Right) Public beam spot position x plot.

positions in Data15 (red) and MC16 (black) are plotted in the graphs below (left plots in Figure D.7, D.8 and D.9). Public beam spot positions [56] are also plotted (right plots) for informational purposes. Figure D.7 shows that $< x >_{MC16a} \approx -0.5$, and it agrees with 2016 public beam spot results, while not with public 2015 result. Figure D.8 shows

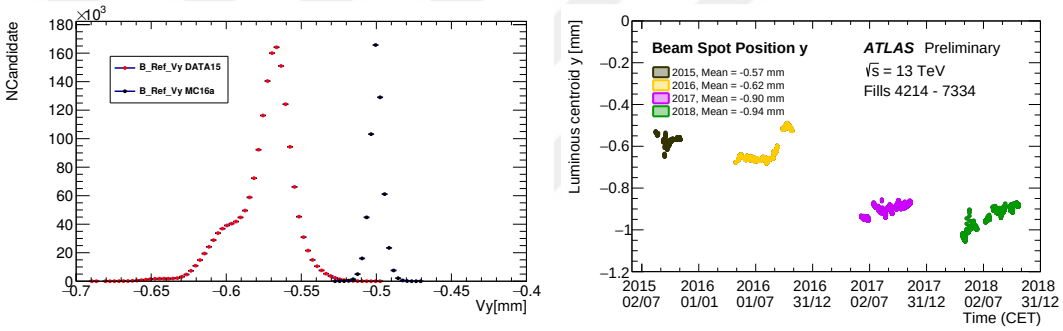

Figure D.8 (Left)Data15 (red) and MC16a (blue)refitted primary vertex y position profile. (Right) Public beam spot position plot y.

that $< y >_{MC16a} \approx -0.5$, and it is in disagreement with the public result and Data15. The Data15 (red) and MC16a (blue) numbers of B^+ candidates are displayed in the

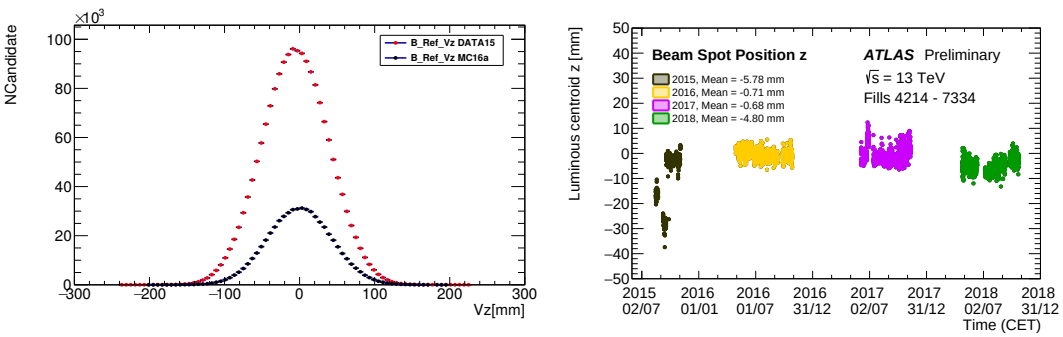

Figure D.9 (Left)Data15 (red) and MC16a (blue) refitted primary vertex z position profile.(Right) Public beam spot position plot z

Figure D.9 together with a refitted $PV_z[mm]$ point on both x and y axes. The lower

pad displays its ratio without any selection and correction. It can be concluded that z position can be corrected with basic procedure, which will be described in the following section (Appendix D.2.2).

D.2.2 Pv_z Reweighting

Primary vertex z position reweighting is applied in order to correct our MC16a with Data15. The procedure is to plot Data15 and MC16a numbers of B^+ candidates in relation with V_z [mm]. The weight function and parameters are then obtained by fitting a first-order polynomial function to the ratio of Data15/MC16a. This function is defined in Equation D.6.

$$f(x) = a_0 + a_1 \cdot x \tag{D.6}$$

Figure D.10 shows the Data15 (red) and MC16a (black) refitted PV$_z$ point and its ratio

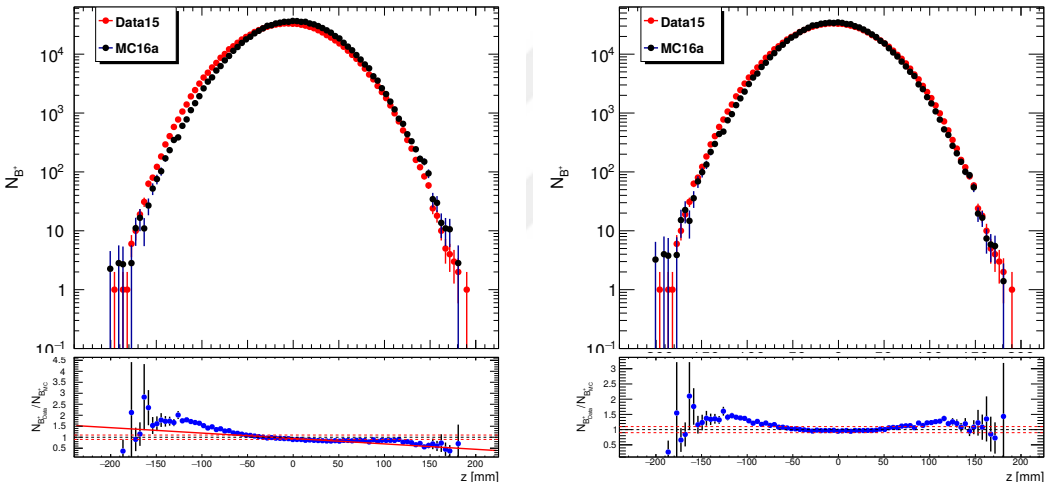

Figure D.10 Data15 (red) and MC16a (black) V_z profile. Left is before correction, right after correction is applied.

with selection cuts and trigger efficiency corrected (Left), and after correction is applied (Right). The first-order polynomial fit is applied to the Data/MC ratio in Figure D.10 (left plot) to get the weight function. The fit function and all its parameters are stored in order to be used as a weight function.

The fact that Equation D.6 is a first-order polynomial was chosen on purpose to make the techniques for determining the systematic uncertainty of these weights easier.

D.3 Number of Primary Vertices

D.3.1 Overview

There are two approaches to adjust for the number of primary vertices. A high-order polynomial fit is one approach. The alternative is to fix the ratio bin by bin. MC16a is scaled to Data15 for bin-by-bin correction, and the ratio is determined for each bin. These numbers are then used as corrections for each event. Due to this correction's minimal impact, it will be implemented in a systematic.

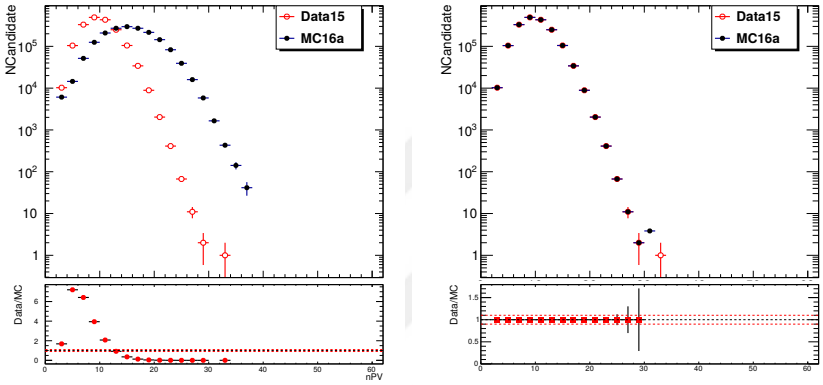

Figure D.11 Data15 (red) and MC16a (blue) nPVs Correction. Left plot shows the condition before correction and Right plot shows the condition after correction

The Data15 and Data16 number of interactions per crossing is given in the below Figure D.12, which is closely related to the number of primary vertices.

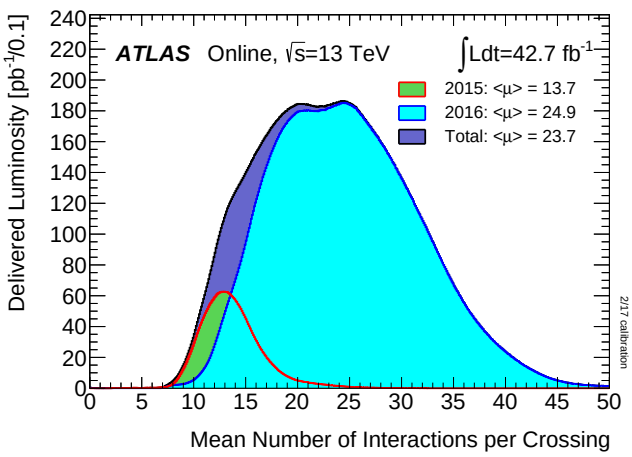

Figure D.12 Data15 and Data16 mean number of interaction per crossing ATLAS public result [53].

However, because the above method necessitates the sacrifice of the majority of the event, a new method is described and used to reweight the MC described in Appendix D.3.2.

D.3.2 Efficiency Scale Factor

Efficiency scale is a basic method to take into account of Pileup Reweighting Tool. The procedure is as the following.

- First, Official PRW correction need to be applied (Section 7.2).
- Then, Efficiency before and after PRW correction is calculated.
- Finally, the ratio is of the Efficiency histograms is extracted to get a single scale factor derived from double differential bins and used in reweighting.

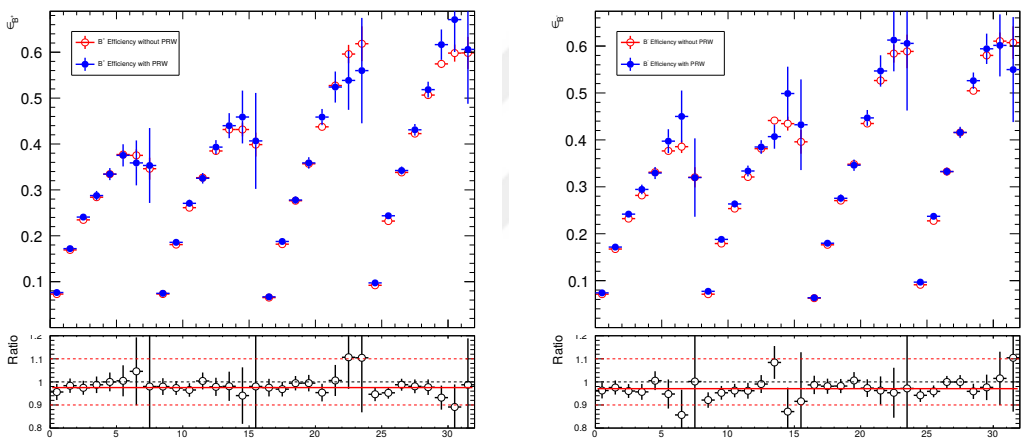

Figure D.13 B^+ and B^- efficiency in DD bin.

The Figure D.13 is showing the efficiency in DD bin with and without PRW applied. The mean of the ratio is 0.9730285 $\pm$ 0.0049158193 is calculated by applying 0th order polynomial (Pol0) fit to the ratio. The Figure D.14 is showing the efficiency in p_{T} bin with and without PRW applied. The mean of the ratio is 0.9738115 $\pm$ 0.0049186641 is calculated by applying Pol0 fit to the ratio. The Figure D.15 is showing the efficiency in $|y|$ bin with and without PRW applied. The mean of the ratio is 0.9771785 $\pm$ 0.0049239608 is calculated by applying Pol0 fit to the ratio. These three figures demonstrate that all scaling factors agree. Also tried Pol1, which agrees with Pol0. To achieve the same effect as PRW, we opted to utilize a single scale factor, which is:

$$\epsilon_{SF} = 0.973 \pm 0.005 \tag{D.7}$$

$$W_{SF} = 1/\epsilon_{SF} \tag{D.8}$$

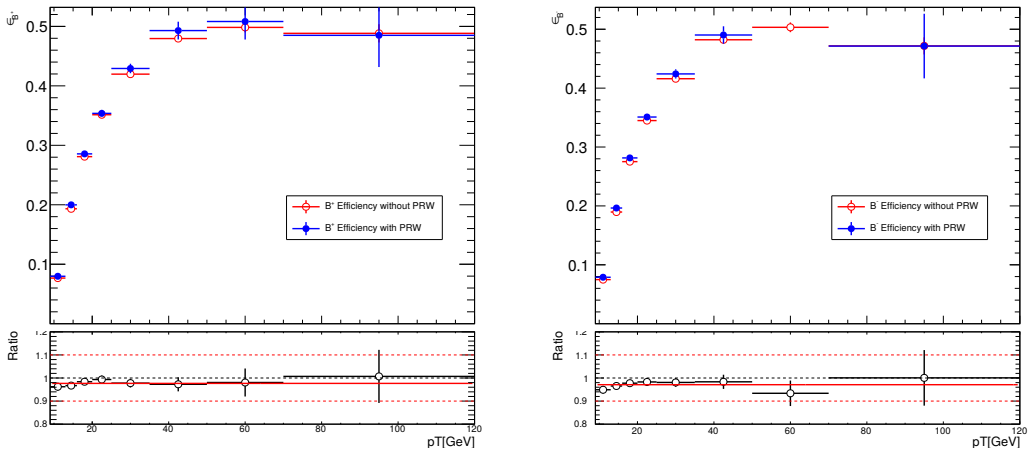

Figure D.14 B^+ and B^- efficiency in p_T bin.

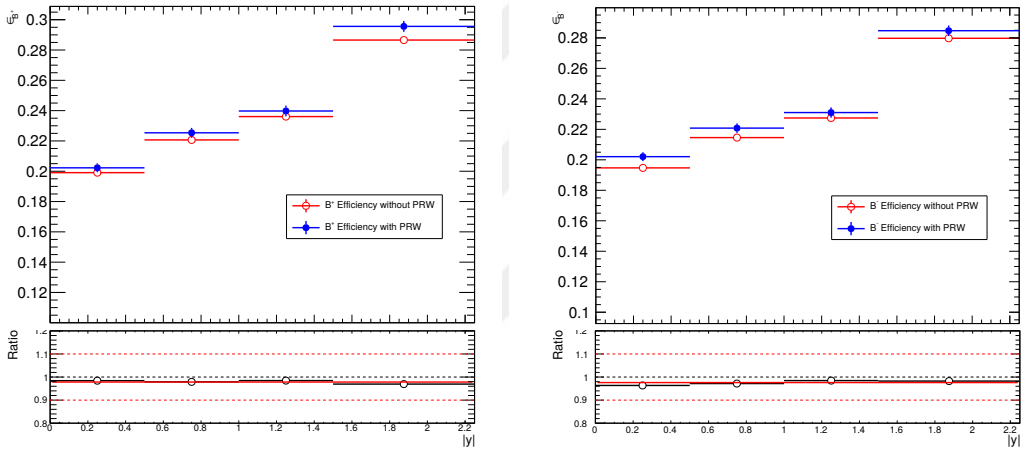

Figure D.15 B^+ and B^- Efficiency Ratio in $|y|$ bin

D.4 p_T Bin Reweighting

Reweighting for p_T and y bins is the last step in properly reweighting MC16a. Reweighting for p_T bins is covered in this section.

The procedure is straightforward. The number of B^+ candidates for Data15 and MC16a is plotted in Figure D.16 in p_T bin. Figure D.16 shows the number of B^+ candidates for Data15 and MC16a in p_T bin. Unweighted distribution is displayed in the left plot. The hyperbolic function from Equation D.9 is then used to fit the Data/MC ratio.

$$y(x) = a_0 - \frac{a_0 \cdot a_1}{x - a_2} \tag{D.9}$$

The parameters of the fit function are then stored for use as a weight function. The right plot of the Figure D.16 depicts the corrected distribution of candidates in p_T bin

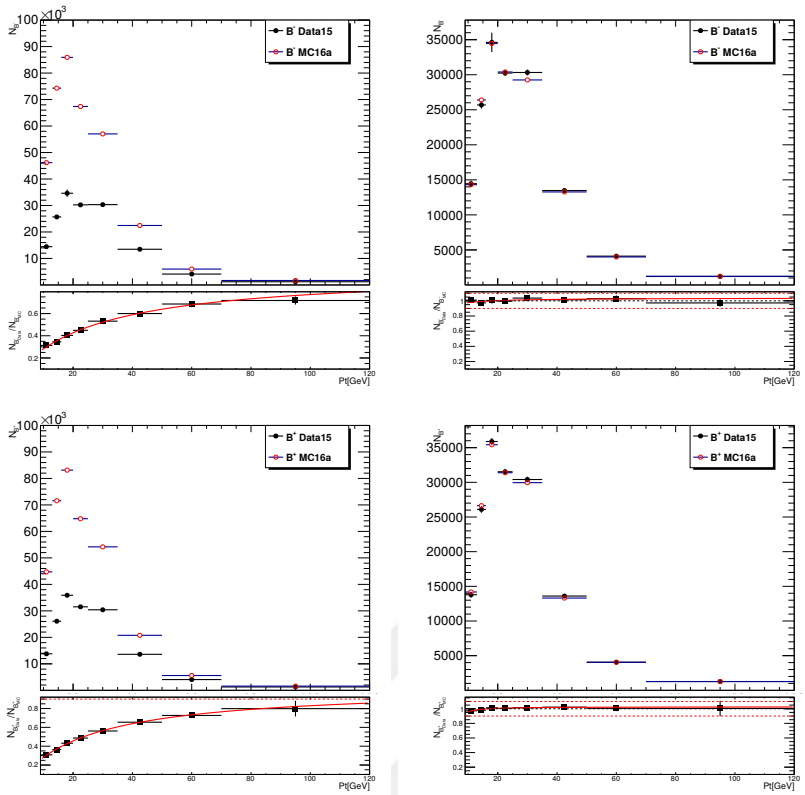

Figure D.16 Data15 (black) MC16a(red) distribution of number of candidates in p_{T} bins. (left) before applying p_{T} correction, (right) after applying p_{T} correction. Lower pad shows the $N_{B^+(Data15)}/N_{B^+(MC16a)}$ ratio while upped pad shows the charge conjugate ratio.

using y(p_{T}) hyperbolic weight function. Statistical and systematic uncertainties derived from these fit functions are explained in Section 5.

D.5 $|y|$ Bin Reweighting

After correcting in p_{T} bin defined in Appendix D.4, $|y|$ reweighting is calculated and applied. First order polynomial fits are used for $|y|$ reweighting described with Equation D.10. Left plot in Figure D.17 shows the number of B^+ candidates in $|y|$ bin for Data15 and MC16 prior to the correction.

$$f(x) = a_0 + a_1 \cdot x \tag{D.10}$$

The left plot of Figure D.17 is fitted using the first order polynomial. The fit function and parameters are preserved in order to be used as weights. The right plot of Figure D.17 shows the corrected distribution after applying the $f(|y|)$ weight function.

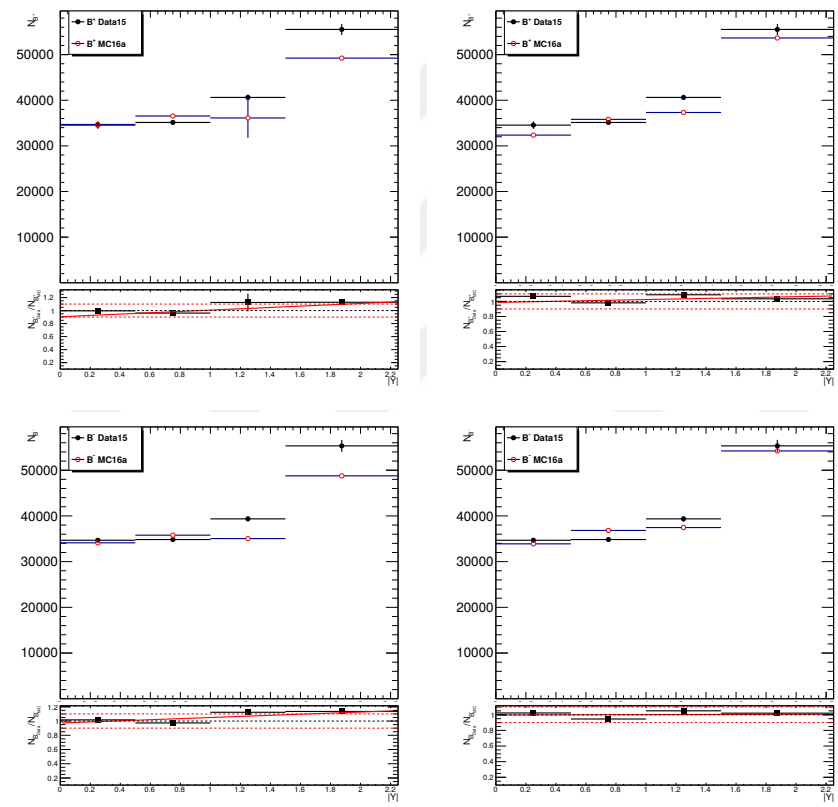

Figure D.17 The distribution of Data15 (black) and MC16a(red) number of B^- candidates in (left) before and (right) after applying $|y|$ correction. Lower pad shows the $N_{B^-}^{Data15}/N_{B^-}^{MC16a}$ ratio while upper pad shows the charge conjugate ratio.

D.6 Muon Reconstruction Scale Factor

The MCP guidelines [45] recommend using the official tool [51] to calculate the scale factors and efficiency of muon reconstruction.

Predefined working points in official tool:

- **Medium**: High efficiency down to $p_{\mathrm{T}} \sim 5$ GeV, and $0.1 < |\eta| < 2.7$ range; minor systematic uncertainties on SF.
- **Loose**: Full eta coverage and maximum efficiency down to $p_{\mathrm{T}} \sim 3$ GeV. Systematic is about twice the Medium WP.
- **Tight**: Efficiency between 5 $\%$ and 10 $\%$ below Medium WP. Uncertainty on SF is higher than Medium WP.
- **LowPt**: Maximal efficiency down to $p_{\mathrm{T}} \sim$3 GeV; systematic uncertainties on SFs comparable to Medium WP.
- **HighPt** : Best momentum resolution and removal of poorly measured high-pT tracks / "outliers", by requiring at least 3 MS stations and vetoing poorly aligned MS regions; the expected resolution roughly amounts to 12-15 $\%$ for 1 TeV tracks.

The Loose working point is used to determine the nominal, up, and down values for the associated triggers. To calculate the per-event weighting, central values are employed. For use later in the systematic calculation outlined in Section 7.6, the up and down scale factors are saved.

APPENDIX E

FIT PLOTS

B^+ and B^- yields mentioned in Section 4 are derived from the fits shown in the sections that follow. The lines and the colors are described in the legend as follows:

- Signal is defined as Modified Gaussian. Depicted as a red dotted line.
- Combinatorial background is described with Exponential Function. Shown as an orange area.
- $B^+ \to J/\psi\pi^+$ background is modeled with Kernel Density Estimation. Displayed as a green area under the signal.
- Hadronic (J/ψ X) background is described with Complementary Error Function. Shown as a pink area on the left of the plot.

E.1 B^+ p_T Bins

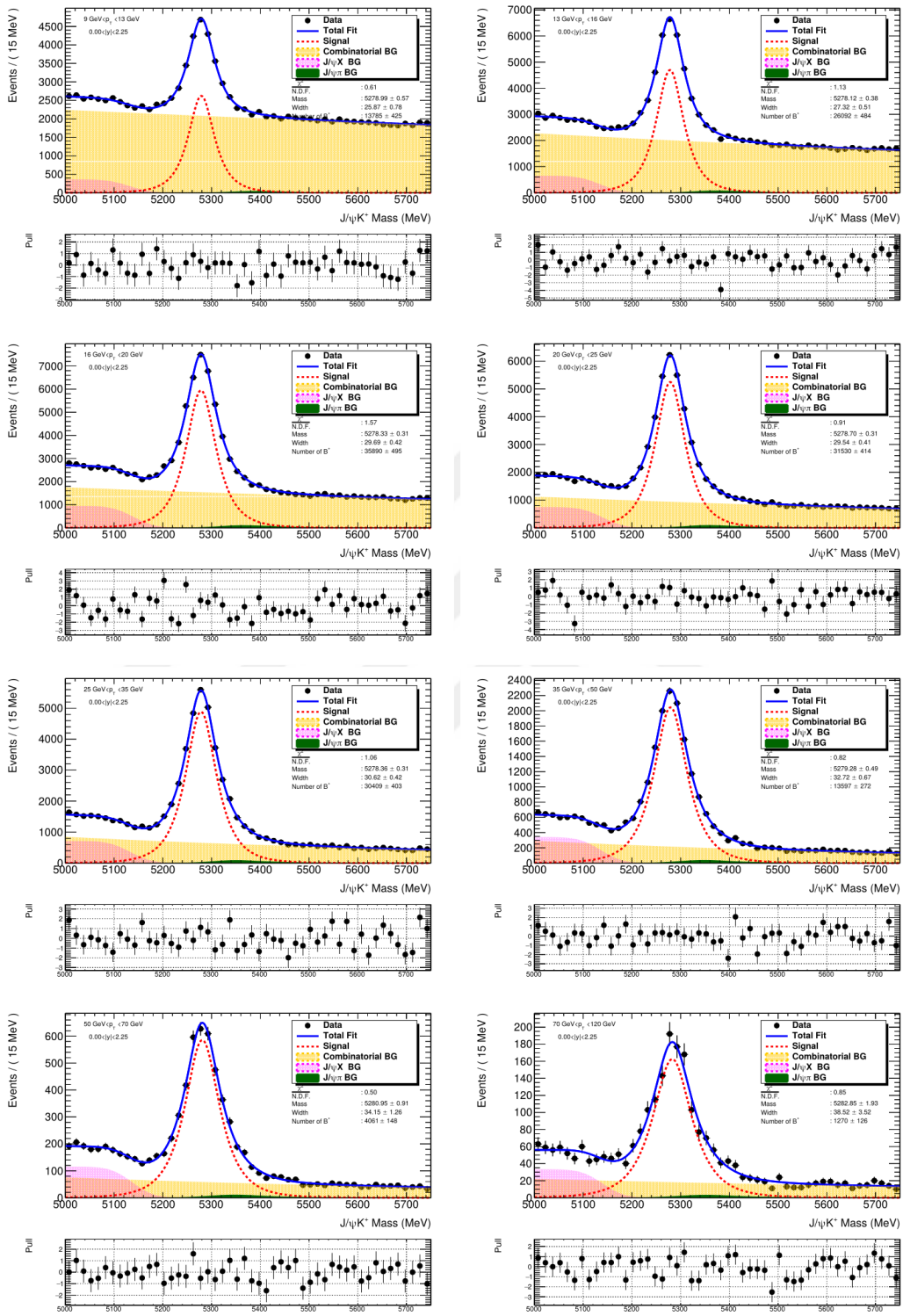

Figure E.1 B^+ candidate fit in p_T bins.

E.2 B^+ y Bins

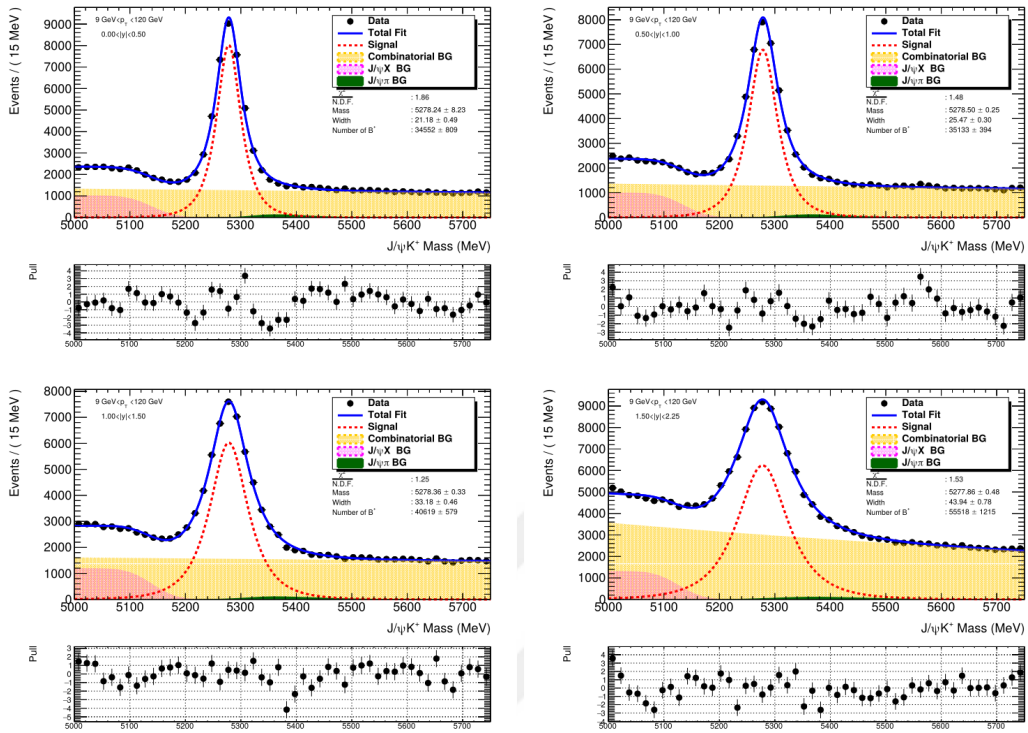

Figure E.2 B^+ candidate fit in y bins.

E.3 B^+ Double Differential Bins

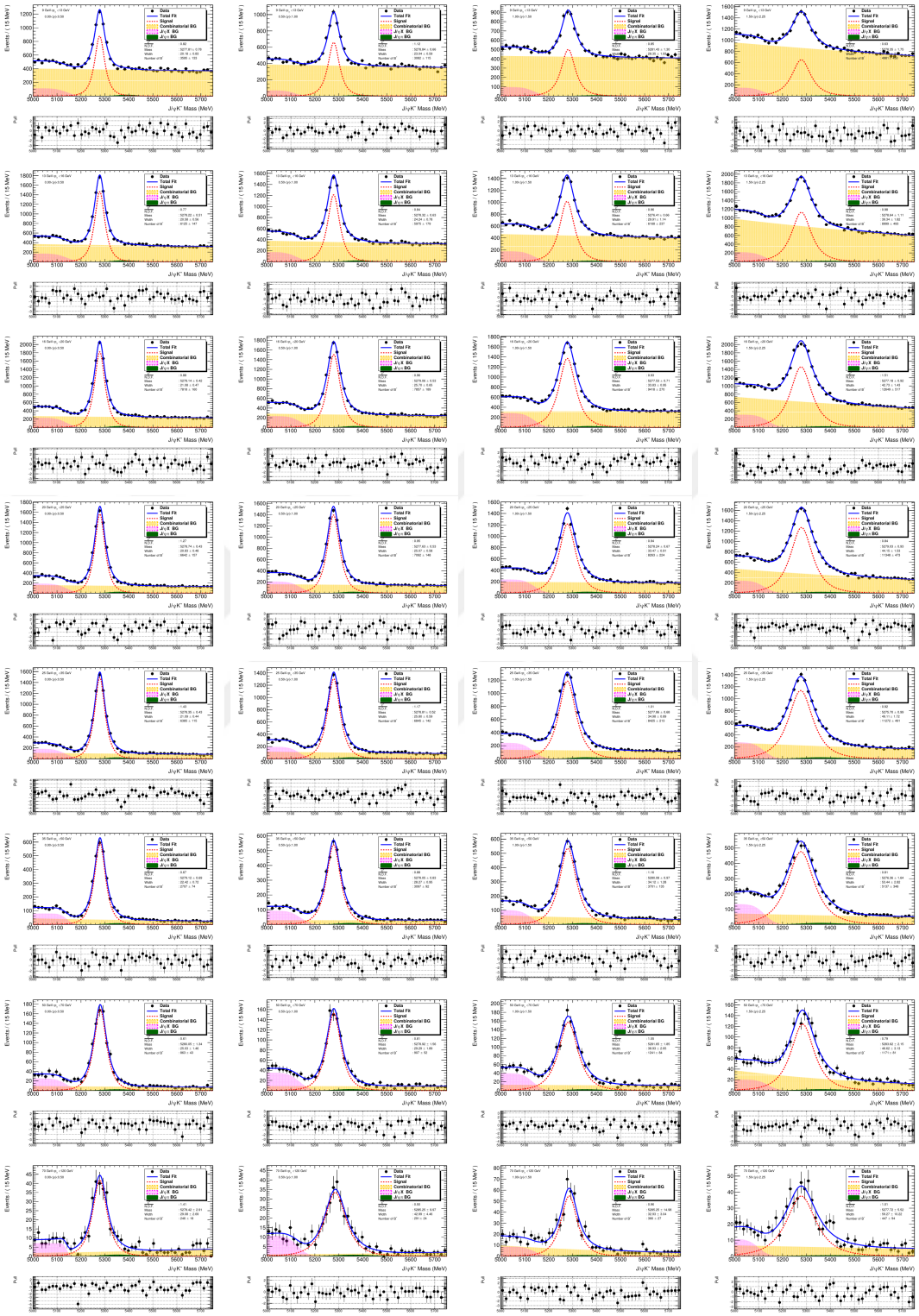

Figure E.3 B^+ candidate fit in double differential bins. Arranged up to down in p_{T} bins and left to right in $|y|$ bins.

E.4 B^- p_T Bins

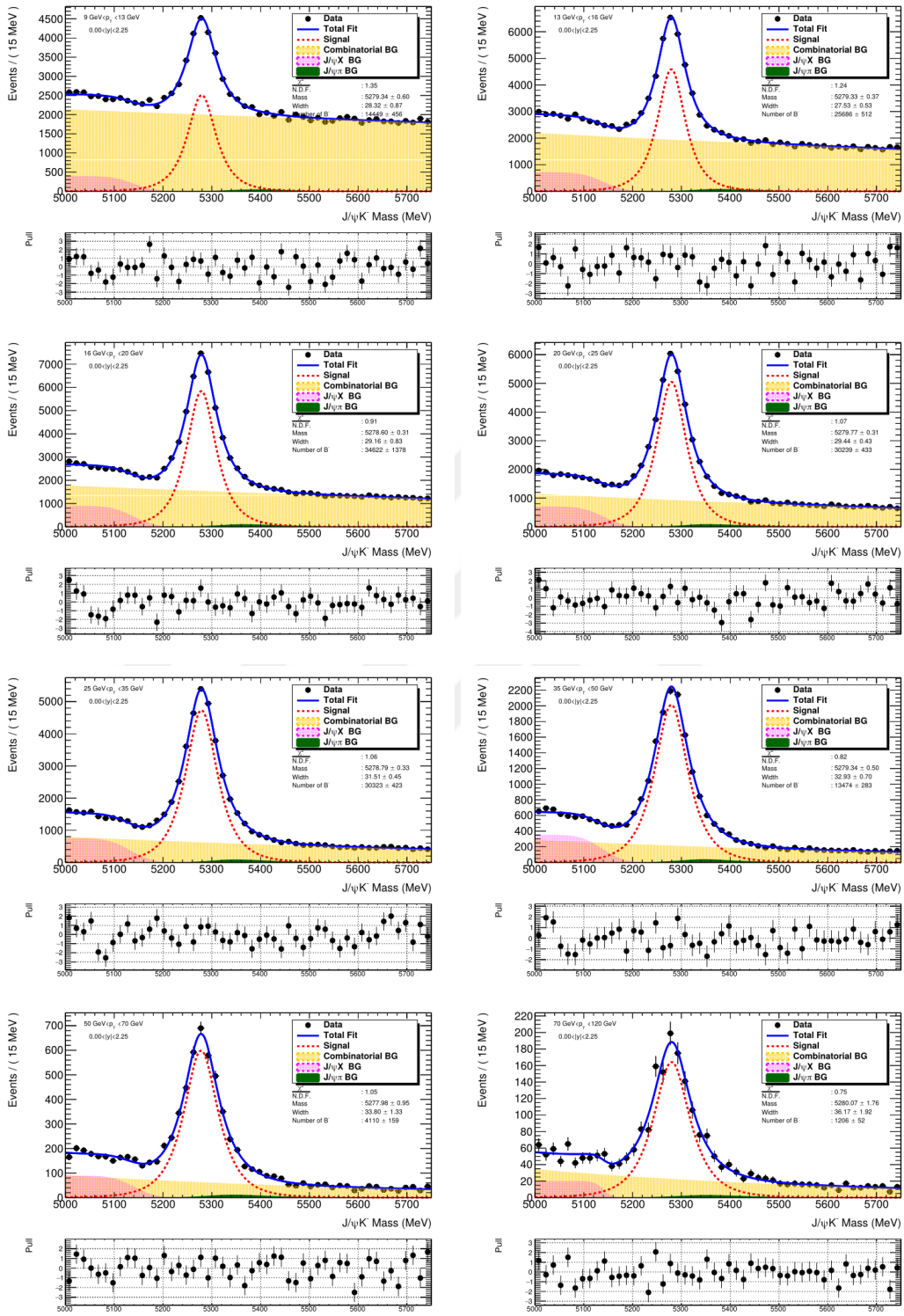

Figure E.4 B^- candidate fit in p_T bins.

E.5 B^- y Bins

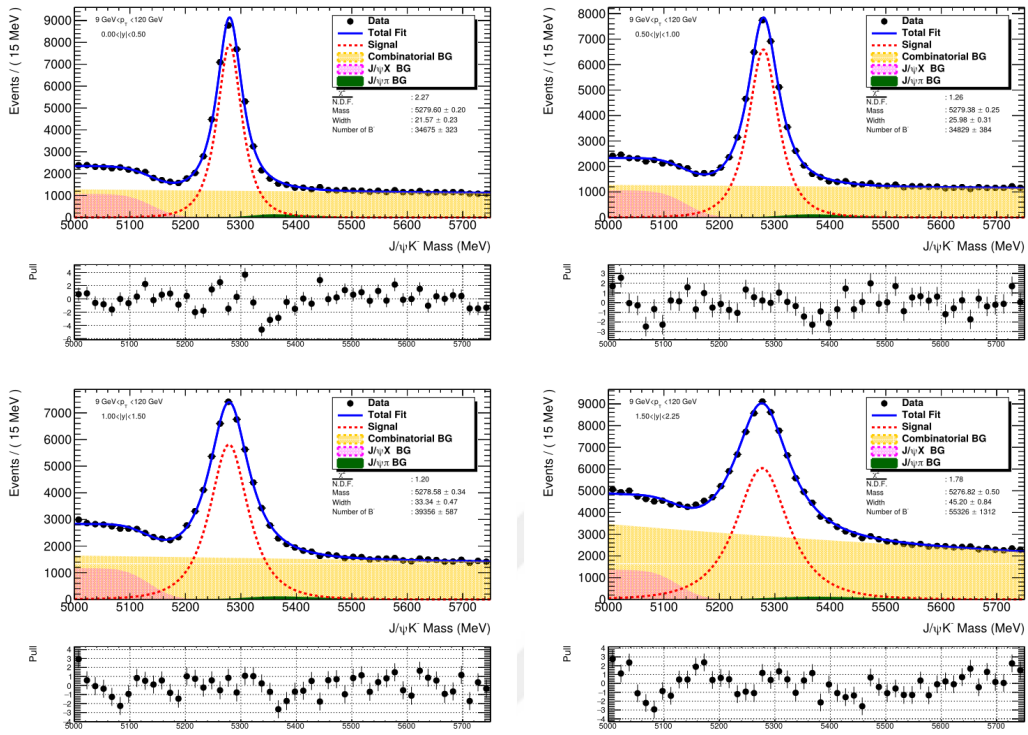

Figure E.5 B^- candidate fit in y bins.

E.6 B^- Double Differential Bins

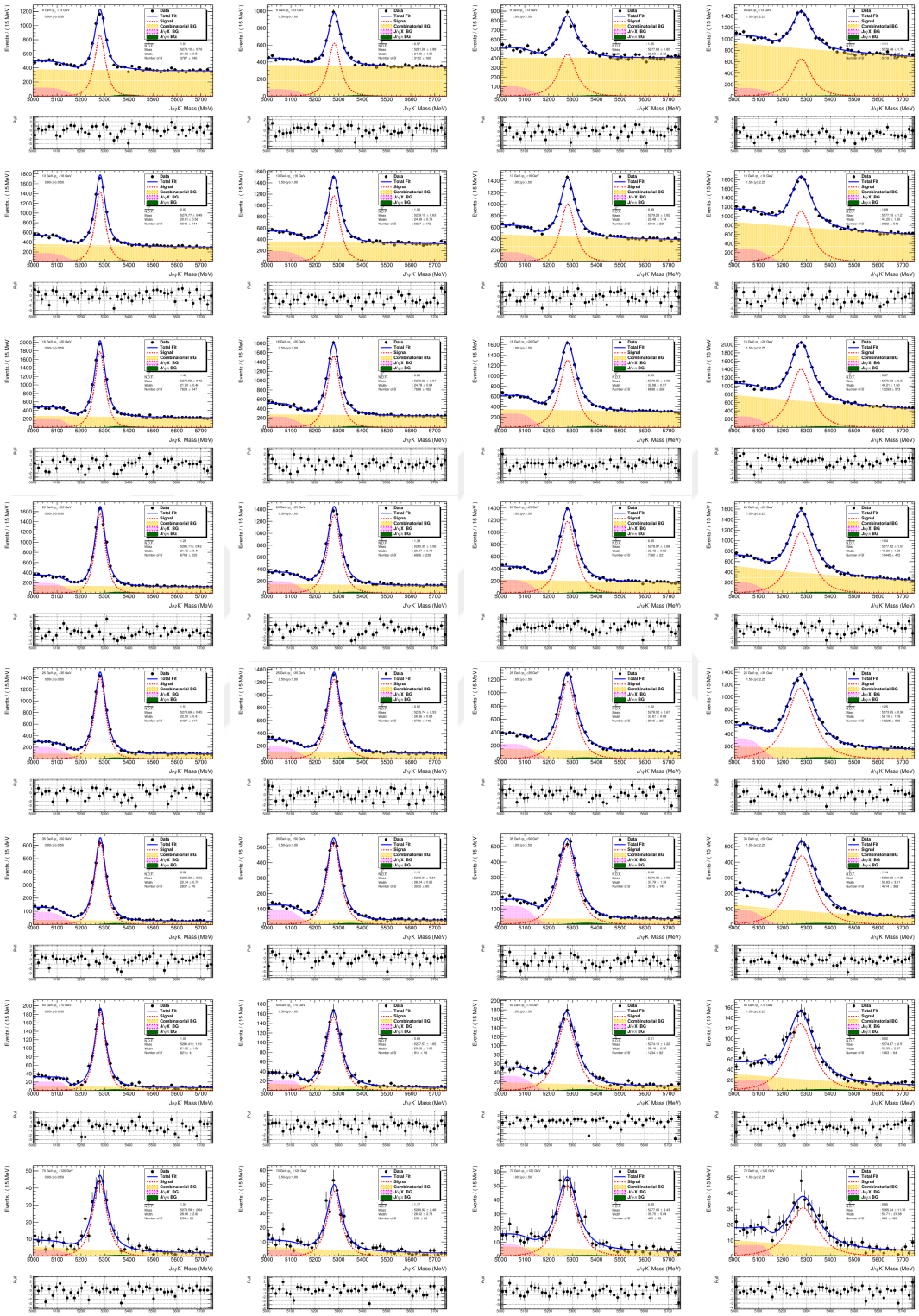

Figure E.6 B^- candidate fit in double differential bins. Arranged up to down in p_{T} bins and left to right in $|y|$ bins.

APPENDIX F

$B^{\pm}$ MASS TABLES

The average $B^{\pm}$ mass for each double differential bins which is collected from the signal yield fitting procedure, are plotted in Figure F.1 for Data15 and MC16. The weighted mean of the B^{+} mass is calculated with the unconstrained averaging formula from the PDG [48] shown in the Equation F.1.

$$\bar{x} \pm \delta\bar{x} = \frac{\sum_i w_i x_i}{\sum_i w_i} \pm \frac{1}{\sqrt{\sum_i w_i}} \tag{F.1}$$

where

$$w_i = \frac{1}{(\delta x_i)^2} \tag{F.2}$$

Below Figure F.1 shows the average $B^{\pm}$ mass per bin using the Equation F.1 for MC16a and Data15. Then by fitting the values with "Pol0"resulting fit values are shown at the Table F.1 in "Fit" row, then total average weighted mean of the B^{+} mass in is shown in "Weighted Mean" row.

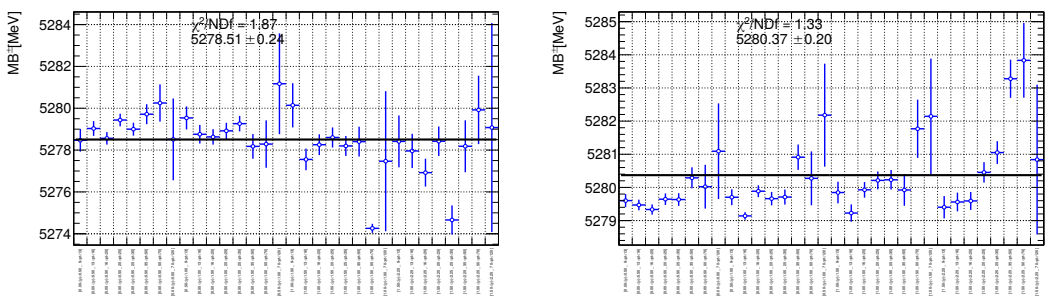

Figure F.1 Data15(Left) and MC16a(Right) $B^{\pm}$ (mean) mass distribution with its uncertainty.

Table F.1 $B^{\pm}$ candidates mass and uncertainties from double differential bins.

Type	MC16a	Data15	PDG
Fit	5280.37 ± 0.204137	5278.51 ± 0.241735	5279.34 ± 0.12
Weighted Mean	5279.68 ± 0.045153	5278.01 ± 0.086346	5279.25 ± 0.26

Table F.2 B^{+} number of candidates, mass and width extracted from the double differential bins fit results.

p_{T} [GeV]		$0.0 < \lvert y \rvert < 0.5$				$0.5 < \lvert y \rvert < 1.0$			
min	max	N B^{+}			M B^{+} [MeV]	σ B^{+} [MeV]	N B^{+}			M B^{+} [MeV]	σ B^{+} [MeV]
9.0	13.0	10 413.94	$\pm$	103.22	5278.74 ± 0.28	19.57 ± 0.20	9914.01	$\pm$	101.12	5278.87 ± 0.34	23.66 ± 0.26
13.0	16.0	14 687.75	$\pm$	121.96	5278.70 ± 0.23	18.87 ± 0.16	15 062.52	$\pm$	123.94	5278.81 ± 0.12	22.91 ± 0.09
16.0	20.0	16 322.98	$\pm$	128.49	5278.87 ± 0.22	19.11 ± 0.15	17 542.77	$\pm$	133.61	5279.05 ± 0.25	23.10 ± 0.18
20.0	25.0	12 575.53	$\pm$	112.70	5278.90 ± 0.25	19.03 ± 0.17	13 835.23	$\pm$	118.48	5278.75 ± 0.29	23.28 ± 0.20
25.0	35.0	10 528.70	$\pm$	103.15	5279.17 ± 0.27	19.24 ± 0.19	11 529.39	$\pm$	107.92	5279.30 ± 0.32	24.13 ± 0.23
35.0	50.0	4114.21	$\pm$	64.31	5279.75 ± 0.45	20.07 ± 0.32	4431.54	$\pm$	66.71	5280.81 ± 0.56	26.06 ± 0.41
50.0	70.0	1083.34	$\pm$	32.56	5280.25 ± 0.91	20.96 ± 0.66	1169.62	$\pm$	66.49	5279.74 ± 1.19	28.78 ± 0.88
70.0	120.0	276.91	$\pm$	21.70	5280.97 ± 2.08	24.51 ± 1.49	319.97	$\pm$	17.49	5283.51 ± 2.32	30.61 ± 1.69
p_{T} [GeV]		$0.0 < \lvert y \rvert < 0.5$				$0.5 < \lvert y \rvert < 1.0$			
min	max	N B^{+}			M B^{+} [MeV]	σ B^{+} [MeV]	N B^{+}			M B^{+} [MeV]	σ B^{+} [MeV]
9.0	13.0	7991.93	$\pm$	92.05	5278.98 ± 0.45	28.11 ± 0.35	13 000.23	$\pm$	116.94	5279.39 ± 0.48	38.25 ± 0.38
13.0	16.0	13 434.70	$\pm$	117.43	5277.55 ± 0.37	29.49 ± 0.27	20 522.35	$\pm$	145.19	5279.13 ± 0.40	40.03 ± 0.30
16.0	20.0	16 256.45	$\pm$	128.29	5279.34 ± 0.34	30.03 ± 0.24	24 143.05	$\pm$	156.87	5278.65 ± 0.38	41.47 ± 0.28
20.0	25.0	13 169.89	$\pm$	115.33	5279.36 ± 0.38	30.47 ± 0.27	19 006.45	$\pm$	139.21	5280.32 ± 0.43	42.02 ± 0.33
25.0	35.0	11 474.59	$\pm$	106.97	5279.74 ± 0.42	31.54 ± 0.30	15 775.94	$\pm$	127.00	5280.50 ± 0.49	42.99 ± 0.37
35.0	50.0	4641.57	$\pm$	68.42	5278.89 ± 0.69	32.75 ± 0.50	5885.74	$\pm$	77.58	5282.71 ± 0.82	44.41 ± 0.63
50.0	70.0	1344.83	$\pm$	36.59	5282.61 ± 1.23	32.14 ± 0.91	1552.68	$\pm$	39.96	5282.71 ± 1.67	46.98 ± 1.35
70.0	120.0	402.91	$\pm$	20.66	5282.82 ± 2.34	34.69 ± 2.11	435.15	$\pm$	21.34	5277.58 ± 3.41	50.85 ± 2.91

Table F.3 B^{-} number of candidates, mass and width extracted from the double differential bins fit results.

p_{T} [GeV]		$0.0 < \lvert y \rvert < 0.5$				$0.5 < \lvert y \rvert < 1.0$			
min	max	N B^{-}			M B^{-} [MeV]	σ B^{-} [MeV]	N B^{-}			M B^{-} [MeV]	σ B^{-} [MeV]
9.0	13.0	10 099.00	$\pm$	101.52	5280.47 ± 0.28	19.63 ± 0.20	9694.84	$\pm$	100.11	5280.49 ± 0.33	23.15 ± 0.26
13.0	16.0	14 510.16	$\pm$	121.26	5280.25 ± 0.23	19.27 ± 0.16	14 798.69	$\pm$	122.93	5280.69 ± 0.27	23.26 ± 0.20
16.0	20.0	16 290.35	$\pm$	128.35	5279.80 ± 0.22	19.45 ± 0.16	17 022.82	$\pm$	131.50	5280.75 ± 0.26	23.35 ± 0.19
20.0	25.0	12 579.66	$\pm$	112.68	5280.39 ± 0.25	19.36 ± 0.18	13 756.81	$\pm$	118.09	5280.59 ± 0.29	23.74 ± 0.21
25.0	35.0	10 702.85	$\pm$	103.69	5280.11 ± 0.27	19.67 ± 0.19	11 653.66	$\pm$	108.54	5280.11 ± 0.32	24.15 ± 0.23
35.0	50.0	4212.11	$\pm$	64.92	5280.84 ± 0.45	20.55 ± 0.32	4685.35	$\pm$	68.92	5281.00 ± 0.53	25.45 ± 0.39
50.0	70.0	1089.54	$\pm$	32.86	5279.78 ± 0.95	21.98 ± 0.69	1194.74	$\pm$	34.73	5280.73 ± 1.11	27.18 ± 0.85
70.0	120.0	281.66	$\pm$	16.70	5281.21 ± 2.01	24.58 ± 1.59	325.92	$\pm$	18.17	5281.10 ± 2.09	26.86 ± 1.60
p_{T} [GeV]		$0.0 < \lvert y \rvert < 0.5$				$0.5 < \lvert y \rvert < 1.0$			
min	max	N B^{-}			M B^{-} [MeV]	σ B^{-} [MeV]	N B^{-}			M B^{-} [MeV]	σ B^{-} [MeV]
9.0	13.0	7673.43	$\pm$	90.41	5280.78 ± 0.47	29.04 ± 0.38	12 900.43	$\pm$	121.46	5279.42 ± 0.48	37.62 ± 0.41
13.0	16.0	13 100.41	$\pm$	117.38	5280.80 ± 0.36	29.19 ± 0.29	20 311.48	$\pm$	144.67	5279.99 ± 0.40	40.21 ± 0.31
16.0	20.0	15 945.39	$\pm$	127.84	5280.49 ± 0.33	29.33 ± 0.25	24 138.43	$\pm$	157.12	5280.53 ± 0.38	41.81 ± 0.29
20.0	25.0	12 997.42	$\pm$	114.36	5281.07 ± 0.38	30.65 ± 0.27	18 977.45	$\pm$	138.91	5280.59 ± 0.44	42.61 ± 0.33
25.0	35.0	11 533.13	$\pm$	109.15	5280.70 ± 0.41	31.15 ± 0.32	16 166.12	$\pm$	128.40	5281.59 ± 0.48	43.32 ± 0.36
35.0	50.0	4761.98	$\pm$	69.30	5280.85 ± 0.66	32.04 ± 0.48	6213.14	$\pm$	79.30	5283.83 ± 0.81	45.09 ± 0.61
50.0	70.0	1385.21	$\pm$	37.54	5280.88 ± 1.26	32.98 ± 0.97	1664.44	$\pm$	41.19	5284.76 ± 1.52	47.09 ± 1.29
70.0	120.0	404.68	$\pm$	20.10	5281.32 ± 2.60	37.07 ± 1.96	456.72	$\pm$	21.98	5283.37 ± 3.01	48.29 ± 2.65

APPENDIX G

FONLL TABLES

FONLL stands for "fixed-order next-to-leading logarithmic." In the context of QCD calculations, FONLL refers to a specific approach that is used to calculate the production cross section of heavy quarks in high-energy particle collisions. FONLL calculations are based on perturbation theory and include both fixed-order and next-to-leading logarithmic corrections to the leading-order result.

Next-to-leading order theoretical predictions used in this analysis are shown in below tables. Instead of CTEQ6.6, the new PDF function called NNPDF30 is used. The web interface for FONLL [40] is used for calculation. p_{T} bin FONLL is calculated in 8 bins for the fixed $|y| < 2.25$ range . y bin FONLL is calculated for 4 bins for the fixed 9<p_{T} < 120 GeV range, and double differential bin is calculated per p_{T} and y bin which is in total 32 bins.

Bottom quark with the meson final state is selected. BR(q->meson) = 1 is set, where NNPDF30 PDF set is used. In the final stage $f_{b\to B^+}$ ratio is applied. The following tables shows the values used in the cross-section plots.

G.1 FONLL $\sqrt{s} = 13$ TeV

13 TeV FONLL Data used in cross-section plots are shown below:

G.1.1 p_{T} Bin

Table G.1 FONLL 13 TeV in p_{T} bins σ_{B^+} (13 TeV) [nb/GeV] ($|y| < 2.25$).

p_{T} [GeV]		σ_{B^+} (13 TeV) [nb/GeV]		
min	max	central	min	max
9.00	13.00	2424.540	1801.320	3349.680
13.00	16.00	1017.144	792.608	1359.320
16.00	20.00	487.866	387.906	634.032
20.00	25.00	212.405	172.584	267.811
25.00	35.00	69.850	58.181	85.109
35.00	50.00	15.373	13.181	18.009
50.00	70.00	2.980	2.615	3.384
70.00	120.00	0.368	0.329	0.408

G.1.2 y Bin

Table G.2 FONLL 13 TeV in y bins σ_{B^+} (13 TeV) [nb] (9<p_{T} <120 GeV).

y		σ_{B^+} (13 TeV) [nb]		
min	max	central	min	max
0.00	0.50	4106.112	3172.608	5521.056
0.50	1.00	3984.528	3085.296	5357.856
1.00	1.50	3744.624	2907.408	5037.168
1.50	2.25	3289.024	2551.360	4429.792

G.1.3 Double Differential Bin

Table G.3 FONLL 13 TeV in DD bins (σ_{B^+} (13 TeV) [nb/GeV]).

p_{T} [GeV]		$(0.0 < y < 0.5)$			$(0.5 < y < 1.0)$		
min	max	central	min	max	central	min	max
9.00	13.00	293.352	216.240	405.348	285.702	211.242	394.842
13.00	16.00	124.766	97.213	166.736	120.999	94.275	161.704
16.00	20.00	60.496	48.093	78.622	58.466	46.481	75.970
20.00	25.00	26.667	21.673	33.627	25.663	20.857	32.363
25.00	35.00	8.919	7.430	10.865	8.535	7.116	10.400
35.00	50.00	2.015	1.728	2.360	1.913	1.640	2.240
50.00	70.00	0.404	0.355	0.458	0.379	0.333	0.430
70.00	120.00	0.052	0.047	0.058	0.048	0.043	0.053
p_{T} [GeV]		$(1.0 < y < 1.5)$			$(1.5 < y < 2.25)$		
min	max	central	min	max	central	min	max
9.00	13.00	270.606	201.144	373.932	241.536	181.492	333.812
13.00	16.00	113.574	88.495	151.776	99.461	77.529	133.008
16.00	20.00	54.478	43.319	70.788	47.002	37.366	61.084
20.00	25.00	23.721	19.274	29.906	20.095	16.331	25.340
25.00	35.00	7.801	6.499	9.502	6.446	5.369	7.853
35.00	50.00	1.716	1.472	2.010	1.362	1.168	1.596
50.00	70.00	0.332	0.292	0.377	0.250	0.219	0.284
70.00	120.00	0.041	0.036	0.045	0.028	0.025	0.031

G.2 FONLL $\sqrt{s} = 7$ TeV

The 7 TeV FONLL data used in plotting is shown below tables. FONLL is calculated inside representing p_{T} and y bin total cross section. $f_{b\to B^+}$ ratio is already applied in the tables. Also other parameters are: quark = bottom, final state = meson.
BR(q->meson) = 1, PDF set = NNPDF30 .

G.2.1 p_{T} Bin

Table G.4 FONLL 7 TeV in p_{T} bin.

p_{T} [GeV]		σ_{B^+} (7 TeV) [nb/GeV] ($\lvert y\rvert < 2.25$)		
min	max	central	min	max
9.00	13.00	1302.540	994.704	1792.140
13.00	16.00	512.856	400.520	682.992
16.00	20.00	234.396	186.660	303.858
20.00	25.00	96.778	78.679	121.829
25.00	35.00	29.735	24.766	36.234
35.00	50.00	5.935	5.084	6.969
50.00	70.00	1.026	0.898	1.168
70.00	120.00	0.109	0.097	0.122

G.2.2 y Bin

Table G.5 FONLL 7 TeV in y bin.

y		σ_{B^+} (7 TeV) [nb] (9<p_{T} <120 GeV)		
min	max	central	min	max
0.00	0.50	2161.584	1680.144	2902.512
0.50	1.00	2078.352	1615.680	2792.352
1.00	1.50	1917.600	1489.200	2577.744
1.50	2.25	1617.312	1255.008	2177.632

APPENDIX H

GM-VFNS TABLES

GM-VFNS stands for "general-mass variable-flavor-number scheme." In the context of QCD calculations, GM-VFNS refers to a specific approach that is used to calculate the production cross section of heavy quarks in high-energy particle collisions. GM-VFNS calculations are based on perturbation theory and are designed to be applicable to a wide range of heavy quark masses and flavors. In this section, 13 TeV and 7 TeV cross section theoretical predictions are summarized which are calculated by using NNPDF30 (nlo_as0118) and mb=4.75 GeV, except for the scale setting.

H.1 GM-VFNS $\sqrt{s} = 13$ TeV

H.1.1 p_{T} Bin

Table H.1 contains $d\sigma/dp_{\mathrm{T}}$ integrated over the full rapidity range $-2.25 < y < +2.25$ in units of nb/GeV.

Table H.1 13 TeV GM-VFNS predictions for the p_{T} bin

p_{T} [GeV]		σ_{B^+} (13 TeV) [nb/GeV] ($\lvert y\rvert < 2.25$)		
min	max	central	min	max
9.00	13.00	2744.900	2187.900	3524.500
13.00	16.00	1039.300	845.210	1297.700
16.00	20.00	473.850	391.630	579.300
20.00	25.00	198.930	167.040	237.640
25.00	35.00	63.941	54.692	74.513
35.00	50.00	14.008	12.248	15.872
50.00	70.00	2.760	2.459	3.053
70.00	120.00	0.349	0.317	0.379

H.1.2 y Bin

Table H.2 shows the differential cross-sections for $d\sigma/dy$ for bins with only the positive sign of y. One need to have to take a factor of 2 into account when sum up all given values to get a total cross-section.

Table H.2 13 TeV GM-VFNS predictions for the y bin

y		σ_{B^+} (13 TeV) [nb] ($9 < p_{\mathrm{T}} < 120$ GeV)		
min	max	central	min	max
0.00	0.50	4360.700	3533.500	5505.900
0.50	1.00	4235.400	3432.600	5346.500
1.00	1.50	3989.500	3233.700	5034.500
1.50	2.25	3518.800	2852.800	4438.400

H.1.3 Double Differential Bin

The Table H.3 contains cross-section with $d\sigma/dp_{\mathrm{T}}$ integrated over bins with given positive y-values.

Table H.3 13 TeV GM-VFNS predictions for the Double Differential bin.

p_{T} [GeV]		σ_{B^+} (13 TeV) [nb/GeV] ($0.0 < y < 0.5$)			σ_{B^+} (13 TeV) [nb/GeV] ($0.5 < y < 1.0$)		
min	max	central	min	max	central	min	max
9.00	13.00	330.560	425.680	263.990	322.080	414.610	257.270
13.00	16.00	126.890	158.900	103.330	123.150	154.160	100.320
16.00	20.00	58.537	71.745	48.406	56.629	69.379	46.840
20.00	25.00	24.889	29.830	20.916	23.984	28.734	20.160
25.00	35.00	8.145	9.524	6.970	7.808	9.125	6.683
35.00	50.00	1.835	2.086	1.604	1.744	1.982	1.525
50.00	70.00	0.374	0.415	0.333	0.352	0.390	0.313
70.00	120.00	0.050	0.054	0.045	0.046	0.050	0.042

p_{T} [GeV]		σ_{B^+} (13 TeV) [nb/GeV] ($1.0 < y < 1.5$)			σ_{B^+} (13 TeV) [nb/GeV] ($1.5 < y < 2.25$)		
min	max	central	min	max	central	min	max
9.00	13.00	305.430	392.960	244.060	409.920	526.850	327.770
13.00	16.00	115.810	144.870	94.376	152.610	190.650	124.480
16.00	20.00	52.877	64.732	43.758	68.621	83.869	56.847
20.00	25.00	22.208	26.583	18.677	28.293	33.803	23.824
25.00	35.00	7.146	8.344	6.120	8.872	10.338	7.608
35.00	50.00	1.568	1.779	1.371	1.867	2.114	1.636
50.00	70.00	0.309	0.342	0.275	0.348	0.385	0.311
70.00	120.00	0.039	0.042	0.035	0.041	0.044	0.037

H.2 GM-VFNS $\sqrt{s} = 7$ TeV

The 7 TeV GM-VFNS data used in plotting is shown below tables.

H.2.1 p_{T} Bin

Table H.4 7 TeV GM-VFNS predictions for the p_{T} bin

p_{T} [GeV]		σ_{B^+} (7 TeV) [nb/GeV]		
min	max	central	min	max
9.00	13.00	1518.400	1205.900	1917.300
13.00	16.00	537.520	438.330	662.270
16.00	20.00	233.620	193.570	281.340
20.00	25.00	92.511	78.188	109.170
25.00	35.00	27.770	23.868	31.900
35.00	50.00	5.506	4.829	6.140
50.00	70.00	0.965	0.861	1.050
70.00	120.00	0.105	0.095	0.112

H.2.2 y Bin

Table H.5 7 TeV GM-VFNS predictions for the y bin

y		σ_{B^+} (7 TeV) [nb/GeV]		
min	max	central	min	max
0.00	0.50	2355.200	1916.000	2954.600
0.50	1.00	2267.800	1845.000	2844.300
1.00	1.50	2097.000	1706.400	2628.800
1.50	2.25	1776.600	1446.400	2225.500

APPENDIX I

ATLAS SERVICE WORKS

I.1 Introduction

This section outlines the service work personally undertaken or attended to during the ATLAS qualification task and other upgrade projects that began in 2017. For the qualification task, I received training as a DCS and detector expert and subsequently contributed to detector maintenance in the USA15 and UX15. In order to gain familiarity with RPC technology, I assisted in the repair and recommissioning of the BME RPCs. I provided support for the development of the DAQ system for the test beam and the BIS78 project, in collaboration with Alessandro Polini, who is responsible for the BIS78 DAQ. Specifically, I contributed to the development of the BIS78's readout monitoring system and its connection to the DCS. These works can be grouped into the following sections:

- Installation, test, and commissioning of RPC BME chambers
- BIS78 resistive plate chambers upgrade
- RPC prototype tests in GIF++ and H8

I.2 Installation, Test, and Commissioning of RPC BME Chambers

During the extended year-end technical stop (EYETS 2017) from December 2016 to May 2017, the ATLAS detector underwent maintenance and upgrades, including the commissioning of RPC BME chambers. The aim of the EYETS was to carry out essential maintenance, repairs, and upgrades on the LHC and its detectors to ensure their readiness for the upcoming run period.

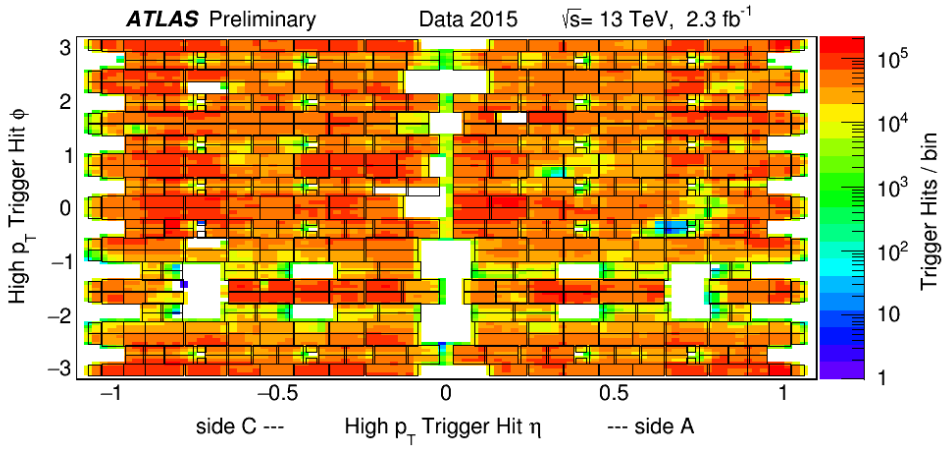

Figure I.1 RPC trigger hit occupancy for Data 2015 [57].

Figure I.1 shows the RPC trigger hit distribution for 2015 data. The region around η = 0 corresponds to holes in the barrel structure due to the services, while the holes in the acceptance at around ϕ = -1 and ϕ = -2 are caused by the mechanical structures supporting the ATLAS calorimeters in the region of the ATLAS feet, preventing full coverage of the barrel. The RPC chambers BME and BOE, as well as the additional BOG and BOF chambers in the outer part of the feet sectors, are not included in this plot as their commissioning and integration into the ATLAS DAQ was completed after the 2015 run. The BME sMDT chambers are designed to cover the gaps in the ATLAS Muon Spectrometer due to the elevator region of the ATLAS detector [58]. To cover the non-instrumented area around the ATLAS feet region, BMEs are commissioned. This work involves the following steps:

- Preparing BME gas gaps and construction of the chambers.
- Cabling BME chambers and testing with cosmic muons.
- The combination of BME RPC chambers with their MDT counterparts and combined tests.
- Installing BME chambers in ATLAS cavern.

As a starting point for these operations, front ends are soldered to gas gaps, and the faraday cages are closed once the eta and phi layers are carefully positioned. The wires shown in Figure I.2 are then prepared and placed on the eta and phi sides, with their front ends linked to pad boards. After thorough testing, the RPCs are integrated onto the MDTs, and combined testing with cosmics is carried out. Finally, the BME chambers are installed in their predetermined locations on the ATLAS detector.

Figure I.2 Cabling of the BME chambers.

I.3 BIS78 Resistive Plate Chambers Upgrade

As part of the BIS78 upgrade project, the previous RPC detectors will be substituted with advanced ones, specifically designed to perform reliably at higher collision rates, and offer increased efficiency and stability. The new detectors will be initially tested during Run3 by installing them in the inner sectors 7 and 8 of the ATLAS barrel. To facilitate the operation of the upgraded detectors, a comprehensive upgrading effort was undertaken that included the development of new readout electronics, data gathering systems, analysis software, and various tools. Since the sensors and electronics installed

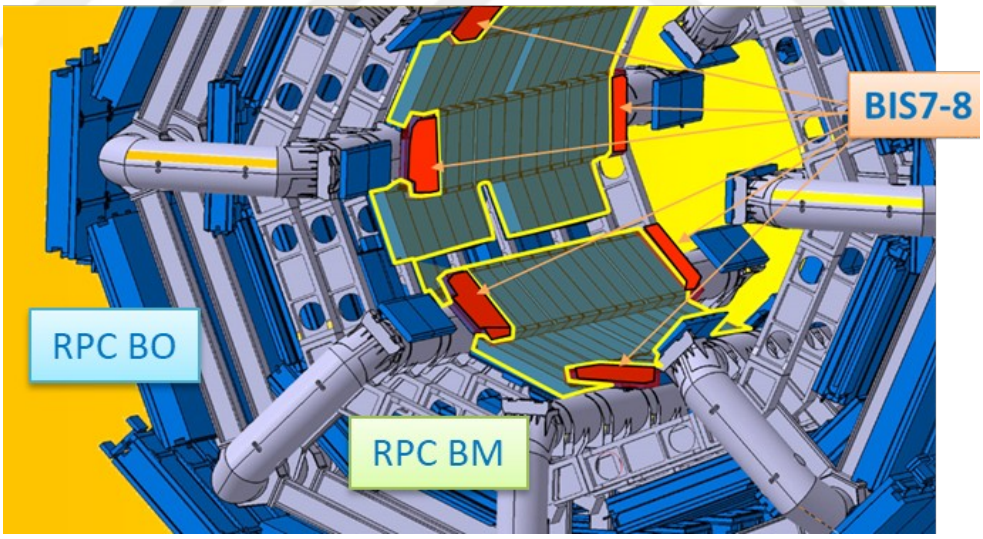

Figure I.3 Position of BIS78 chambers.

in the LHC are expected to operate under high radiation levels, it's crucial to evaluate their performance and stability under such conditions. To address this requirement, the GIF++ facility offers the necessary infrastructure to test devices in high-radiation environments, making it one of the few facilities with such capabilities. In summary, the work can be outlined as follows:

- Assembling of BIS78 prototype at BB5.
- BIS78 GIF++ tests.
- Testing OPC-UA server and developing OPC-UA client.
- Development of online and offline DAQ software.

Figure I.4 shows the construction of the BIS78 prototype. The front ends are soldered to each gas gap, and the new prototype is composed of three layers. The high voltage and gas connections are then prepared, and the prototype is sealed with a Faraday cage. Once the BIS78 prototype is assembled in BB5, it is tested using cosmic rays

Figure I.4 Assembling of the prototype.

with the setup depicted in Figure I.5. The setup comprises of two scintillators with trigger logic, a CAEN TDC for data acquisition, and a server for data collection and storage. Following these tests, the prototype is then evaluated at the GIFF++ facility, as mentioned in Section I.4.

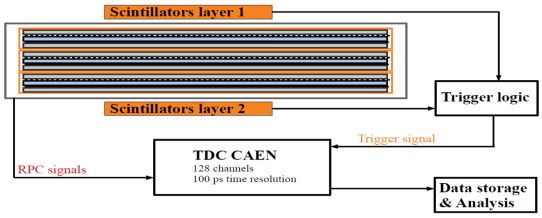

Figure I.5 Basic test setup used in BB5 [59].

Since the new BIS78 prototype employs a new frontend connected to a faster TDC known as HP-TDC, new DAQ devices were evaluated and configured accordingly.HP-TDCs are housed by the TDC mezanine[1] , Figure I.6 shows the TDC mezzanine containing the HP-TDC and trigger pad, here each TDC card has three TDC having 32 channels with 200 ps time resolution. Data is flowing through FE (Front End) to HP-TDC. An additional challenge was collecting the detector conditions from the

[1] A mezzanine card, also known as a "daughterboard", is a printed circuit board that plugs directly into another plug-in card.

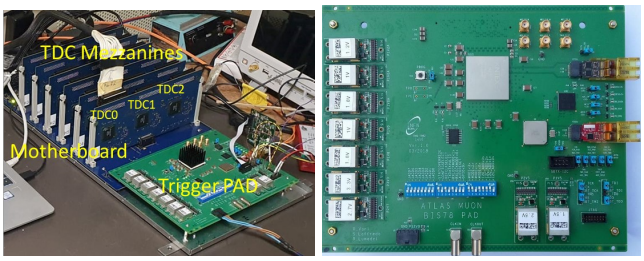

Figure I.6 TDC Mezzanine which contains trigger pad and HP-TDC boards (Left), Trigger pad (Right).

trigger pad, which required the adoption of a new communication protocol known as OPC-UA. OPC-UA (Open Platform Communications - Unified Architecture) is a machine-to-machine communication protocol for industrial automation developed by the OPC Foundation. OPC-UA is a service-oriented architecture that is independent of platforms, and it combines all the features of the OPC Classic specifications into a single, flexible framework [60]. Using the OPC-UA server and client illustrated in Figure I.8 and I.8, we gather detector condition data, including current, voltage, etc. One also can send the JTAG command through this chain. These functions are depicted in greater detail in Figure I.7.

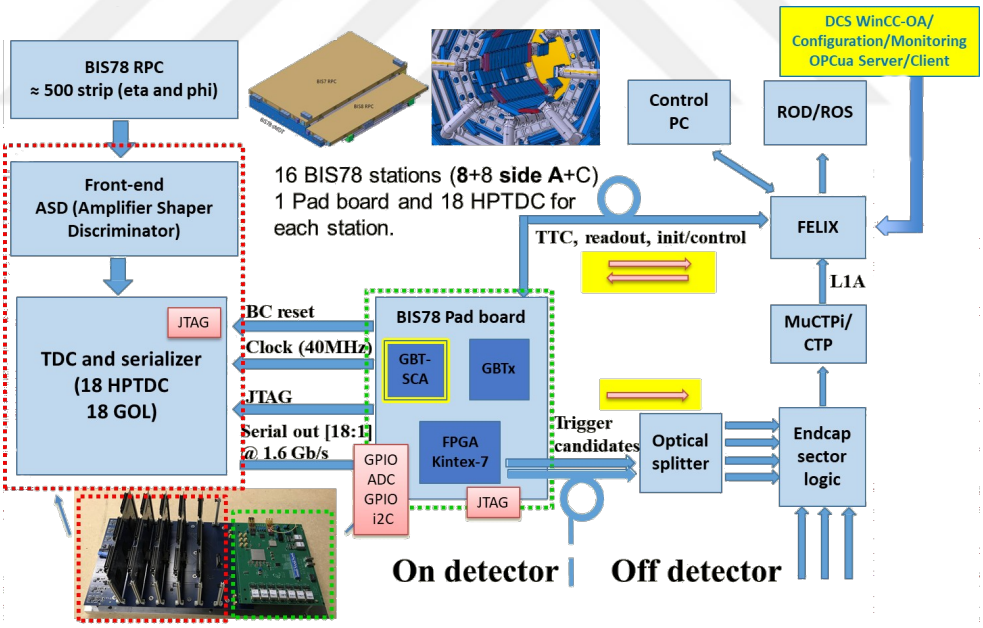

Figure I.7 OPC setup.

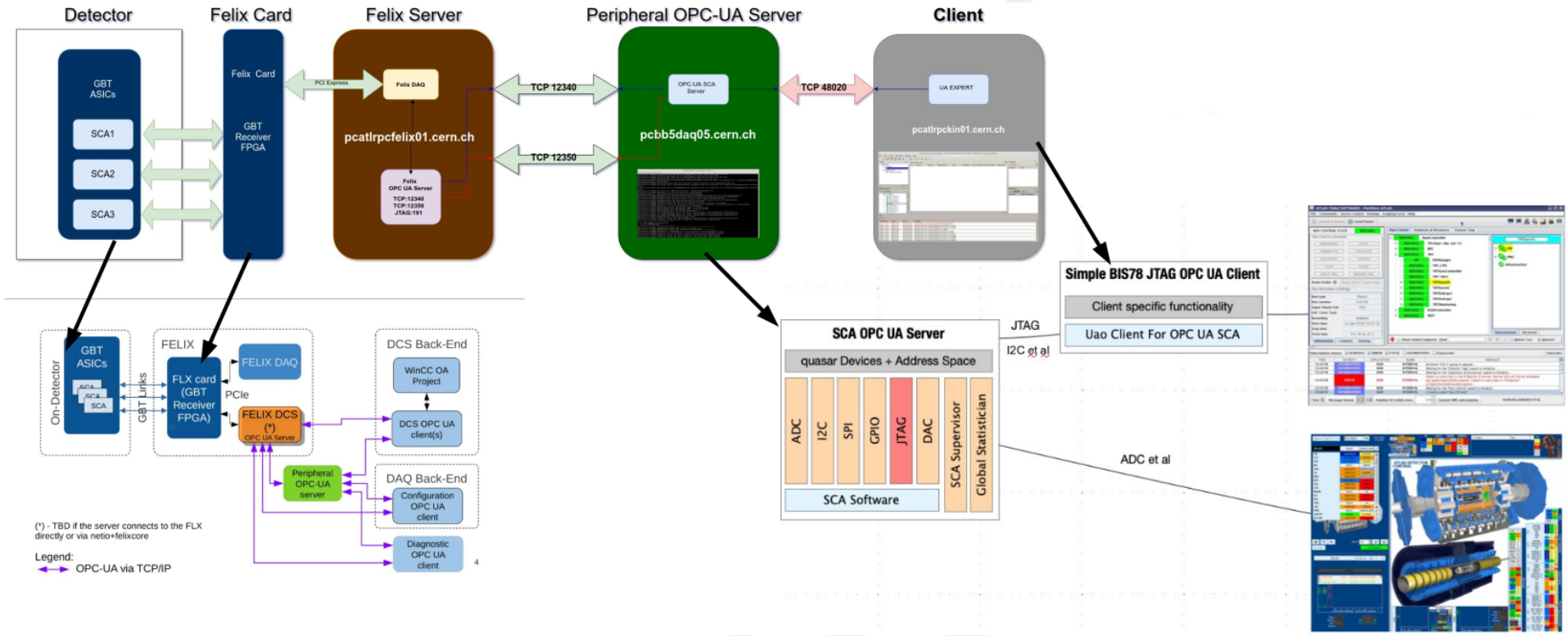

Figure I.8 OPC-UA setup in BB5.

I.4 RPC Prototype Tests in GIF++ and H8

The GIF++ facility is a gamma irradiation site located at CERN's Prevessin campus, in the Northern Region of the Super Proton Synchrotron (SPS), as shown in Figure I.9. It provides gamma irradiation and/or muon beams for testing detector prototypes and components.

The facility contains several sections: a bunker housing a Cesium-137 gamma radiation (662 KeV) source with an intensity of up to 13.9 TBq, a detector preparation area, an electronic service area, and a gas support area. The irradiation bunker is placed in the SPS North Area, and the H4 beamline runs through the center of the GIF++ bunker. The bunker's temperature and humidity are carefully controlled to replicate LHC conditions, allowing us to conduct accurate studies and measurements of the RPCs' aging characteristics. All the variables related to bunker operation (temperature,

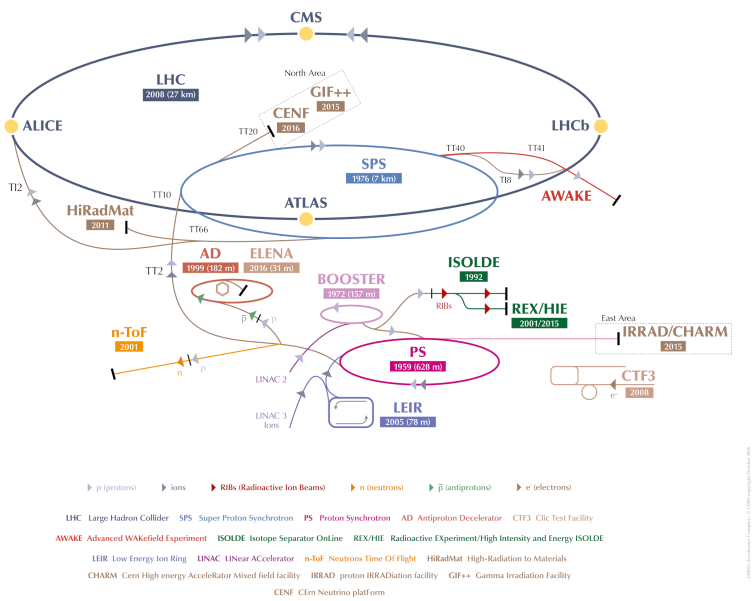

Figure I.9 Cern accelerator complex [61].

humidity, radiation, source condition, gas status, etc.) are published and stored via the DIP framework. The RPC-related variables are collected and stored via our DCS framework. The work done for the GIF++ and H8 operations are:

- Preparation of the GIF++ and H8 infrastructure for prototype testing.
- Preparation of DAQ hardware and software and its maintenance.
- Data taking shifts.

- Analysis of test data.

Figure I.10 shows the GIF++ infrastructure where we perform our tests. The collected data is used for efficiency, time and spatial resolution, photon rate, cluster size, cross-talk, and aging studies. There are two types of setups used for the tests, as shown in Figure I.12. During the testing at GIF++, both the two and three gas-gap prototypes

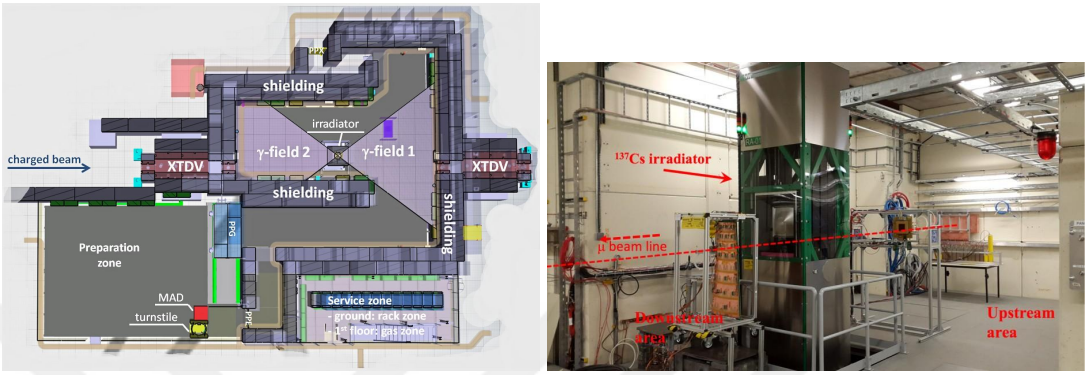

Figure I.10 GIF infrastructure.

are evaluated. Figure I.11 displays the RPC prototype with two gas gaps, where the left figure depicts the detector placement on the aluminum frame, and the right figure illustrates the setup.

The Super Proton Synchrotron (SPS) provides proton beams with energies ranging from 10 to 400 GeV to several areas, including the North Area (H2, H4 (GIF++), H6, and H8), with a maximum hadron intensity of up to 10^8 particles per spill. H2 and H4 originate from the T2 target, while H6 and H8 originate from the T4 target. The muon beams produced by the SPS are utilized in our tests. Figure I.12 shows the DAQ setup

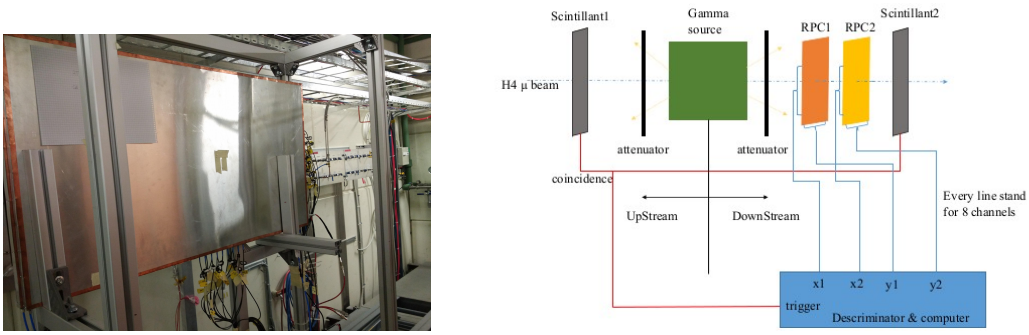

Figure I.11 GIF++ setup.

used in GIF++ and H8 test areas. Both ADC and TDC CAEN devices are used for data taking. The prototypes and detectors were also tested at H8, which provides a muon beam from the SPS. Figure I.13 shows the prototype testing at the H8 test area.

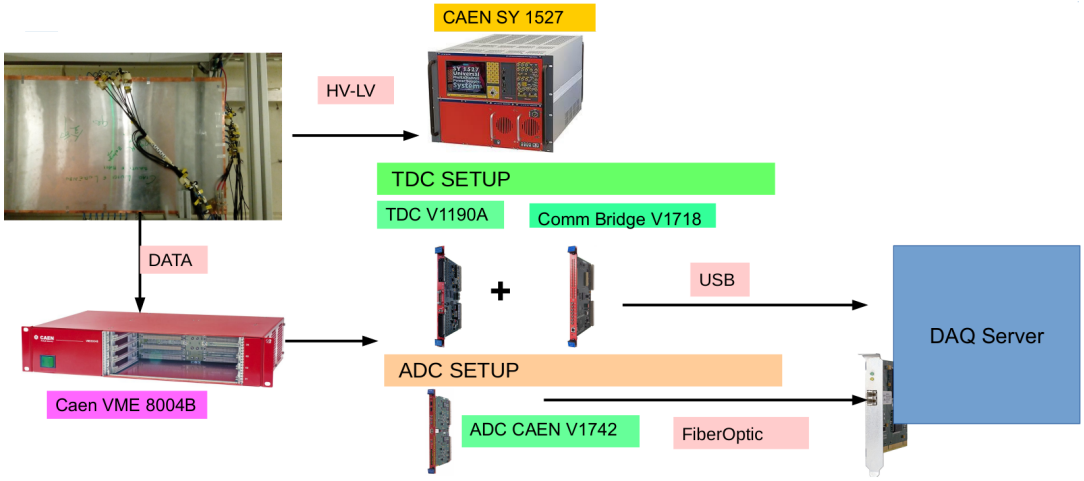

Figure I.12 TDAQ setup.

Figure I.13 H8 test setup.

I.5 Results

This section presents a collection of selected results obtained from the testing of prototypes and initial modules of BIS78 during the GIF++ and BB5 tests.

Figure I.14 illustrates the efficiency of the BIS78 prototype under varying gamma source conditions (in GIF++), where the efficiency curve remains relatively stable at around 5400 V. Lower absorption factors indicate higher source intensities (e.g., ABS 3.3), resulting in an increase in the current and voltage applied to the gas gap compared to the monitor. As a result, a correction must be made to the high voltage using Equation I.1.

$$V_{effective} = V_{applied} - I_{gap} \times R_{bakelite} \tag{I.1}$$

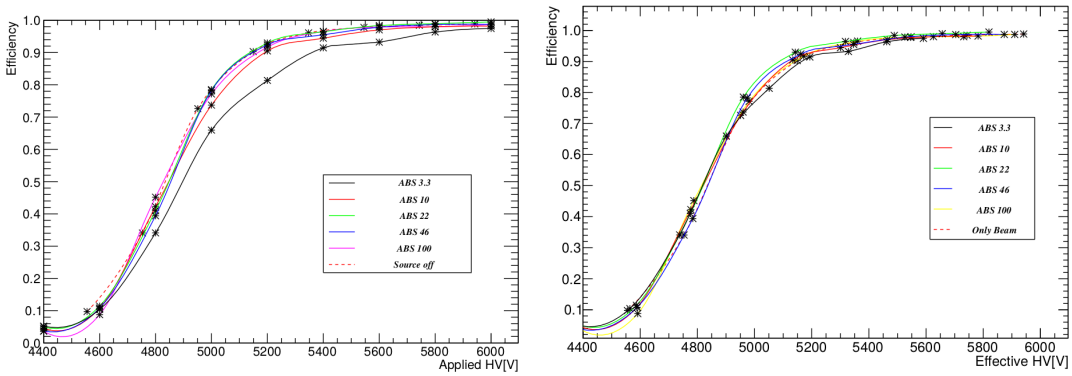

Figure I.14 (Left) Applied HV, (Right) Effective HV versus Efficiency [62].

Another property that was measured is the time resolution in relation to the effective voltage and source conditions. It is evident that the time resolution remains at around 400 ps between voltages of 5600 V and 6000 V.

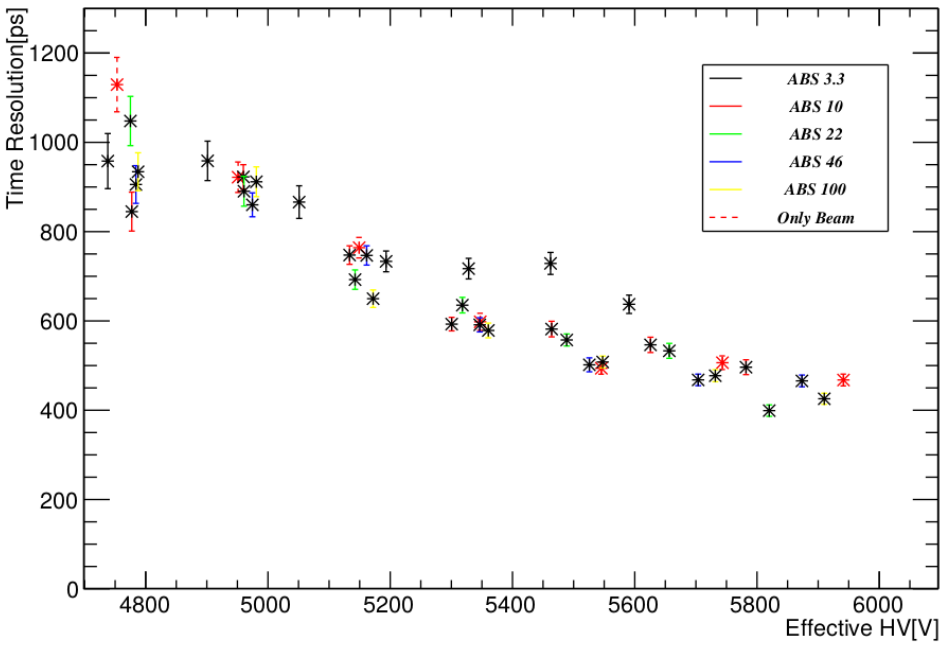

Figure I.15 Time resolution vs Effective HV [62].

Figure I.16 shows the ΔT test results of the new module of the BIS78 RPC detectors. Tests were conducted on two out of three singlets using the setup depicted in Figure I.5 at BB5. Both Figure I.15 and I.16 indicates that the first module test in BB5 agrees with the prototype result in GIF++.

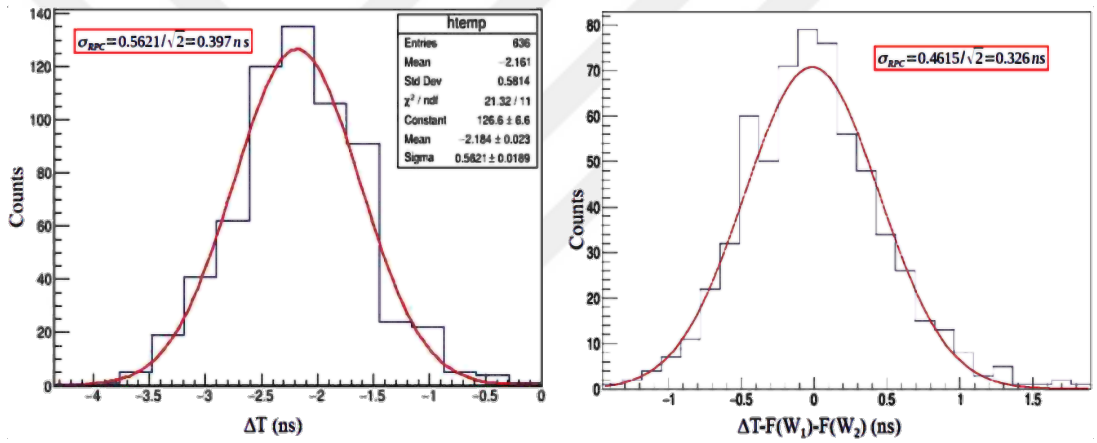

Figure I.16 Distribution of the ΔT for the 5600V. Without time walk correction(left), with time walk correction (right) [59].

PUBLICATIONS

Publications, Talks, Posters and Technical Reports

[1] Leonid Gladilin, Zekeriya Uysal, and Marina Aleksandrova. "Measurement of the B^+ production cross sections in pp collisions at $\sqrt{s}$ = 13 TeV at ATLAS:Supporting Document", Technical Report, Geneva, CERN, 2022, URL: https://cds.cern.ch/record/2804949

[2] Orhan Cakir, Emre Celebi, Hakan Cetinkaya, Hilal Kolenoglu, Gorkem Turemen, Zekeriya Uysal, Gokhan Unel, "DemirciPro's tools for completing the Linac: Ion source and LEBT line", arXiv 2103.11829, 03 2022.

[3] ATLAS Collaboration, "Performance of the ATLAS RPC detector and Level-1 muon barrel trigger at $\sqrt{s} = 13$ TeV.", CERN-EP-2020-245, arXiv 2103.01029, JINST 16 P07029. 63 p Feb 2021.

[4] O. Çakır, E. Çelebi, H. Çetinkaya, H. Kolenoglu, G. Türemen, Z. Uysal, G. Ünel, "A Graphical User Interface to Design Solenoid and Quadrupole Magnets with Demirci-Pro", Bodrum/Turkey, September 01-05 2020.

[5] H. Kolenoglu, O. Cakir, E. Celebi, H. Cetinkaya, G. Turemen, G. Unel, Z. Uysal, "Demirci-Pro: RFQ, İyon Kaynağı, LEBT ve Mıknatıs Tasarımı için Modüler Yazılım Çerçevesi", Parçacık Hızlandırıcıları ve Algıçları Yerel Altyapı ve Ar-Ge Çalıştayı(YEFAM), Istanbul/ Turkey. November 29 2020.

[6] Andrew J. Beddall, Zekeriya Uysal, "Development of Graphical User Interface for RPC Test Data", The International Aluminium-Themed Engineering and Natural Sciences Conference (IATENS'19), Seydişehir/TURKEY, October 04-06 2019.

[7] O. Cakir, E. Celebi, H. Cetinkaya, H. Kolenoglu, G. Turemen, Z. Uysal, G. Unel, DEMIRCIPRO: Ion Source Simulation Integration, Turkish Physical Society 7th Internationally Participated Congress on Particle Accelerators and Applications, September 02 2019

[8] O. Cakir, E. Celebi, H. Cetinkaya, H. Kolenoglu, G. Turemen, Z. Uysal, G. Unel, "DEMIRCI-PRO: A Single Software Interface for RFQ Ion Source and LEBT Line Design", Turkish Physical Society 35th International Physics Congress, Bodrum/-Turkey, September 04-08 2019.

[9] Sinem Simsek, Zekeriya Uysal, "BIS78 Prototiplerinin GIF++ Alanindaki Testleri", Taek Cern Workshop, Ankara/Turkey,October 04-05 2018.

CURRICULUM VITAE

After completing his undergraduate studies in physics engineering at Gaziantep University in 2001, he pursued an MSc in high energy and plasma physics. In 2009, he began his Ph.D. studies. Since 2011, he has been doing research at the European Nuclear Research Center on behalf of Gaziantep University.

During his Ph.D., he worked with the ATLAS-BJpsiX group and contributed several analyses. Additionally, he collaborates with several detector subgroups, particularly on DAQ upgrade projects.